MAY 29 1997

SANDIA REPORT

SAND97–1176 • UC–406
Unlimited Release
Printed May 1997

Advanced Tomographic Flow Diagnostics for Opaque Multiphase Fluids

J. R. Torczynski, T. J. O'Hern, D. R. Adkins, N. B. Jackson, K. A. Shollenberger

Approved for public release; distribution is unlimited.

MASTER

Sandia National Laboratories

DISTRIBUTION OF THIS DOCUMENT IS UNLIMITED

HH

DISCLAIMER

DISCLAIMER

Portions of this document may be illegible in electronic image products. Images are produced from the best available original document.

Advanced Tomographic Flow Diagnostics
for Opaque Multiphase Fluids

J. R. Torczynski[1], T. J. O'Hern[1], D. R. Adkins[1], N. B. Jackson[2], K. A. Shollenberger[1]

[1]Engineering Sciences Center

[2]Advanced Energy Technology Center

Sandia National Laboratories

P. O. Box 5800

Albuquerque, New Mexico 87185-0834

Abstract

This report documents the work performed for the "Advanced Tomographic Flow Diagnostics for Opaque Multiphase Fluids" LDRD (Laboratory-Directed Research and Development) project and is presented as the fulfillment of the LDRD reporting requirement. Dispersed multiphase flows, particularly gas-liquid flows, are industrially important to the chemical and applied-energy industries, where bubble-column reactors are employed for chemical synthesis and waste treatment. Due to the large range of length scales (10^{-6}-10^1 m) inherent in real systems, direct numerical simulation is not possible at present, so computational simulations are forced to use models of subgrid-scale processes, the accuracy of which strongly impacts simulation fidelity. The development and validation of such subgrid-scale models requires data sets at representative conditions. The ideal measurement techniques would provide spatially and temporally resolved full-field measurements of the distributions of all phases, their velocity fields, and additional associated quantities such as pressure and temperature. No technique or set of techniques is known that satisfies this requirement. In this study, efforts are focused on characterizing the spatial distribution of the phases in two-phase gas-liquid flow and in three-phase gas-liquid-solid flow. Due to its industrial importance, the bubble-column geometry is selected for diagnostics development and assessment. Two bubble-column testbeds are utilized: one at laboratory scale and one close to industrial scale. Several techniques for measuring the phase distributions at conditions of industrial interest are examined: level-rise measurements, differential-pressure measurements, bulk electrical impedance measurements, electrical bubble probes, x-ray tomography, gamma-densitometry tomography, and electrical impedance tomography. The first four techniques provide either spatially averaged or local information and are discussed in the context of validation. Although already well developed, the fifth technique is not suitable for large-scale flow experiments but is useful for validation efforts. The last two techniques are investigated and discussed in detail, and representative phase-distribution results are presented for gas-liquid and gas-liquid-solid flows in the two testbeds at conditions of interest.

Acknowledgment

Table of Contents

6

List of Figures

List of Tables

Nomenclature

$A_{\alpha\beta}$, $\tilde{A}_{\alpha\beta}$	matrices for determining c_α
B_α, $\tilde{B}_\alpha$	vectors for determining c_α
a_m, b_n	polynomial coefficients for Abel transform
B	MCA energy bin number
B_p	MCA energy bin number of peak
B_w	MCA energy bin width of peak
C_α	conductivity parameters
c_α	increments in conductivity parameters
c_{mn}, d_{nm}	reconstruction coefficient matrices for Abel transform
D	cylinder or vessel diameter
d_b	diameter of a sphere with the same volume as a prescribed bubble
$f(r, R)$	inverse Abel transform of $g(x, R)$
$g(x, R)$	Abel transform of $f(r, R)$
H_0	height of gas-liquid interface in bubble column without gas flow
H	height of gas-liquid interface in bubble column with gas flow
I	intensity (counts per second) of gamma beam
i, j	FEM nodal indices
I_e	current scale for electrodes in EIT
I_0	intensity (counts per second) of gamma beam initially
I_h	MCA intensity height of peak
J_n	normal current flux
$\mathbf{J}$	current flux vector
k, m, n, p	FEM nodal indices for nodes at electrodes
k_0, k_1, k_2	parameters for Gaussian fit to peak in MCA spectrum
L	either path length or height of measurement above vessel bottom
M_{ij}	global stiffness matrix
$M_{\alpha ij}$	derivative of the global stiffness matrix M_{ij} with respect to C_α
m_β, n_β	conductivity function internal parameters
N_e	number of electrodes in EIT system
N_n	number of nodes in FEM representation of EIT
N_σ	number of conductivity parameters in EIT
$\mathbf{n}$	outward normal unit vector
ΔP	pressure difference between two pressure transducers for DP technique
P	pressure
P_β	conductivity function internal parameters
R	cylinder or vessel radius, or domain length scale in EIT
R_β	conductivity function internal parameters
r	cylindrical coordinate
s	arc length
$s^{(k)}$	arc length location of electrode k in EIT
T	temperature

t	time
U_G	gas superficial velocity in bubble column
U_1	velocity in formula for terminal bubble velocity
U_2	velocity in formula for terminal bubble velocity
U_T	terminal velocity of an isolated gas bubble in a liquid
V	voltage
$V^{(k)}(\mathbf{x})$	voltage field for current injection and withdrawal at electrode k and node 0
$V^{(mn)}(\mathbf{x})$	voltage field for current injection and withdrawal at electrodes m and n
$V_i^{(k)}$	voltage at node i for current injection and withdrawal at electrode k and node 0
$V_i^{(mn)}$	voltage at node i for current injection and withdrawal at electrodes m and n
$V_k^{(mn)}$	voltage at electrode k for current injection and withdrawal at electrodes m and n
$V_{k,1}^{(mn)}$	voltage $V_k^{(mn)}$ when $\sigma = \sigma_1(\mathbf{x};\{C_\alpha\})/C_1$, $\alpha = 2, ..., N_\sigma$, and $C_1 = 1$
$V_0^{(mn)}$	arbitrary voltage offset, an adjustable parameter in EIT
$\partial V_i^{(k)}/\partial C_\alpha$	Jacobian
$v_k^{(mn)}$	experimental voltage at electrode k for injection, withdrawal at electrodes m, n
W	vertical separation of two pressure transducers for DP technique
$\mathbf{x}$	coordinate vector
x	Cartesian coordinate, horizontal, normal to paths
y	Cartesian coordinate, normal to x and z, parallel to paths
z	Cartesian or cylindrical coordinate, vertical, along cylinder axis
α, β	indices for conductivity parameters
δ_{ij}	Kronecker delta function
$\delta(s)$	Dirac delta function
ε	phase volume fraction or "holdup"
Γ	rms difference between computational and experimental EIT voltages
$\phi_i(\mathbf{x})$	FEM basis function
$\psi(x, R)$	$g(x, R)/[2\sqrt{R^2 - x^2}]$
η	viscosity (absolute)
μ	attenuation coefficient
ρ	density
σ	electrical conductivity
σ_0	representative value of electrical conductivity
σ_1	electrical conductivity function $\sigma = \sigma_1(\mathbf{x};\{C_\alpha\})/C_1$, $\alpha = 2, ..., N_\sigma$
τ	gamma detection time constant
ζ	surface tension
$(\ )_a$	pertaining to air
$(\ )_G$	pertaining to gas
$(\ )_L$	pertaining to liquid
$(\ )_S$	pertaining to solid
$(\ )_s$	pertaining to glass spheres
$(\ )_w$	pertaining to water

$[\ ]_{av}$	average over measurement plane
BBC	boxed bubble column
BEI	bulk electrical impedance
BEM	boundary-element method, a numerical method
CMRR	common mode rejection ratio for an amplifier
DP	differential pressure
EBP	electrical bubble probe
EIT	electrical-impedance tomography
EITA3D	FEMEIT-like code for three-dimensional voltage fields, axisymmetric conductivity
FEM	finite-element method
FEMEIT	finite-element method electrical-impedance tomography code
FIDAP	commercial finite-element method code (Fluid Dynamics International)
GDT	gamma-densitometry tomography
ICI	insulating cylindrical inclusion
LR	level rise
LSF	liquid-solid flow
MCA	multi-channel analyzer
MUX	multiplexer
PSD	phase-sensitive demodulator
RTR	real-time radiography
SBCR	slurry bubble column reactor
SCA	single-channel analyzer
TBC	transparent bubble column
XRT	x-ray tomography
VCCS	voltage-controlled current source
WCD	wax/catalyst disk
2DynaEIT	boundary-element method electrical-impedance tomography code (Dynaflow, Inc.)
2DynaEIT_fwd	code to generate validation for 2DynaEIT (Dynaflow, Inc.)
ansoln	code to generate analytical voltage fields from infinitesimal strip electrodes
fuldat	code to take adjacent-electrode EIT data and generate a full EIT data set
msheit	code to generate a triangular mesh on a circular domain for FEMEIT
postfd	code to create a FIDAP neutral file for postprocessing from FEMEIT output

1. Introduction

1.1. Overview

This report documents the work performed for the "Advanced Tomographic Flow Diagnostics for Opaque Multiphase Fluids" LDRD (Laboratory-Directed Research and Development) project and is presented as the fulfillment of the LDRD reporting requirement. Dispersed multiphase flows, particularly gas-liquid flows, are industrially important to the chemical and applied-energy industries, where bubble-column reactors are employed for chemical synthesis and waste treatment. Due to the large range of length scales (10^{-6}-10^1 m) inherent in real systems, direct numerical simulation is not possible at present, so computational simulations are forced to use models of subgrid-scale processes, the accuracy of which strongly impacts simulation fidelity. The development and validation of such subgrid-scale models requires data sets at representative conditions. The ideal measurement techniques would provide spatially and temporally resolved full-field measurements of the distributions of all phases, their velocity fields, and additional associated quantities such as pressure and temperature. No technique or set of techniques is known that satisfies this requirement. In this study, efforts are focused on characterizing the spatial distribution of the phases in two-phase gas-liquid flow and in three-phase gas-liquid-solid flow. Due to its industrial importance, the bubble-column geometry is selected for diagnostics development and assessment. Two bubble-column testbeds are utilized: one at laboratory scale and one close to industrial scale. Several techniques for measuring the phase distributions at conditions of industrial interest are examined: level-rise measurements, differential-pressure measurements, bulk electrical impedance measurements, electrical bubble probes, x-ray tomography, gamma-densitometry tomography, and electrical impedance tomography. The first four techniques provide either spatially averaged or local information and are discussed in the context of validation. Although already well developed, the fifth technique is not suitable for large-scale flow experiments but is useful for validation efforts. The last two techniques are investigated and discussed in detail, and representative phase-distribution results are presented for gas-liquid and gas-liquid-solid flows in the two testbeds at conditions of interest.

1.2. Motivation

Dispersed nondilute multiphase flow remains one of the most challenging areas in engineering mechanics despite decades of intense research and the economic importance of these flows. Direct numerical simulations of nondilute multiphase flows from first principles are not possible for conditions of industrial relevance due to the wide range of length and time scales inherent in real systems. In the simplest cases imaginable, such as zero-Reynolds-number flow of a liquid suspension of uniform solid spheres (Ingber et al., 1994) or granular flow of uniform spheres without a continuum fluid (Taylor and Preece, 1989), extremely powerful computational platforms such as massively parallel machines are required to simulate physically relevant numbers of particles (say 10^3-10^6). Complexity is escalated greatly from these cases by progressively considering the following flow classes: turbulent fluid-solid flow (direct numerical simulation of single-phase turbulent flow is now marginally possible under certain conditions for modest Reynolds numbers); nondilute turbulent gas-solid flow, where drag is the primary interphase interaction; nondilute turbulent liquid-solid flow, where the interphase momentum exchange is much more complicated due to the comparable densities of the two phases; nondilute turbulent gas-liquid flow, where the interface between the phases becomes highly distorted (see Figure 1) and experiences continual topological change; and nondilute gas-liquid-solid flow. Geometric complexity and additional physical processes such as heat and mass transfer and chemical reactions further complicate industrial systems.
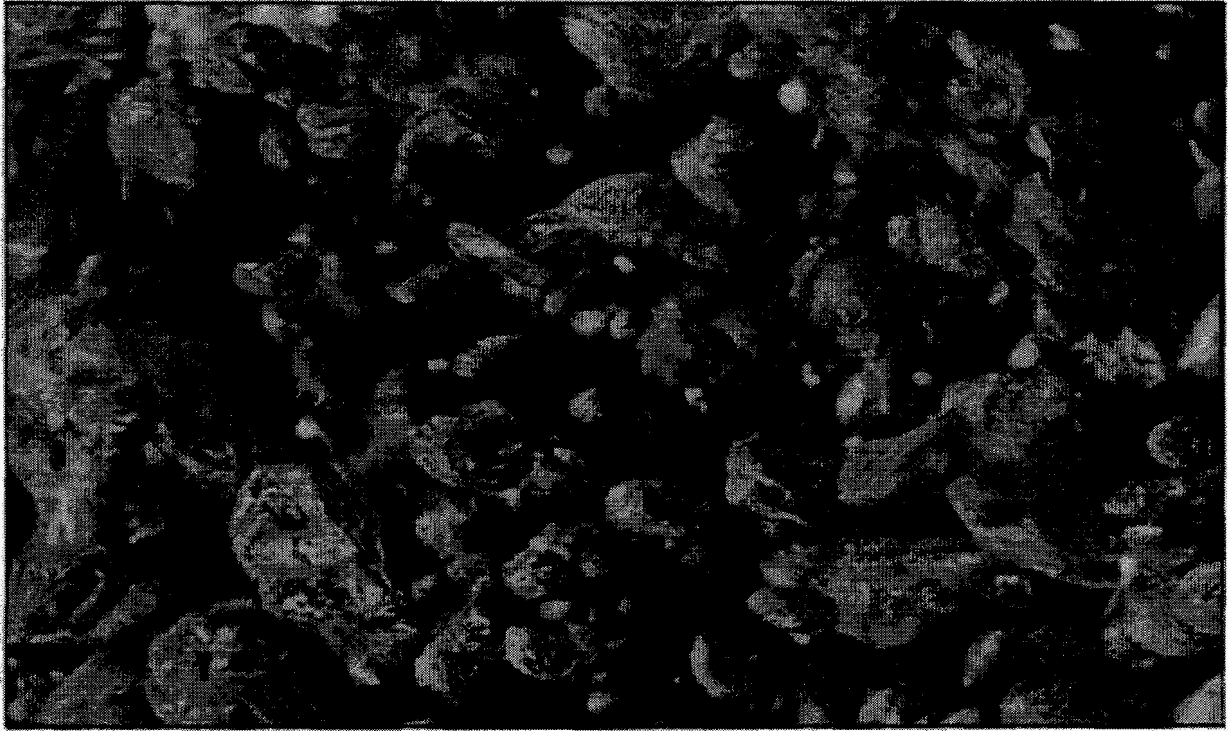
Figure 1. Nondilute turbulent gas-liquid flow.

Curiously, even the terminal velocity of an isolated gas bubble rising in a liquid continues to be a subject of research up to the present time. In a recent paper, Jamialahmadi et al. (1994) present the first properly-dimensioned relation that accurately predicts the bubble terminal velocity U_T for a wide range of parameters and flow conditions:

$$U_T = \frac{U_1 U_2}{\sqrt{U_1^2 + U_2^2}},$$
(1)

$$\text{where } U_1 = \sqrt{\frac{2\zeta}{d_b(\rho_L + \rho_G)} + \frac{g d_b}{2}} \text{ and } U_2 = \frac{(\rho_L - \rho_G)g d_b^2}{18\eta_L} \begin{cases} 1 & \text{polar liquids} \\ \left[\dfrac{3\eta_L + 3\eta_G}{2\eta_L + 3\eta_G}\right] & \text{nonpolar liquids} \end{cases}.$$
(2)

Here, ρ_G and ρ_L are the gas and liquid densities, η_G and η_L are the gas and liquid viscosities, ζ is the surface tension, d_b is the diameter of the sphere with the same volume as the bubble, and g is the gravitational acceleration. These relations were developed from heuristic arguments involving Stokes drag on a sphere and interfacial oscillations. The terminal-velocity relation is plotted in Figure 2 for an air bubble in water for various values of surface tension and is surprisingly complex. Nevertheless, Jamialahmadi et al. (1994) show this relation to be in excellent agreement with the experimental data for a wide variety of gas-liquid systems.
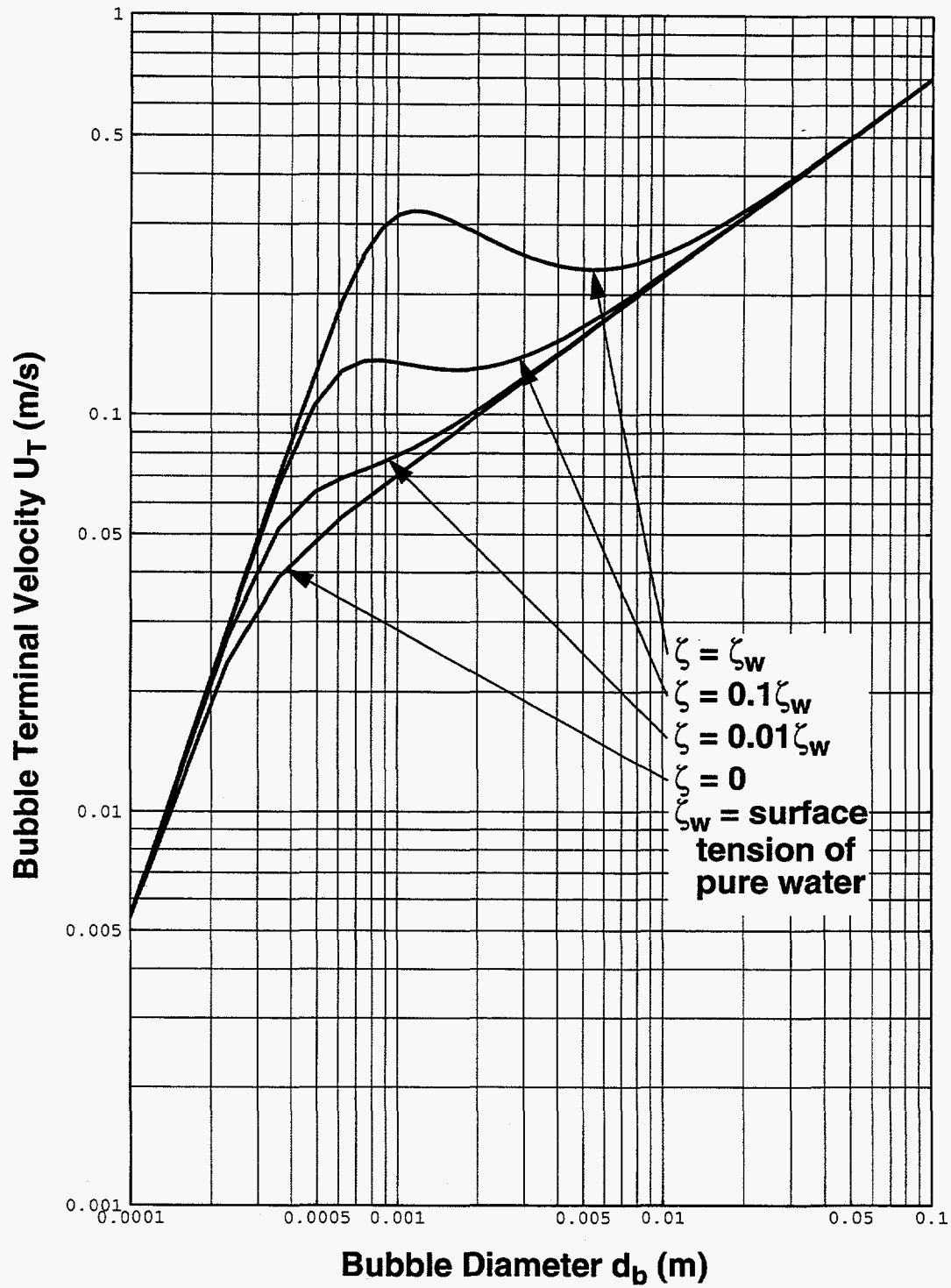
Figure 2. Terminal velocity of an isolated air bubble in water (Jamialahmadi et al., 1994).

Although direct numerical simulations of realistic multiphase flows are not possible at present (cf. Elghobashi, 1994; Crowe et al., 1996; Jaeger et al., 1996), multiphase flows can be simulated if models are introduced to describe phenomena occurring at unresolved spatial and temporal (subgrid) scales (e.g. Torvik and Svendsen, 1990; Kashiwa et al., 1993; Kashiwa et al., 1994). One such simulation of gas-liquid flow in a bubble column is shown in Figure 3 (Kumar et al., 1995b). Development of subgrid-scale models and correlations typically relies on a combination of theory (to elucidate expected scaling behavior of the modeled phenomena), numerical simulation (to examine microscale mechanisms in detail), and experiment (to search for new phenomena at extreme conditions and to quantify and validate theoretical and numerical predictions). In the continually ongoing attempt to increase the fidelity of numerical simulations employing subgrid-scale models, accuracy requirements for subgrid-scale models become increasingly stringent. As a result, experiments are called upon to deliver extremely accurate and highly detailed information to support the development of sophisticated, high-fidelity subgrid-scale models. This, in turn, necessitates the development of highly sophisticated experimental diagnostics that are capable of providing this type of information.

gas volume fraction   **liquid volume fraction**
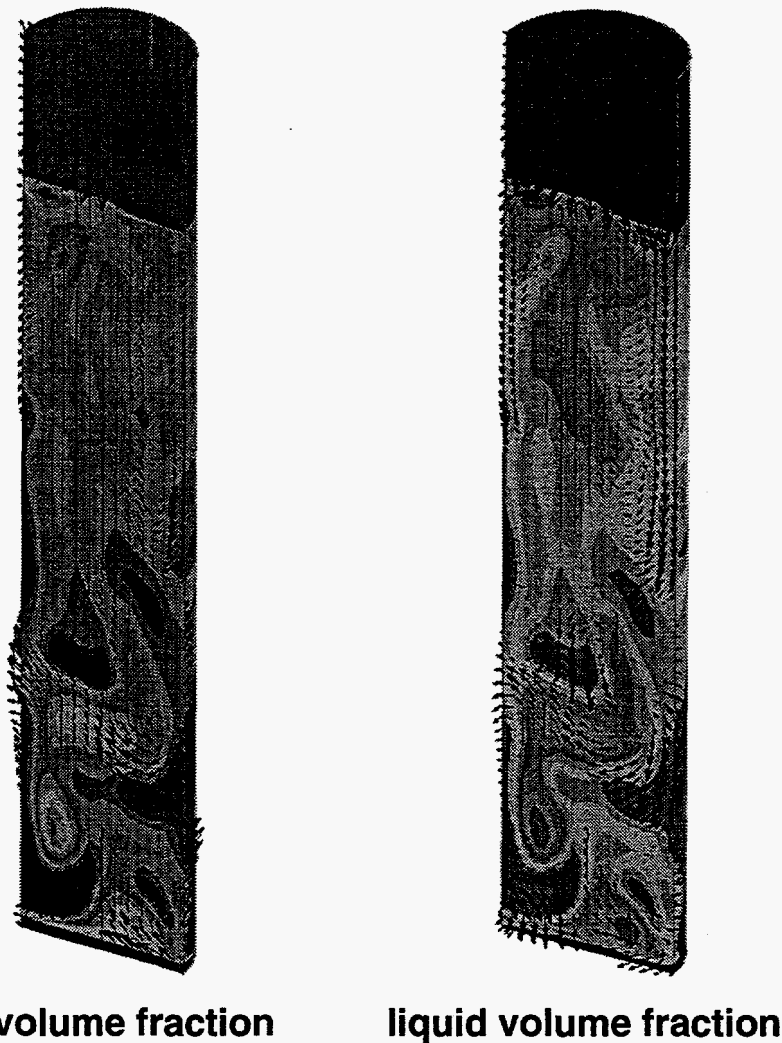
Figure 3. Los Alamos CFDLIB calculation of bubble-column flow (Kumar et al., 1995b).

Most or all of the following features characterize the type of diagnostics required for subgrid-scale model development and validation. Although volume-averaged or local measurements can be useful, particularly for diagnostics validation, full-field measurements are needed in order to develop accurate subgrid-scale models. Appreciable degrees of spatial and temporal resolution are desired since multiphase flows are rarely homogeneous in space, even at the macroscale level, and often have large fluctuations. Due to the existence of important microscale phenomena, noninvasive or minimally invasive techniques are particularly desired to avoid distorting the microscale behavior (and perhaps the macroscale behavior in the process) in the vicinity of the measurement. Techniques must be robust and capable of operating in relatively harsh mechanical, thermal, and chemical environments. Direct measurement of the desired physical quantity (e.g. phase volume fraction field) is highly desirable but rarely achievable. Instead, a different physical quantity (e.g. gamma attenuation along paths) is measured, and the quantity of primary interest is subsequently inferred via an assumed physical model (e.g. a linear relationship between phase volume fractions and gamma attenuation coefficient) and a computational algorithm (e.g. tomographic reconstruction of the field from measurements on paths). Thus, it is desirable to have a suite of rather different diagnostic techniques which rely on rather different physical assumptions and processes but which purport to measure the same physical quantity. This becomes essential when more than two phases are present.

1.3. Slurry Bubble-Column Reactors (SBCRs)

At present and in the near future, it is not possible to develop either universal numerical simulation codes or universal diagnostic techniques that cover all known regimes of multiphase flow. Rather, codes and diagnostics are typically developed within a particular context and extended to greater generality when possible. In this study, the context for diagnostics development, validation, and application is taken to be the slurry bubble-column reactor (SBCR) because of its economic and industrial importance (cf. Torczynski et al., 1994; Jackson et al., 1996ab; Dudukovic et al., 1997). Figures 4-5 show a schematic diagram of an SBCR along with a photograph of an actual SBCR (including all its ancillary plant equipment) in LaPorte, TX, operated by Air Products and Chemicals, Inc., for the U. S. Department of Energy. Briefly, an SBCR is a large-diameter, vertically oriented, cylindrical pressure vessel partially filled with a catalyst-laden liquid through which a reactive gas is bubbled (sparged). As the bubbles rise, gas dissolves into the liquid, encounters the catalyst, reacts to form the desired chemical substance, and releases heat to the surrounding liquid if the reaction is exothermic. Important industrial examples include the production of methanol or slurry Fischer-Tropsch wax (a mixture of long-chain hydrocarbons) from syngas derived from coal (principally a mixture of hydrogen and carbon monoxide). To render such processes economically viable, such reactors must be scaled to large sizes (e.g. several meters in diameter and tens of meters in height). Due to the expense of constructing a plant, accurate predictions of hydrodynamic behavior is essential when scaling to large sizes. More specifically, overly conservative scaling can lead to costly overdesign (i.e. an SBCR of far greater volume than required to convert all of its feedstock into product), and overly optimistic scaling can lead to costly, inefficient operation (i.e. an SBCR that is too small to convert all of its feedstock into product) or possibly to catastrophic failure (e.g. from excessive gas channeling through the liquid due to unexpected hydrodynamic effects). The design and scale-up process currently relies on extrapolation from small-scale experiments, where the extrapolation is conservative to minimize the possible impact of encountering a different hydrodynamic regime at larger scale. This process would be greatly facilitated by the availability of validated numerical models of multiphase flow in the parameter ranges of interest, which, as indicated above, requires the capability of acquiring the type of experimental data needed to develop and validate these models at conditions of interest.
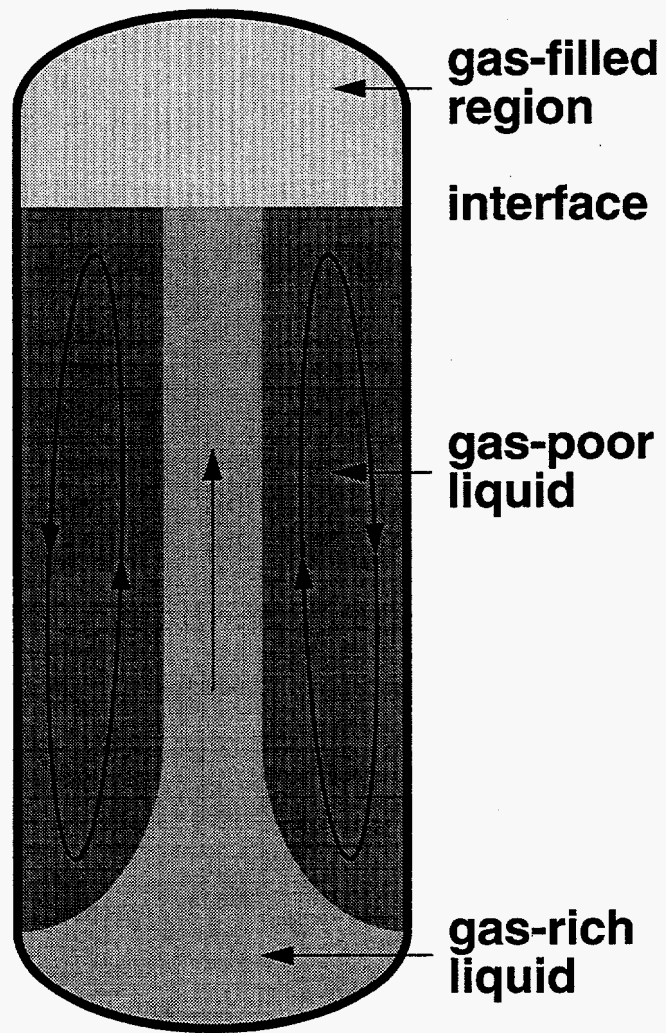
Figure 4. Slurry bubble-column reactor (SBCR) schematic diagram.

LaPorte Alternative Fuel Development Unit (AFDU), LaPorte, TX
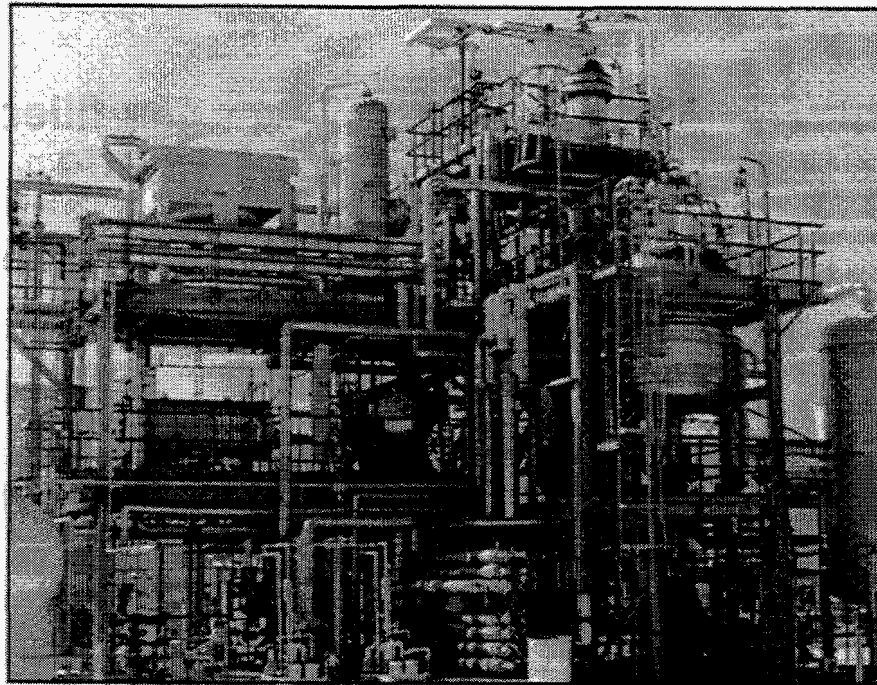
SIMPLIFIED PROCESS FLOWSHEET FOR LAPORTE PDU
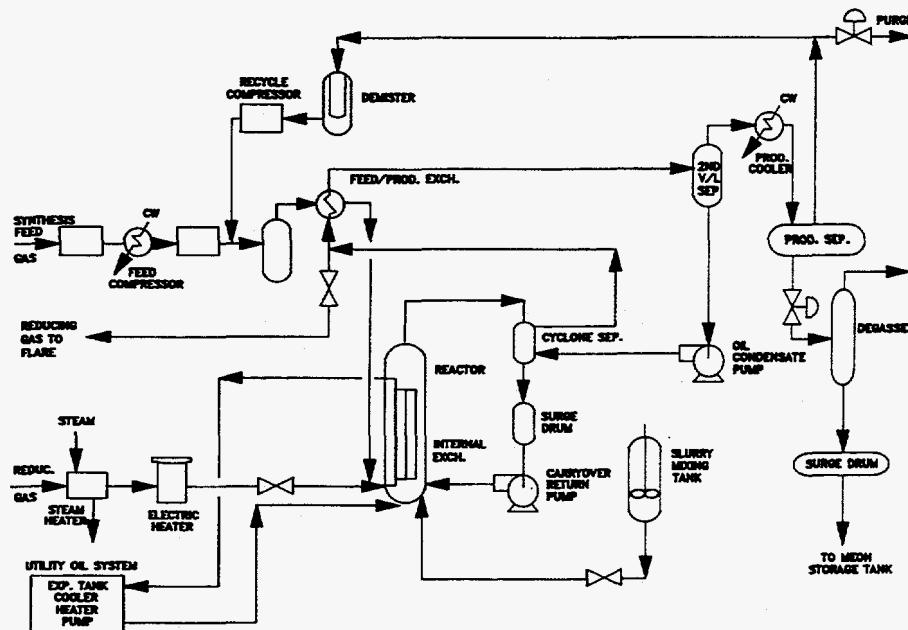
Figure 5. SBCR photograph and process diagram, courtesy of Air Products and Chemicals.

An SBCR is essentially a three-phase bubble column, with gas bubbles and solid particles contained in liquid at nondilute concentrations. Several comprehensive reviews exist in which bubble-column hydrodynamics is discussed in great detail (Shah and Deckwer, 1983; Joshi et al., 1990; Deckwer and Schumpe, 1993; Fan and Tsuchiya, 1993), and many studies exist in which particular features of bubble-column hydrodynamics are examined (e.g. Zuber and Findlay, 1965; Devanathan et al, 1990; Dudukovic et al., 1991; Wilkinson et al., 1992; Kumar et al., 1994; Krishna and Ellenberger, 1996; Dudukovic et al., 1997). The most important phenomenon governing the hydrodynamic behavior of a two-phase gas-liquid bubble column (and of a three-phase gas-liquid-solid bubble column) is buoyancy. A gas distribution that is maximum at the vessel axis and minimum at the vessel side walls is often observed and establishes a liquid circulation as indicated in the SBCR schematic diagram in the absence of forced liquid flow. The strength of this liquid circulation is determined by balancing the rate of momentum production by buoyancy against the rate of momentum transport to the side walls by viscous effects or turbulent mixing. Bubble-column hydrodynamic behavior is often correlated in terms of the gas superficial velocity U_G, which is the total gas mass flow divided by the gas density ρ_G at column conditions (i.e. not at standard conditions) and by the total cross-sectional area of the column, $\pi D^2/4$ for a cylinder of diameter D. Of particular interest is the dependence of the gas volume fraction or "holdup" ε_G on the gas superficial velocity U_G. At low gas flow rates, the homogeneous bubbly flow regime is typically encountered, in which the volume-averaged gas volume fraction increases linearly with gas superficial velocity. At higher gas flow rates, the churn-turbulent flow regime is typically encountered, in which the volume-averaged gas volume fraction increases sublinearly with gas superficial velocity. Unlike the homogeneous bubbly flow regime, the churn-turbulent flow regime is characterized by extreme flow unsteadiness, with velocity fluctuations comparable to average velocity values. The transition between homogeneous bubbly flow and churn-turbulent flow is sometimes explained in terms of the appearance of small numbers of extremely large bubbles in the latter, but this interpretation is not universally accepted. Different types of flow regimes and transitions are possible for different vessel diameters. For example, "slugging" (vertically adjacent regions alternately filled with gas and liquid) can occur for small-diameter vessels. Relatively little information is available for vessels with diameters much in excess of 1 m. The picture is further clouded by the fact that pressure, temperature, viscous effects, surface tension, sparger (gas injector) configuration, and the presence of solid particles all exert significant, and often nonintuitive, influences on bubble-column hydrodynamic behavior.

1.4. Scope of Existing and Proposed Diagnostics

The state of a two-phase gas-liquid bubble column is completely determined by specifying the pressure, the temperature, the velocity vector, and the material (gas or liquid) at all points within the vessel for all times, or at least with spatial and temporal resolution sufficient to represent all microscale processes with reasonable accuracy (Dudukovic et al., 1997). Clearly, no diagnostic or set of diagnostics is capable of measuring all of these fields with the required resolution. At present, very few diagnostics exist or have been proposed that make either in situ microscale measurements (e.g. the diameter or velocity of individual bubbles or solid particles) or average measurements of microscale statistical properties (e.g. bubble size and velocity distributions). Some exceptions include electrical and optical probes to measure diameters of individual bubbles and acoustic scattering techniques to measure bubble size distributions (e.g. Duraiswami, 1993). However, significant technical challenges must be overcome to reduce these techniques to routine practice, particularly for nondilute turbulent flow.

Most diagnostics that are currently available or under development focus on making spatially and/or temporally resolved measurements of macroscale properties. For example, pressure and temperature can be measured using various types of transducers having adequate temporal resolution on the

macroscale. Adequate macroscale spatial resolution can be achieved by mounting the transducers on supports that can be traversed throughout the region of interest although this is rather invasive. Velocity measurements for nondilute turbulent multiphase flow are much rarer, even at the macroscale. The best example is presented by Dudukovic and coworkers, who have developed computer automated radioactive particle tracking (CARPT) to measure the liquid velocity field (Moslemian et al., 1992; Yang et al., 1994; Dudukovic et al., 1997). In this technique, a small, neutrally-buoyant, radioactive particle is placed within the liquid, and its position is triangulated in real time using multiple radiation detectors. The particle is presumed to move with the liquid, so its trajectory yields both the time-averaged liquid velocity field and liquid-velocity-fluctuation statistics at all locations sampled by the particle, generally the entire liquid-filled region.

Characterization of macroscale material distribution is the target of several existing and proposed diagnostic techniques, which is reasonable considering the importance of material distribution in determining the hydrodynamic behavior of bubble-column and other multiphase flows. Techniques can be divided into two broad classes: (1) diagnostics that provide only spatially-averaged or local information about material distribution; and (2) diagnostics that provide measurements of the macroscale material distribution field throughout a significant portion of the flow. While the first class of techniques provides only limited information, the second class provides the type of information needed for model validation and thus are the focus of this effort. In this second class, spatial resolution is obtained either directly, by measurements at an array of locations covering the region to be examined, or indirectly, by using mathematical techniques such as tomographic reconstruction to infer spatially resolved information from quantities measured on boundaries. Two particular techniques belonging to the second class that obtain spatial resolution indirectly are examined herein: gamma-densitometry tomography and electrical-impedance tomography.

In the remainder of this report, the following subjects are addressed. First, the physical bases and implementations of various diagnostic techniques are discussed, starting with techniques that yield only volume-averaged or local information and concluding with techniques that yield spatially and/or temporally resolved information. The former group includes level-rise measurements, differential-pressure measurements, bulk electrical impedance measurements, and electrical bubble probes, and the latter group includes x-ray tomography, gamma-densitometry tomography, and electrical-impedance tomography. Preliminary validation efforts using these techniques are discussed. Subsequently, advanced testbeds are described, and the results of extensive application of gamma-densitometry tomography and electrical-impedance tomography to these testbeds are presented.

2.   Diagnostic Techniques

Several diagnostic techniques have been examined that can provide information about material distribution in multiphase flows. These diagnostic techniques differ both in the physical effect employed to infer material distribution and in the degree of spatial and temporal resolution that can be achieved. Two broad classes of diagnostics can be defined depending on the degree of spatial resolution that is achieved: (1) those diagnostics yielding only spatially-averaged or local information; and (2) those diagnostics yielding spatially resolved information. The first class of diagnostics includes level-rise (LR) measurements, differential-pressure (DP) measurements, bulk electrical impedance (BEI) measurements, electrical bubble probes (EBPs), optical bubble probes, heat-injection probes, and acoustical bubble probes. Of these seven techniques, the first four are examined herein. The second class of diagnostics includes x-ray tomography (XRT), gamma-densitometry tomography (GDT), electrical-impedance tomography (EIT), and acoustical tomography. Of these four diagnostics, the first is used for validation purposes, the second and third are examined extensively, and the fourth has not been investigated.

2.1.   Techniques Yielding Spatially-Averaged or Local Information

Diagnostic techniques yielding spatially-averaged or local material-distribution information for multiphase flows are useful while attempting to develop and validate more advanced noninvasive diagnostics capable of providing spatially resolved material distribution. Four such techniques have been employed in this capacity: level-rise (LR) measurements, differential-pressure (DP) measurements, bulk electrical impedance (BEI) measurements, and electrical bubble probes (EBPs). The first three provide volume-averaged values of material volume fractions over a significant region of the flow, whereas the last technique provides a local measurement of material volume fractions.

2.1.1.   Level-Rise (LR) Technique

The level-rise (LR) technique is discussed here in the context of a gas-liquid bubble-column flow, as shown in Figure 6. It is a conceptually simple technique that relies on the incompressibility of the liquid portion of the multiphase flow and provides a value for the gas and liquid volume fractions averaged over the entire volume of the bubble column. The height H_0 of the gas-liquid interface above the bottom of the column is measured in the absence of gas flow, and the expanded height H is measured in the presence of gas flow. When the bubble column has a constant cross-sectional area, the volume-averaged values of the gas and liquid volume fractions are given by the relations

$$\varepsilon_G = 1 - \frac{H_0}{H} \text{ and } \varepsilon_L = \frac{H_0}{H}. \tag{3}$$

The expanded height can be measured either visually or by using a video camera and image-processing software. The principal source of uncertainty for this technique is that the gas-liquid interface during gas flow is neither flat nor stationary in time. The combination of these two features precludes the use of common image-processing techniques to reduce this uncertainty. Thus, in this study, visual observation is used to estimate the expanded height during gas flow. Extension of this technique to more than two phases is straightforward, but additional information is then required to determine the volume fractions of all phases unambiguously.

23
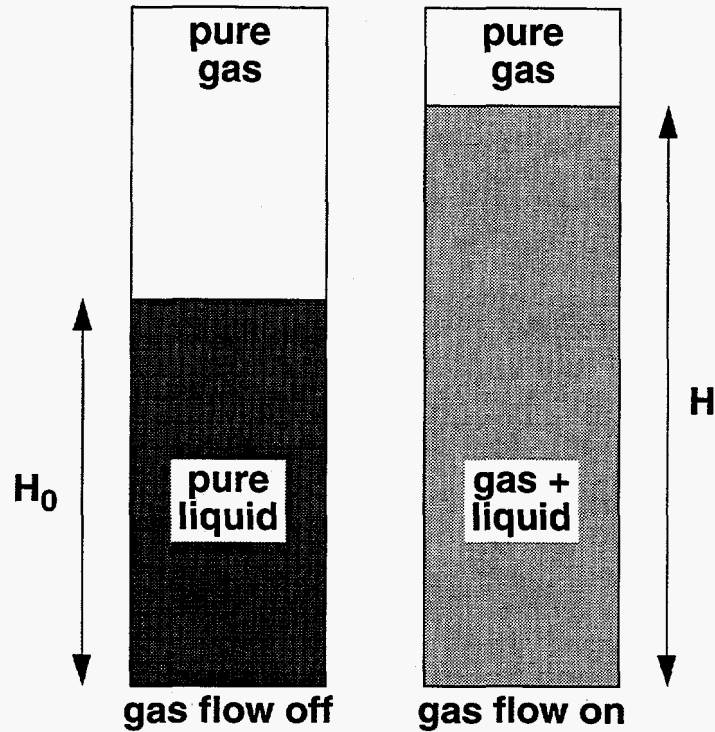
Figure 6. Schematic diagram of level-rise (LR) technique.

2.1.2. Differential-Pressure (DP) Technique

The differential-pressure (DP) technique is discussed here in the context of a gas-liquid bubble-column flow, as shown in Figure 7. This technique requires a gravitational field (as does the bubble-column flow itself) and yields a value for the gas and liquid volume fractions averaged over the region of the bubble column between two vertically offset pressure transducers. The pressure difference ΔP is measured between two pressure transducers separated by a distance W, and the measured pressure gradient is assumed to be purely hydrostatic at the average density of the gas-liquid mixture:

$$\Delta P = (\varepsilon_G \rho_G + \varepsilon_L \rho_L) g W \text{ and } \varepsilon_G + \varepsilon_L = 1, \tag{4}$$

where ρ_G and ρ_L are the gas and liquid densities and g is the gravitational acceleration. These relations allow determination of the gas and liquid volume fractions:

$$\varepsilon_G = \frac{\rho_L g W - \Delta P}{(\rho_L - \rho_G) g W} \text{ and } \varepsilon_L = \frac{\Delta P - \rho_G g W}{(\rho_L - \rho_G) g W}. \tag{5}$$

Due to the presence of pressure fluctuations due to flow unsteadiness, these relations are applied only in the time-averaged sense. Also, the gas density is often neglected since it is typically 2-3 orders of magnitude smaller than the liquid density. The principal source of uncertainty for this technique lies in the basic assumption that the time-averaged pressure gradient is hydrostatic. This assumption constrains the time-averaged liquid-acceleration and wall-shear contributions to the pressure

gradient to be small compared to the hydrostatic contribution. The former constraint requires that the time-averaged velocity and volume-fraction fields vary slowly in the vertical direction. This requirement would be satisfied if these fields approached their "fully developed" distributions, which is believed to occur within a few vessel diameters above the point of gas injection. However, this requirement may not be true near the bottom of the bubble column or near the gas-liquid interface, where the liquid is strongly accelerated and actually reverses its direction of flow. While difficult to quantify, the latter constraint suggests operation at high Reynolds numbers (small viscosity). However, it should be emphasized that wall shear does not vanish for turbulent flow in the limit of zero viscosity. Since the Reynolds numbers under consideration are on the order of 10^3-10^6, viscous wall shear appears acceptably small, but multiphase turbulent wall shear is difficult to assess. Extension of this technique to more than two phases is straightforward, but additional information is then required to determine the volume fractions of all phases unambiguously.
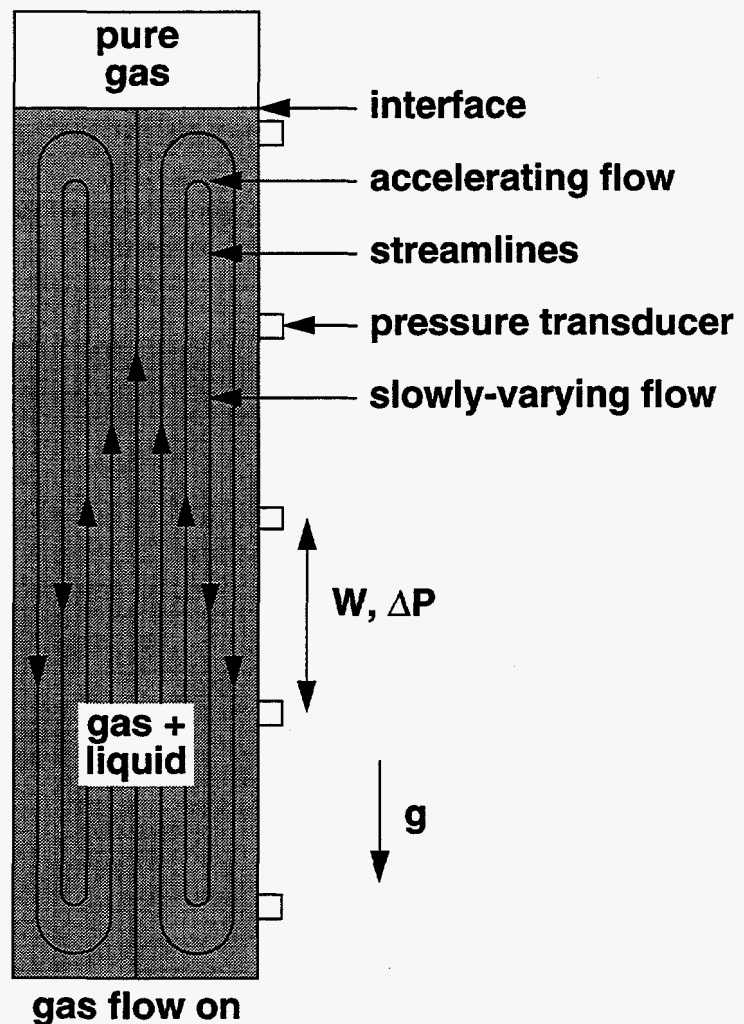
Figure 7. Schematic diagram of differential-pressure (DP) technique.

2.1.3. Bulk Electrical Impedance (BEI) Technique

The bulk electrical-impedance (BEI) technique is discussed here in the context of a gas-liquid bubble-column flow. This technique depends on the liquid having a much greater electrical conductivity than the gas and yields a value for the gas and liquid volume fractions averaged over an ill-defined region of the bubble column between two oppositely-positioned large-area electrodes. The gas-liquid mixture is assumed to be a resistive medium with a mixture conductivity σ_m given by the Maxwell-Hewitt relation for a random dispersion of small insulating spheres (gas bubbles) within a continuum (the liquid) of conductivity σ_L (cf. Hewitt, 1978; Ceccio and George, 1996):

$$\frac{\sigma_m}{\sigma_L} = \frac{1 - \varepsilon_G}{1 + (\varepsilon_G/2)}. \tag{6}$$

This relation can be inverted to determine the gas and liquid volume fractions:

$$\varepsilon_G = \frac{1 - (\sigma_m/\sigma_L)}{1 + (1/2)(\sigma_m/\sigma_L)} \text{ with } \varepsilon_G + \varepsilon_L = 1. \tag{7}$$

These relations should be applied to instantaneous quantities but are typically applied using time-averaged quantities.

Figure 8 shows a typical BEI probe ring, which has two rectangular electrodes (3.8 cm tall, 120° in angular extent) positioned at opposite sides of the ring.
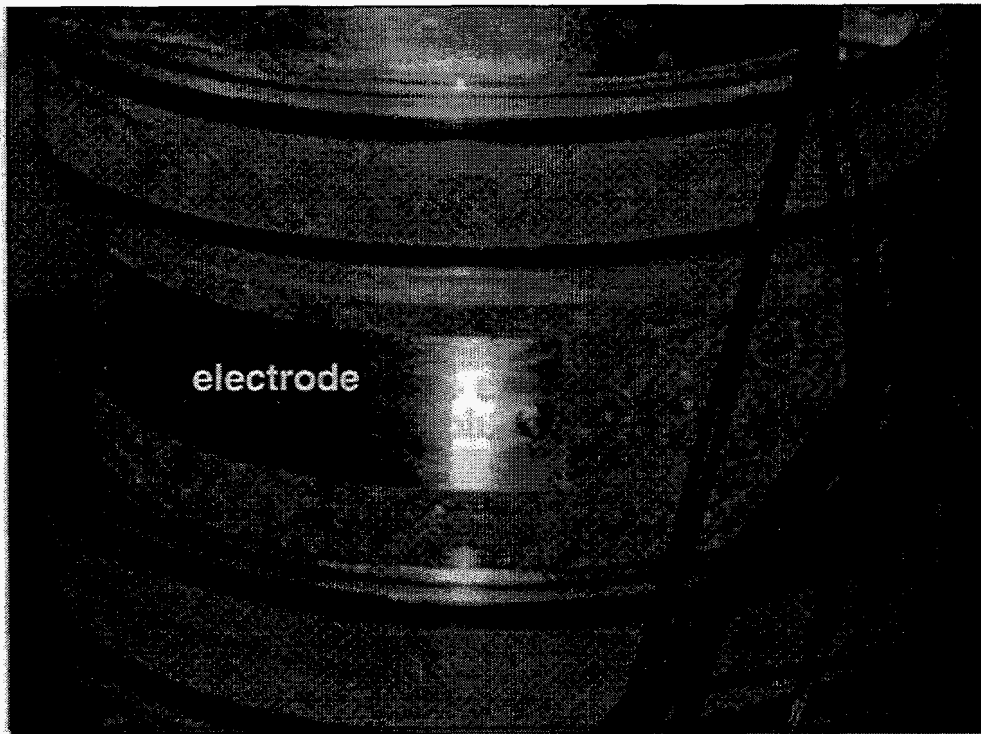
Figure 8. Bulk electrical impedance (BEI) probe ring with two rectangular electrodes.

In typical operation, neither the mixture conductivity nor the liquid conductivity is measured directly since this would require detailed knowledge of the voltage distribution within the mixture, which is particularly sensitive to various aspects of the electrode geometry such as corners and edges. Instead, a known alternating current (typically at frequencies around 50 kHz) is passed from one electrode to the other in the absence of gas flow and in the presence of gas flow, and the resulting voltage differences are measured for both cases. By virtue of Ohm's Law, the ratio of the mixture conductivity to the liquid conductivity is equal to the ratio of the voltage without gas flow to the voltage with gas flow. The principal sources of uncertainty for this technique lie in three areas: (1) the assumption of a spatially uniform distribution of gas volume fraction in measurement region; (2) the assumption of the Maxwell-Hewitt relation, which relies on spherical bubbles; and (3) the use of time-averaged quantities rather than instantaneous quantities. As will be shown in subsequent sections, a strong radial variation of gas volume fraction generally exists in bubble-column flows. It appears possible to "calibrate" the BEI technique by comparison with another technique for measuring gas volume fraction, but this calibration is not generic because it depends on the radial variation of the gas volume fraction present in the flow used for calibration. Moreover, for large gas volume fractions, bubble shapes may depart significantly from sphericity, so the Maxwell-Hewitt relation, which assumes spherical bubbles, becomes of questionable validity. Assessing the impact of time-averaging requires knowledge of the size of gas-volume-fraction fluctuations relative to the average gas volume fraction. This quantity is not believed to be large but cannot be measured at present. Because of the above considerations, it is best to use BEI with systems for which calibration is possible and for which conditions do not depart significantly from the conditions used for calibration. Extension of this technique to more than two phases is straightforward if all but one of the phases are both dispersed and insulating, but additional information is then required to determine the volume fractions of the dispersed insulating phases unambiguously.

2.1.4. Electrical Bubble Probe (EBP)

An electrical bubble probe (EBP) has been developed to make local measurements of gas volume fraction in gas-liquid bubble-column flow. A schematic diagram of an EBP is shown in Figure 9. This probe consists of two coaxial electrodes separated by insulating material mounted on a support. Since the bubbles travel predominately upward, the probe is oriented pointing downward. The voltage required to maintain a prescribed current between the electrodes is greatly increased when the probe intercepts a bubble, so the voltage history reveals the amounts of time the probe spends immersed in gas and in liquid. These times are interpreted as proportional to the gas and liquid volume fractions at the location of measurement. If the voltage observed with liquid immersion is much smaller than the voltage observed with gas immersion, then the rms of the voltage history is proportional to the gas volume fraction.

An EBP has been fabricated for which the outer electrode has a diameter of 1.27 mm (0.050 inch) and the distance from the inner electrode tip to the outer electrode edge is 0.635 mm (0.025 inch). This probe was inserted into the transparent bubble column (discussed later in this report), and voltage histories were recorded for several air flow rates. One voltage history is shown in Figure 9, and bubble interceptions are readily apparent. A comparison of the rms EBP voltage to the DP signal (where a value of 0 indicates a gas volume fraction of 0) is also shown in Figure 9. The good correlation indicates that EBPs can provide accurate gas-volume-fraction measurements. Radial gas volume fraction profiles, acquired by traversing the probe and assuming that the rms of the voltage history is proportional to the gas volume fraction, are shown in Figure 10. Cross sectional averages of these profiles are in good agreement with DP results (not shown). Although these results are encouraging, more effort is required to determine whether an EBP can be successfully applied to highly nondilute flow, to flows with wide ranges of bubble sizes, or to flows with more than two phases.

electrodes

1.6

bubble probe signal (V)

←—— bubble ——→
interceptions

0

0   1   2

time (s)

air-water, 19 cm ID vessel
0-400 liters/minute air

0.7

rms bubble-probe signal (V)

0

0   1

differential pressure signal (V)
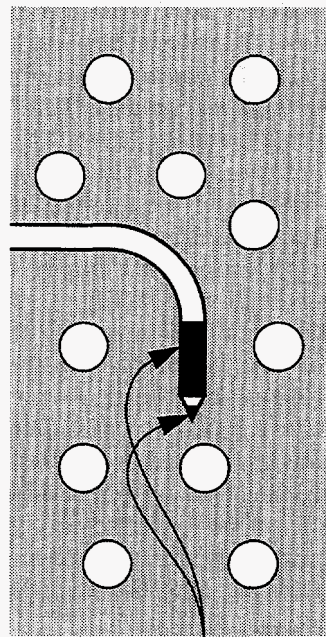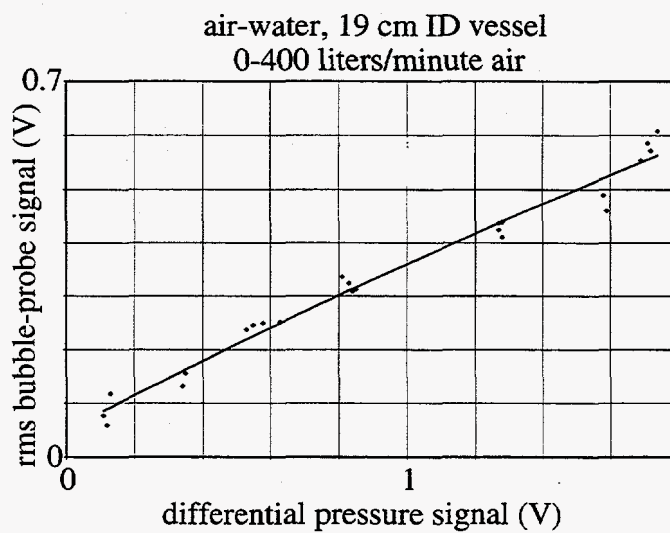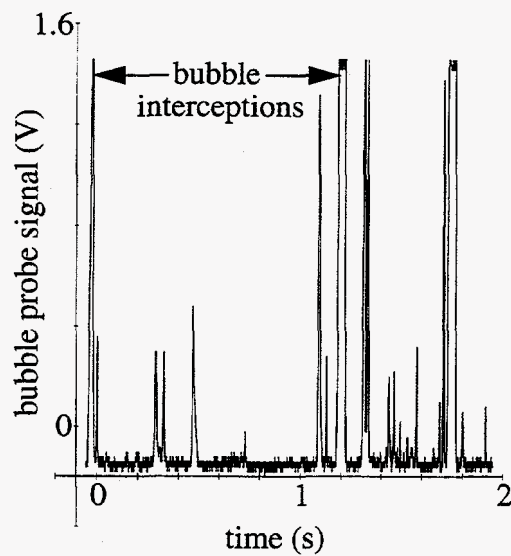
Figure 9. Electrical bubble probe (EBP) schematic, bubble interceptions, and rms correlation.
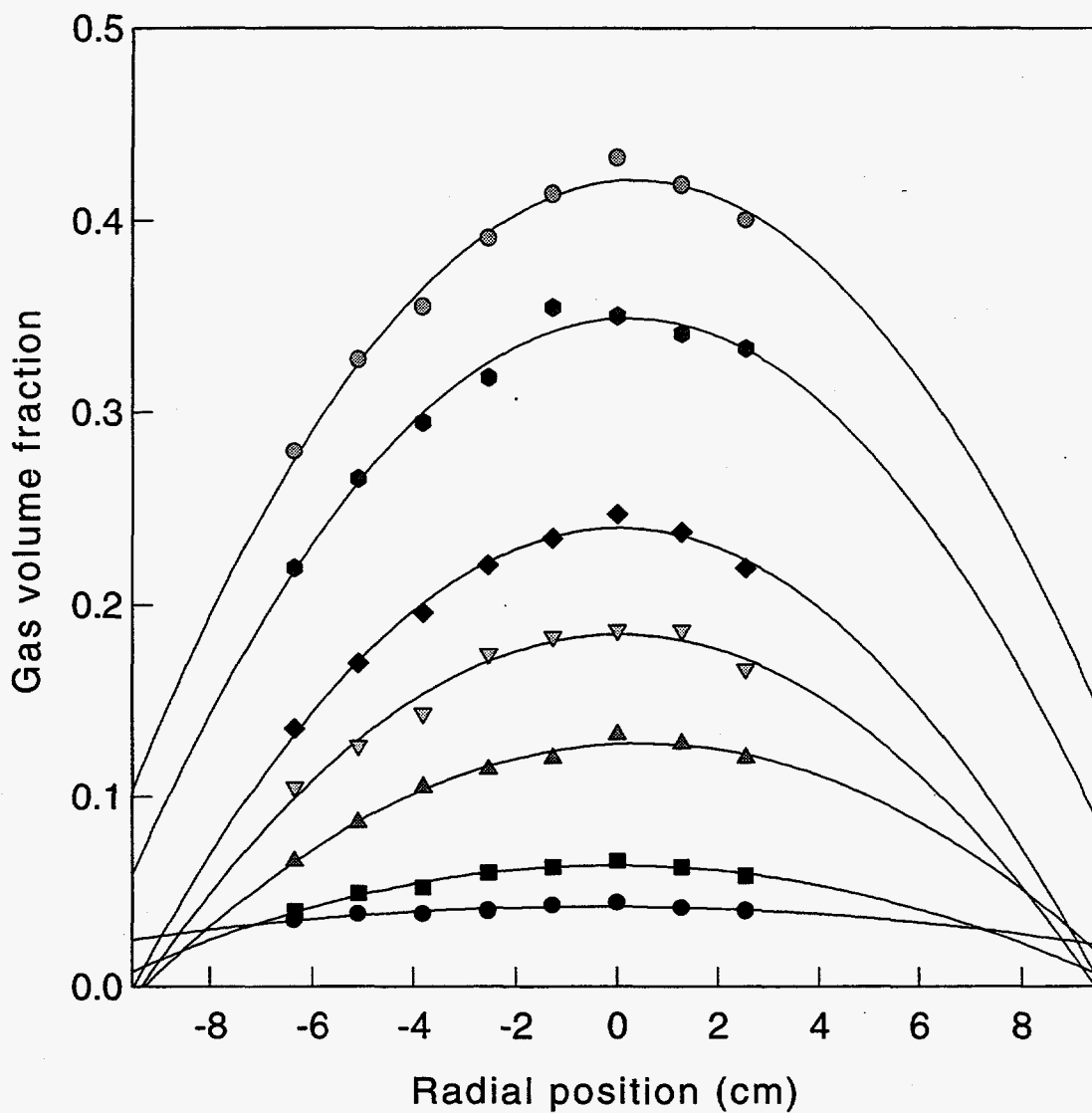
Figure 10. Gas volume fraction radial distributions from EBP.

2.2. X-Ray Tomography (XRT) and Real-Time Radiography (RTR) Techniques

Sandia has very extensive radiographic facilities for determining material distribution. These facilities have generally been applied to solid objects in the past, but application to flowing systems is possible as well under certain circumstances. Two different systems were used to perform validation experiments (Thompson and Stoker, 1997). One was an x-ray tomography (XRT) system for performing tomographic reconstructions of static material distributions, and the other was a real-time radiography (RTR) system capable of providing a temporally resolved x-ray "shadow" of a flow.

2.2.1. XRT System
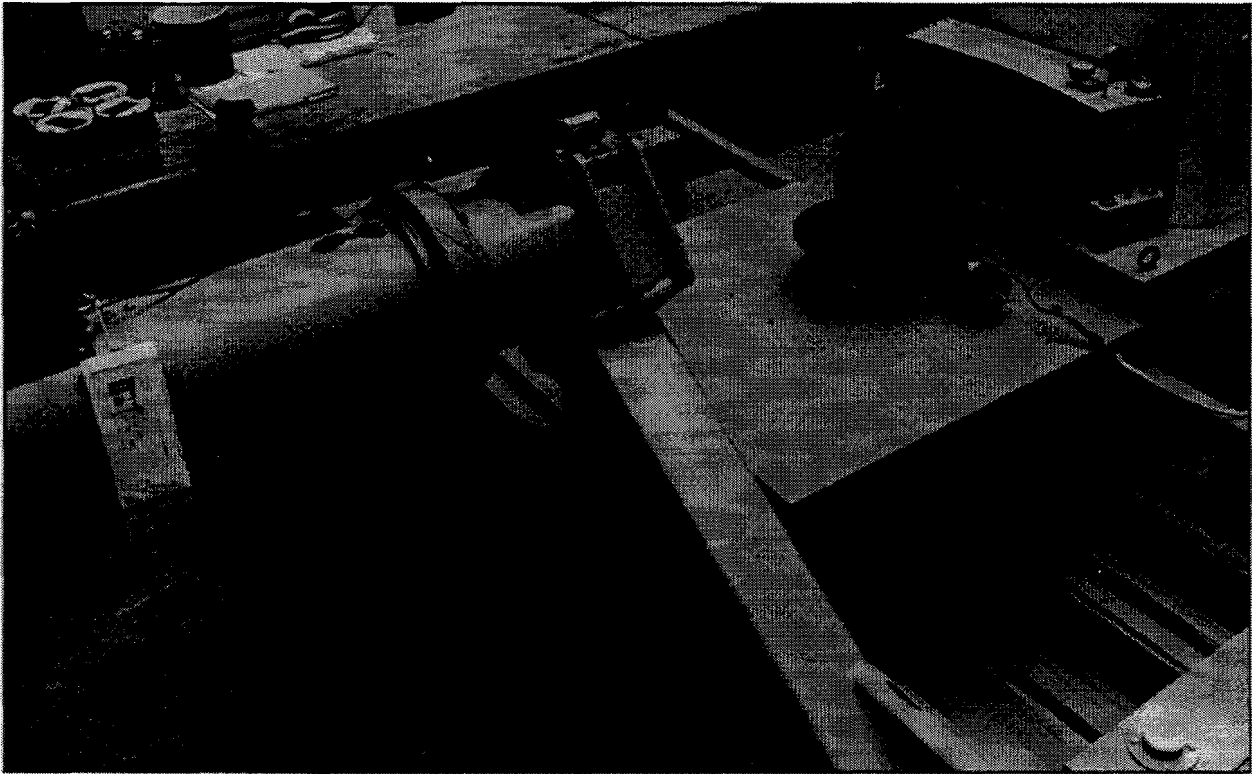
Figure 11. X-ray tomography (XRT) experimental setup.

The XRT system, shown in Figure 11, employs a Van de Graaff accelerator (at left of Figure 11) weighing approximately 2000 kg to produce a beam of x-ray photons with energies up to 2 MeV. A 31-channel Scientific Measurement Systems coplanar detector array (at right of Figure 11) of NE102 plastic scintillators bonded to photomultiplier tubes (PMTs) is used to detect the x-ray photons transmitted through the object to be imaged. This detector array is capable of being laterally repositioned (dithered) to 20 stations to create a much larger virtual array with $31 \times 20 = 620$ detectors. A thresholded pulse-counting approach is used to record the x-ray photons for each detector.

Objects with diameters up to 1 m and weights up to 200 kg can be placed on the translational-rotational stage between the x-ray source and the detector array (at center of Figure 11). Each combination of a translational position and a rotational position constitutes a projection. For objects fitting within the angular width of the detector array, a scan may involve acquiring x-ray counts for the 620 virtual detectors (i.e. for 620 "rays" per projection) at 360 angular positions (360 projections). For larger objects, some translations may be also required. Acquiring a full data set (620 virtual detectors, 360 projections) for imaging one slice through an object requires about 2.5 hours.

A standard filtered back-projection algorithm is used to perform the tomographic reconstruction for the XRT system (cf. Herman, 1983; Howard, 1985). For the full data set indicated above, this method yields a resolution of about 1-2 line pairs per millimeter (a spatial resolution of about 0.25-0.50 mm).

2.2.2. RTR System

The RTR system employs a Pantak x-ray machine capable of producing x-ray photons with energies up to 0.3 MeV. These x-rays pass through the object and are incident on a gadolinium oxysulfide bare-phosphor screen, which is imaged using a RS170 intensified CCD camera at the standard video frame rate. The field of view for this system is the standard 14 inch × 17 inch (35.6 cm × 43.2 cm). No translation or rotation stages are routinely present for this system.

2.3. Gamma-Densitometry Tomography (GDT) Technique

One method of characterizing the phase volume fraction spatial variation is gamma-densitometry tomography (GDT). The basic physics of the interaction of gamma photons with matter is well known (cf. Meyerhof, 1967; Lapp and Andrews, 1972; Knoll, 1979; Lamarsh, 1983). In brief, there are three interaction mechanisms: the photoelectric effect, pair production, and Compton scattering. The first two are absorptive (the gamma photon disappears), whereas the last one is not (the energy and direction of the gamma photon change). These processes cumulatively yield a mass attenuation coefficient μ/ρ (units of cm^2/g), a constant depending only on the composition of the material and the gamma photon energy. The attenuation coefficient μ, roughly proportional to the electron density of the medium for the lighter elements and the gamma photon energies considered here, describes the attenuation of a gamma beam of intensity I passing along a path of length L through the material:

$$I = I_0 \exp(-\mu L).\tag{8}$$

If two or more materials are present along the path, a measurement of I/I_0 yields the average attenuation coefficient μ along the path, where the value of μ is linearly related to the volume fractions ε_i and their attenuation coefficients μ_i of the materials comprising the mixture:

$$\mu = \sum_i \varepsilon_i \mu_i, \text{ where the } \varepsilon_i \text{ are averaged over the path } L.\tag{9}$$

Measuring μ in this manner along many different paths provides the information needed to perform a tomographic reconstruction of the spatial variation of μ. The varieties of tomographic reconstruction algorithms which accomplish this are discussed in great detail elsewhere (e.g. Herman, 1983; Howard, 1985; Vest, 1985). If only two materials are present, the volume fraction spatial distribution of each material can be uniquely determined since the two volume fractions must sum to unity.

Investigators have long recognized the potential of GDT to study multiphase flows. A comprehensive review discussing applications of GDT to multiphase flows is provided by Munshi (1990). Typical

31

applications have included two-phase gas-liquid pipe flows for the nuclear industry (Hewitt, 1978), saturation measurements in porous media (Reda et al., 1981; Brown et al., 1993), gas-solid fluidized beds (MacCuaig et al., 1985; Dyakowski, 1996), gas-liquid flow in packed beds (Toye et al., 1996), particle-laden liquid flows (Shollenberger et al., 1997b), horizontal stratified three-phase pipe flow (Pan and Hewitt, 1995), and bubble columns (Kumar et al., 1995; Shollenberger et al., 1995ab; Adkins et al., 1996; Shollenberger et al., 1997a; Torczynski et al., 1995; Torczynski et al., 1996ac).

2.3.1. GDT System

The GDT system developed for this study is shown in Figure 12. It consists of a gamma source, a gamma detector, a multichannel analyzer for recording the gamma energy spectrum, a traverse for the source and detector, a PC for data acquisition, and software for count-rate analysis.
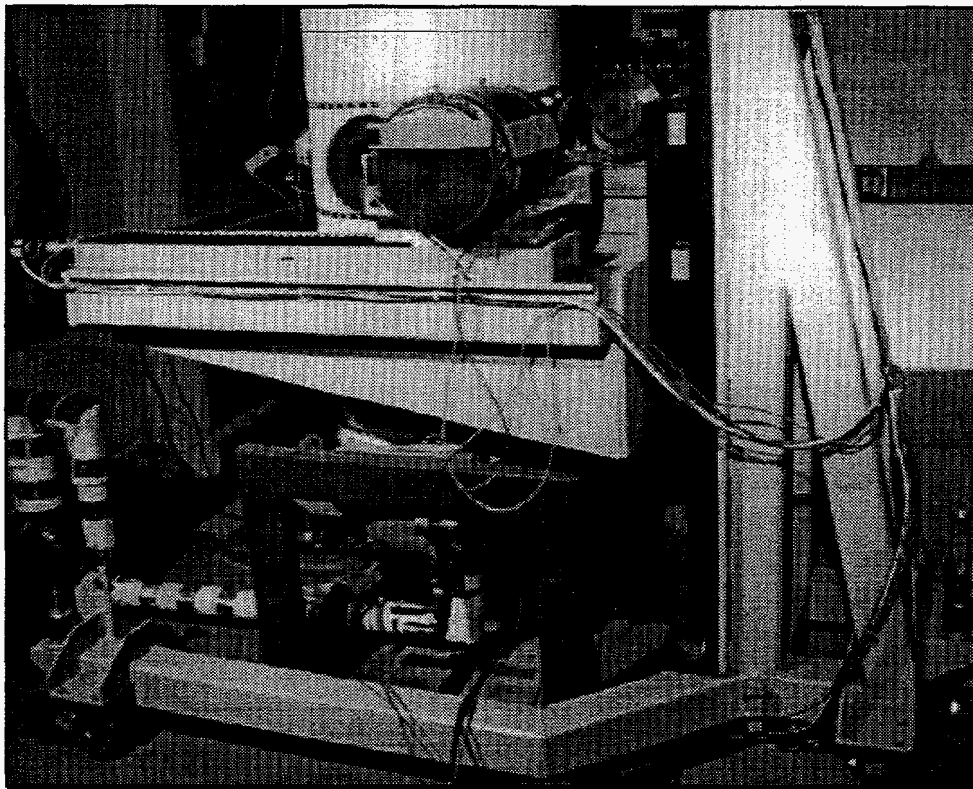
Figure 12. Gamma-densitometry tomography (GDT) system.

The gamma source used in the GDT system is a 5-Curie ^{137}Cs (cesium 137) isotope source. This isotope is fairly stable, having a half-life of roughly 30 years, and produces a fairly monoenergetic spectrum of gamma photons centered on 661.6 keV. The source is contained in a thick-walled cylindrical lead vault for safety purposes. A collimated beam is produced using a small-diameter aperture, for which diameters of 3.66 mm and 6.35 mm have been employed to date. The source is fully interlocked with an infrared sensor that activates the aperture-closure mechanism should a human be detected by the sensor. The aperture-closure mechanism has been designed to require a continual supply of power to remain open so that gravity-driven closure occurs if power is interrupted.

32

A scintillation detector is used to observe the individual gamma photons that pass through the scanned object without being scattered. The scintillation detector employs sodium iodide with thallium activator, NaI(Tl), in the form of a cylindrical crystal 7.62 cm in diameter and 7.62 cm long. The crystal is optically coupled to a photomultiplier tube (PMT) so that the flashes of light produced by individual photons can be observed. The detector crystal is water-cooled with active control to provide temperature stability and minimize thermal drift of the electronics. It is possible for gamma photons that are scattered by the scanned object to enter the detector, creating a spurious signal (see Figure 13). To minimize spurious acquisition of gamma photons that have been scattered through small angles, the detector is lead-shielded and a small-diameter aperture (3.66 mm or 6.35 mm) is placed in front of the detector to provide angular selectivity. The apertures on the source and detector also serve to collimate the gamma beam and thereby restrict the lateral extent of the region sampled by the source-detector combination for a particular position.
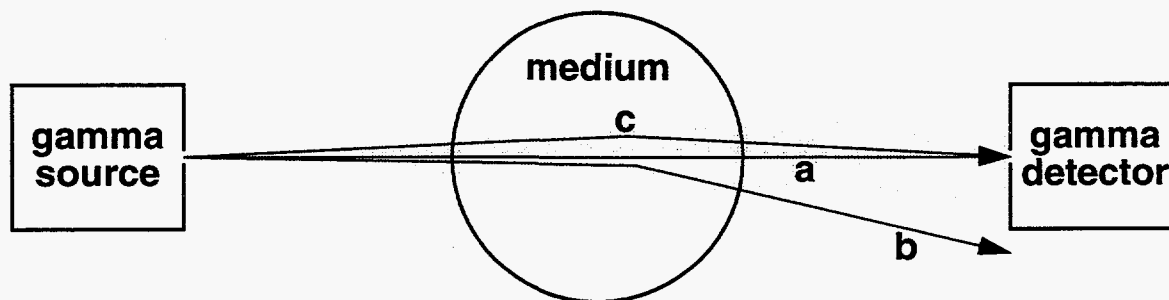
photon a = unscattered and counted (correct)
photon b = scattered and not counted (correct)
photon c = scattered but counted (erroneous)

Figure 13. A detector erroneously observes some of the scattered gamma photons.

A heavy-duty computer-controlled two-axis traverse, shown schematically in Figure 14, is used to support, align, and position the source and the detector. The traverse is configured in a U-shape formed by two opposing arms, on which the source and the detector are mounted. The arms have 66 cm of clearance to accommodate large testbeds, and the traverse has 60 cm of travel in both the horizontal and the vertical directions. The U-shaped configuration allows the traverse system to be positioned easily around the testbed to be scanned and to be moved without difficulty from one testbed to another. The motion of the traverse is fully automated. A scan direction (vertical or horizontal), a step size (distance from one path to the next), and a time to collect counts are specified, and the traverse software automatically moves the source-detector combination to the correct position for the correct amount of time, where positions are determined by detection of positional changes in an encoder rotating with the traverse drive shafts. If a source-detector misalignment of more than 1 mm is detected, the gamma system is automatically shut down in the manner discussed above.
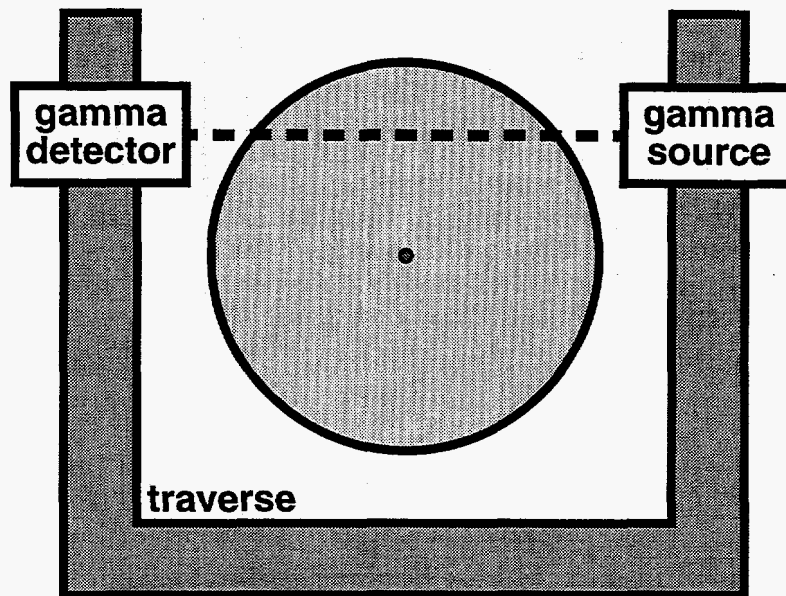
Figure 14. Schematic diagram of traverse for source and detector.

A multichannel analyzer (MCA) is used to measure the energy spectrum of the gamma photons so that the count rate can be determined. More accurately, the MCA measures the spectrum of the electrical pulses from the PMT that are produced by the light flashes from the sodium iodide crystal when gamma photons are incident on it. Typically, 720 contiguous bins are used to span the energy region from 0 to roughly 1400 keV. The MCA operates by acquiring data for a prescribed counting duration, the "live time". However, it requires a finite interval of time to record each count and cannot record additional counts that occur during those intervals, the "dead time". As a result, the total time needed to acquire a spectrum, the "wall-clock time", is somewhat longer than the live time. Calculations of count rates use the number of counts and the live time.

Some typical spectra observed with the MCA are shown in Figure 15. There are several distinguishing features on each of these curves that can be related to Compton-scattering phenomena and detector performance. First, the largest peak occurs within a 100 keV wide region centered at 661.6 keV and represents ^{137}Cs primary photons that reached the detector without being attenuated in the medium and that were completely absorbed in the crystal. The broadening of this peak is due to the light flash brightness distribution produced by the scintillation detector, and similar spreading occurs at all energies in the spectrum. A distinguishable feature to the left of the ^{137}Cs peak is a "shelf" occurring below 477.3 keV (the maximum energy that a photon can transfer to an electron in a single Compton-scattering event). Since there is a continuum of electrons up to this energy, the small peak at the shelf edge is located slightly below 477.3 keV after broadening, as shown in Figure 15. Further left along the spectrum is a peak that represents ^{137}Cs photons Compton scattered off the back of the detector vault and then absorbed by the detector crystal. The energy of these photons is equal to 184.3 keV, the difference between 661.6 keV (the initial photon energy) and 477.3 keV (the energy required to Compton scatter a photon 180°, which is the maximum energy that can be imparted to an electron). Finally, to the right of the ^{137}Cs peak is a region representing two-photon processes, and the peak at 1323.2 keV (twice 661.6 keV) represents two 661.6 keV photons being absorbed in the crystal simultaneously.
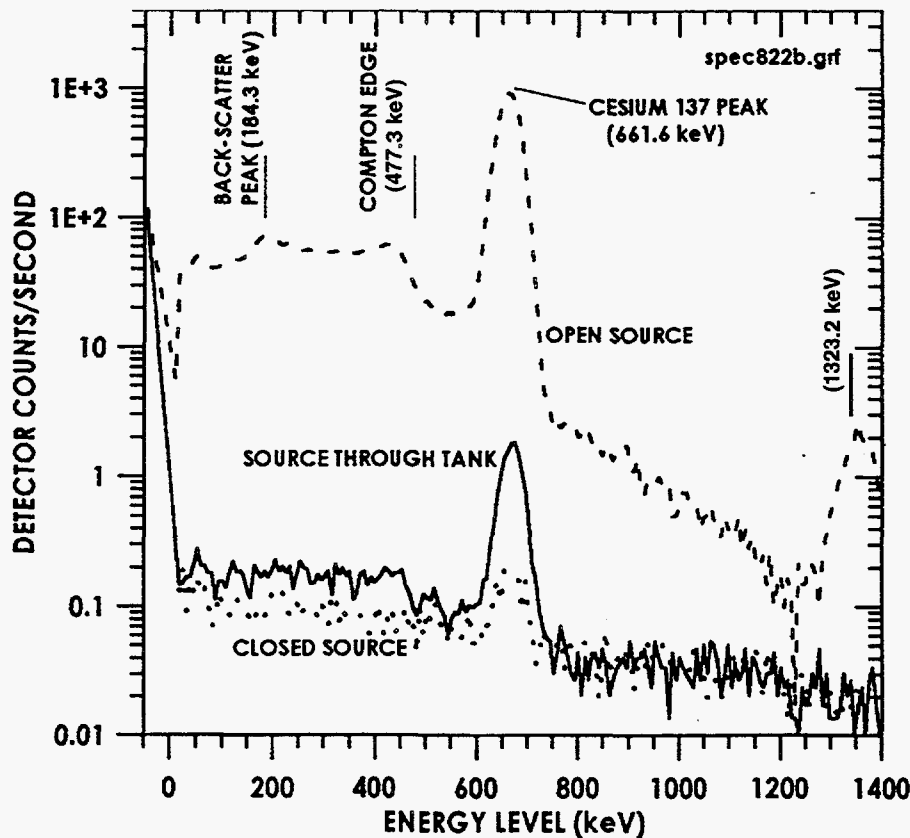
Figure 15. Gamma spectrum from the MCA with various features identified.

It is essential to recognize that the spectra shown in Figure 15 do not represent either the spectrum emitted by the source or the spectrum produced by passage of 661.6 keV photons passing through the testbed being scanned. Rather, the spectra result from the interaction of the 661.6 keV photons with the detector crystal. A 661.6 keV photon interacts with an atom of the detector crystal via Compton scattering or photoelectric absorption. Both of these interactions cause the ejection of one high-energy electron. For photoelectric absorption, this electron acquires all of the photon's energy, and the photon disappears. However, for Compton scattering, the electron acquires only a portion of the photon's energy, and the photon retains the remainder. This lower-energy photon travels in a different direction and can experience further interactions with the crystal. The larger the crystal, the more likely it is that the photon will ultimately experience photoelectric absorption and thus give up all of its energy to electrons. This effect is enhanced by the fact that photoelectric absorption is favored at low energies compared with Compton scattering, which is favored at 661.6 keV. The high-energy electrons lose their energy while passing through the crystal by exciting atoms, which then emit visible light as they return to their ground state. All of these interactions occur almost instantaneously, so a single light flash is observed per incident gamma photon. This light flash is detected and converted into a corresponding voltage by the PMT.

Unfortunately, the brightness of the light flash is related to the energy transferred from the photon to the crystal but cannot be used directly to infer the energy of the incident photon because even monoenergetic incident photons produce light flashes of significantly different brightness. To produce

35

a light flash corresponding to a photon transferring all 661.6 keV of its energy to the crystal, the sequence of interactions must be terminated within the crystal by a photoelectric absorption. If, however, a Compton-scattered photon escapes from the crystal prior to photoelectric absorption, the light flash corresponds to the energy difference between the incident photon and the escaping photon. For photons experiencing exactly one Compton-scattering event prior to escaping, these energies form a continuum from zero up to the maximum energy a photon can transfer to an electron in a single scattering event (477.3 keV for a 661.6 keV photon). This portion of the spectrum is called the Compton "shelf" or continuum. If a photon experiences more than one Compton-scattering event but escapes from the crystal, a light flash corresponding to an energy between 477.3 keV and 661.6 keV is produced a certain fraction of the time. These effects are mitigated by using a crystal large enough to ensure that most photons deposit all of their energy in the crystal. However, even if all photons transferred identical amounts of energy to the crystal, the resulting light flashes would still not have the same brightness. Rather, a brightness distribution results, with a deviation of roughly 9% about the average for NaI(Tl) crystals. Moreover, if two photons enter the crystal almost simultaneously, the combined light flashes often indicate an energy larger than 661.6 keV.

Count-rate spectra acquired using the MCA must be post-processed to yield the count rate corresponding to the unattenuated 661.6 keV photons from [137]Cs. This count rate and the exponential relation for attenuation yield the desired path-averaged attenuation coefficient, as needed for GDT. As discussed above, the observed spectrum is produced almost solely by 661.6 keV photons interacting with the sodium iodide crystal. More specifically, most of the counts at significantly different energies do not indicate that photons of these energies are present in the incident spectrum, which is nearly monoenergetic, or in the transmitted spectrum, which results from the incident spectrum passing through the testbed being scanned. Without a detailed knowledge of the precise form of the spectrum, however, it is impossible to predict rigorously the true number of counts for a spectrum. Initially, summation over a prescribed, fixed "window" of the energy spectrum was examined as a method of determining the count rate. This method, while conceptually simple and straightforward to implement, was not found to produce reliable results during validation experiments, particularly for cases with large attenuation. Subsequently, an approach was developed based on assuming that the spectrum is reasonably described by a Gaussian function in the vicinity of the peak (Knoll, 1979). A curve fit determines the best values for the center, the width, and the height of the Gaussian, and the count rate is determined from the analytical formula for the integration of a Gaussian. To perform the fit, it is necessary to select a fitting window, where only points of the spectrum within the window contribute to the fit. This window is determined adaptively from the measured spectrum so as to contain the 661.6 keV peak and the region around it. Of course, the accuracy of the fit, and hence of the count rate, relies on selecting an appropriate fitting window. However, this is not a particularly severe requirement since the fitting window is used only to determine the Gaussian and not to perform the integration. The above algorithm has been implemented in both Mathematica (Wolfram, 1996) and Fortran to verify its efficacy and was subsequently interfaced with the Labview data acquisition software and has the following steps.

1. Find the maximum count rate per energy bin for all bins in the vicinity of the 661.6 keV peak and the precise bin at which this maximum occurs.

2. Define left and right count-rate cutoff values (e.g. 70% and 10% of the maximum).

3. Find the first bin to the left of the peak where the count rate falls below the left count-rate cutoff and the first bin to the right of the peak where the count rate falls below the right count-rate cutoff. These bins define the fitting window.

4. Take the logarithm of the portion of the spectrum lying within this fitting window, and fit the logarithmic spectrum with a parabola:

$$\ln(dI/dB) = k_0 + k_1 B + k_2 B^2, \ k_2 < 0, \tag{10}$$

where B is the energy bin number, dI/dB is the count rate in energy bin B, and the k_i are the fitting coefficients.

5. The peak center B_p, the peak height I_h, the peak width B_w, and the peak area I (the detector count rate) are given by the following formulas for a Gaussian:

$$B_p = -\frac{k_1}{2k_2}, \ I_h = \exp(k_0 + k_1 B_p + k_2 B_p^2), \ B_w = \sqrt{\frac{-\pi}{k_2}}, \ I = I_h B_w. \tag{11}$$

A series of experiments was performed to validate the use of the MCA for GDT. The experiments consisted of measuring gamma spectra for transmission through various thicknesses of water. Lexan tanks with square inner cross sections of 10.16×10.16 cm (4.0×4.0 inch) and with inner lengths of 2.54, 5.08, 7.62, 10.16, 12.70, 15.24, and 30.48 cm (1.0, 2.0, 3.0, 4.0, 5.0, 6.0, and 12.0 inch) were used to contain the water. Two tanks were placed in series to extend the path length through water up to 45.72 cm (18 inch). Two combinations of source and detector collimators were used in these experiments: collimator diameters of 6.35 mm (0.25 inch) on both the source and the detector, and collimator diameters of 3.66 mm (0.144 inch) on the source and 3.175 mm (0.125 inch) on the detector. Spectra were always collected for a live time of 60 s. Figure 16 shows some of the gamma spectra measured using the MCA. The different curves in the plot represent different thicknesses of water between the source and detector, in 15.2 cm (6 inch) multiples. The previously discussed features of the spectra are clearly seen in these results. Note that, as the path length is increased, the attenuation above 661.6 keV is roughly double the attenuation below 661.6 keV, which confirms that the spectrum above 661.6 keV results from simultaneous absorption of two gamma photons.
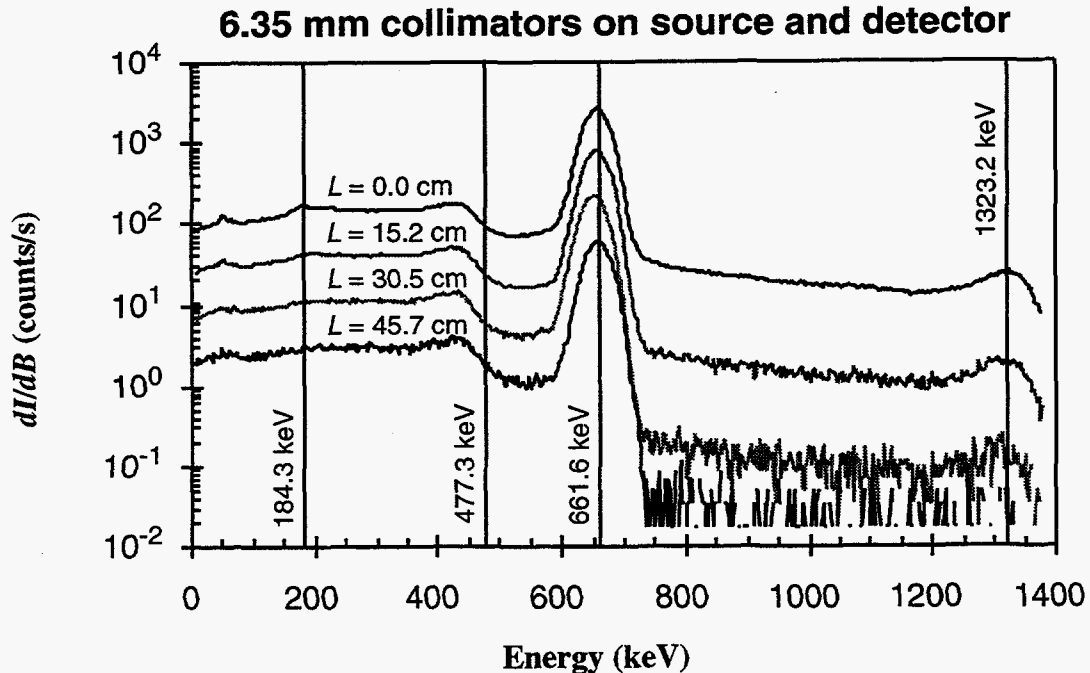
Figure 16. Gamma spectra from the MCA with various thicknesses of water.

The results of applying the algorithm discussed above to the data set shown in Figure 16 are shown in Figure 17. The fits are seen to be very good in the vicinity of the peaks regardless of the peak location or height, and the same fit quality is observed for all other data sets (not shown). Left and right cutoff values of 70% and 10% were used to determine the fitting window. Values of 60-80% for the left cutoff and 10-30% for the right cutoff gave almost identical results, but values of 50% for both cutoffs produced a fit that badly misrepresented the peak. The attenuation coefficient for water was determined to be $\mu_w = 0.0858 \pm 0.0002$ cm^{-1}, in close agreement with the known value (cf. Lamarsh, 1983). A related effort determined the attenuation coefficient of Lexan to be approximately 0.0917 ± 0.0010 cm^{-1}, which appears to be reasonable based on its presumed elemental composition.
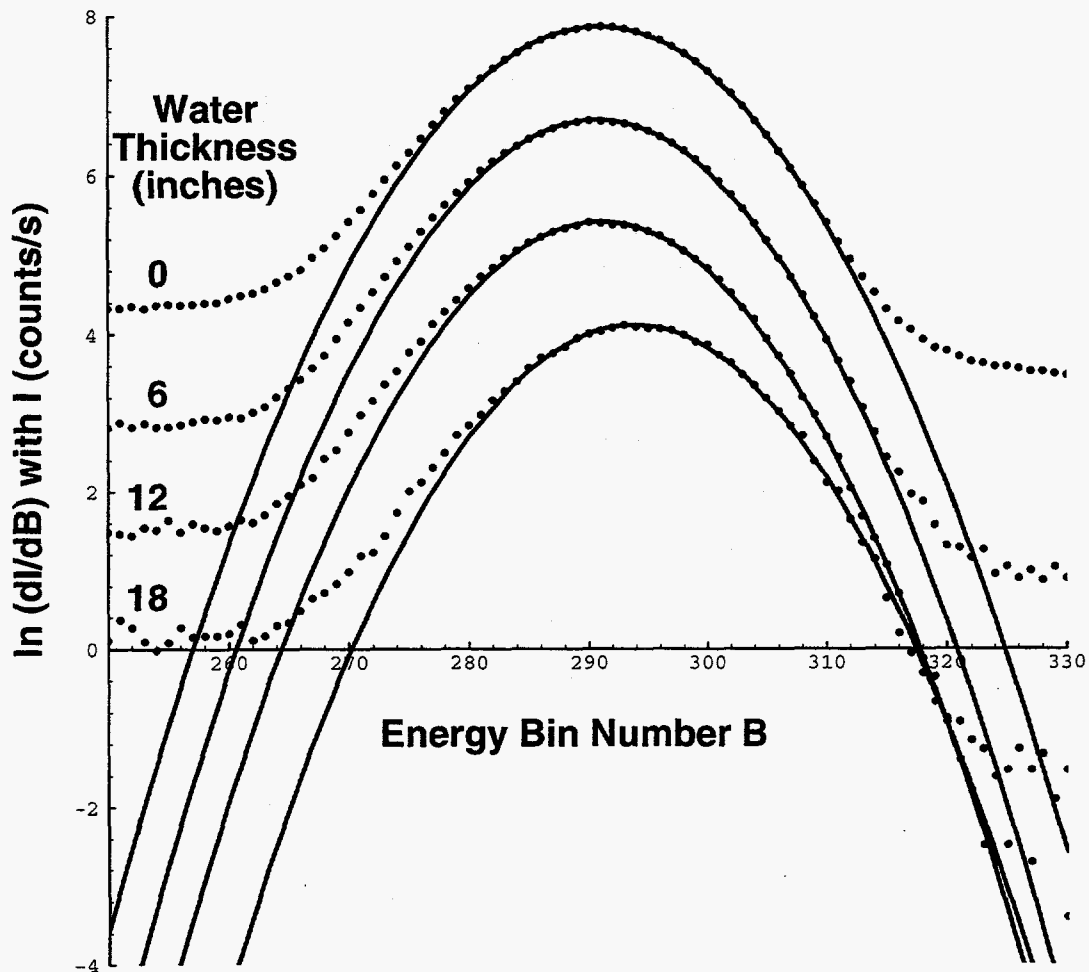
Figure 17. Logarithmic gamma spectra (points) and peak-fitting algorithm (curves).

The fact that the detector cannot respond infinitely fast has implications for data interpretation. If τ is the time required to "detect" a single gamma photon, measurements of count rates comparable to or exceeding $1/\tau$ will not yield accurate results (Reda et al., 1981). Reda et al. (1981) indicate that, for a real count rate I, the measured count rate is given by $I/(1 + \tau I)$. For the detection system discussed above, it appears that $\tau \leq 0.5$ μs, indicating that count rates below 20,000 counts/s are measured with better than 1% accuracy.

38

2.3.2. GDT Reconstruction Algorithm

The goal of tomographic reconstruction algorithms is to convert average quantities along paths passing through the testbed into the spatial variation of the quantity throughout the region of interest. In general, many "projections" (groups of paths lying in a plane and sharing either a common origin or a common direction) are required to produce an accurate reconstruction of the spatial variation within this plane. Three-dimensional variations are then built up from multiple planes. Under the simplifying assumption of an axisymmetric spatial variation within a plane, only one projection is required since the field appears the same when viewed from different angular directions.

The Abel transform (cf. Vest, 1985) can be used to reconstruct the axisymmetric spatial variation of a function $f(r, R)$ from its line integral $g(x, R)$ along the path in the y direction at horizontal position x, as shown in Figure 18.
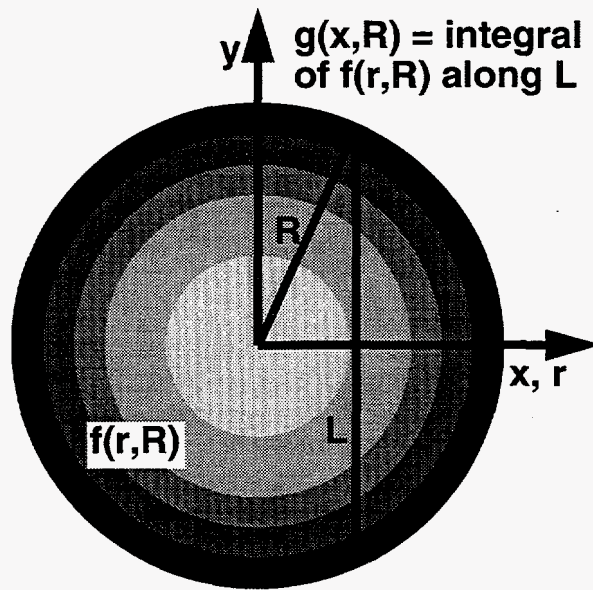
Figure 18. Schematic diagram of Abel transform geometry.

With these definitions, the Abel transform relates $f(r, R)$ and $g(x, R)$ in the following manner:

$$g(x, R) = 2\int_0^{\sqrt{R^2 - x^2}} f(\sqrt{x^2 + y^2}, R)dy = 2\int_x^R \frac{f(r, R)r}{\sqrt{r^2 - x^2}}dr, \; f(r, R) = -\frac{1}{\pi}\int_r^R \frac{(dg/dx)}{\sqrt{x^2 - r^2}}dx. \tag{12}$$

A quantity that arises naturally in axisymmetric tomography is ψ, the "path-averaged" value of f:

$$\psi(x, R) = \frac{g(x, R)}{2\sqrt{R^2 - x^2}}, \tag{13}$$

which is the line integral of f along the path at x divided by the path length. The functions f and ψ have a remarkable property that is useful to Abel tomographic reconstruction algorithms: if one function is an even polynomial, then the other function is also an even polynomial of the same degree.

For the representations

$$f(r, R) = \sum_{m=0}^{N} a_m (r/R)^{2m}, \; \psi(x, R) = \sum_{n=0}^{N} b_n (x/R)^{2n}, \tag{14}$$

the following reconstruction relations are obtained:

$$a_m = \sum_{n=0}^{N} c_{mn} b_n, \; b_n = \sum_{m=0}^{N} d_{nm} a_m, \tag{15}$$

where in terms of binomial coefficients

$$c_{mn} = \begin{cases} -\left[\dfrac{2m+1}{2^{2n}(2n-2m-1)}\right] \begin{pmatrix} 2n-2m \\ n-m \end{pmatrix} \begin{pmatrix} 2m \\ m \end{pmatrix}, & m \le n \\ 0, & m > n \end{cases}, \tag{16}$$

$$d_{nm} = \begin{cases} \left[\dfrac{2^{2n}}{2m+1}\right] \begin{pmatrix} 2m-2n \\ m-n \end{pmatrix} \Bigg/ \begin{pmatrix} 2m \\ m \end{pmatrix}, & n \le m \\ 0, & n > m \end{cases}. \tag{17}$$

GDT data are acquired and analyzed in the following manner. The attenuation field is the quantity of interest and is assumed to be axisymmetric, which is usually a good approximation for time-averaged bubble-column flow. Given the assumption of axisymmetry, reconstruction of the radial variation of the attenuation coefficient requires only one projection: the intensities I_i are measured at a series of horizontal source-detector positions x_i while the vertical source-detector position z is held constant. To acquire the data needed to reconstruct the phase volume fraction spatial variations, this type of data is acquired for three different circumstances. First, a scan is performed with the column "empty" (i.e. empty of liquid but full of gas). Second, a scan is performed with the column "full" (i.e. full of liquid but empty of gas). Third, additional scans are performed with the gas-liquid multiphase flow at the desired conditions. The following expressions then relate f and ψ to the attenuation coefficient μ:

$$f = \frac{\mu - \mu_G}{\mu_L - \mu_G}, \; \psi = \frac{\ln(I^{\text{empty}}) - \ln(I^{\text{flow}})}{\ln(I^{\text{empty}}) - \ln(I^{\text{full}})}. \tag{18}$$

Tomographic reconstruction proceeds in the following manner.

1. Measure the values ψ_i on a set of paths x_i.

2. Fit the $\{(x_i, \psi_i)\}$ with even powers of x_i/R to find the b_n.

3. Use the c_{mn} to find the a_m and the normalized attenuation radial variation f.

Note that for a two-phase gas-liquid flow, f is equal to the liquid volume fraction ε_L in the medium and hence is zero for pure gas and unity for pure liquid. In a three-phase flow, additional information is needed to relate f to the phase volume fractions.

2.4. Electrical-Impedance Tomography (EIT) Technique

Another method of characterizing material distribution is electrical-impedance tomography (EIT). EIT techniques have been discussed extensively in the recent review by Ceccio and George (1996). The underlying physical basis of EIT is the assumption that the impedance of a mixture can be sensibly related to the volume fractions and impedances of the materials comprising the mixture so that spatially resolved impedance measurements yield information about the spatial distribution of the materials in the mixture. If a gas-liquid mixture is considered where the gas is insulating and the liquid is purely resistive with conductivity σ_L, the Maxwell-Hewitt relation for a random dispersion of small insulating spheres (gas bubbles) within a continuum (the liquid) relates the mixture conductivity σ_m to the gas volume fraction ε_G (cf. Hewitt, 1978; Ceccio and George, 1996):

$$\sigma_m/\sigma_L = \frac{1-\varepsilon_G}{1+(1/2)\varepsilon_G}, \quad \varepsilon_G = \frac{1-(\sigma_m/\sigma_L)}{1+(1/2)(\sigma_m/\sigma_L)}. \tag{19}$$

Figure 19 shows a schematic diagram of a generic EIT setup. A region of material is surrounded by an insulating boundary on which several electrodes are mounted. A known current is injected into the material from one electrode and is withdrawn from another, and voltages are measured at all electrodes (both current-carrying and those that carry no current). This process is repeated for different pairs of electrodes until all combinations of electrodes have been examined. Tomographic reconstruction techniques are subsequently applied to determine the spatial variation of the electrical conductivity of the medium under examination. Note that reconstruction algorithms are necessarily considerably more complex for EIT than for GDT: the current paths through the material depend on the impedance distribution, whereas the gamma-photon paths through the material are known a priori since they are independent of the material distribution.
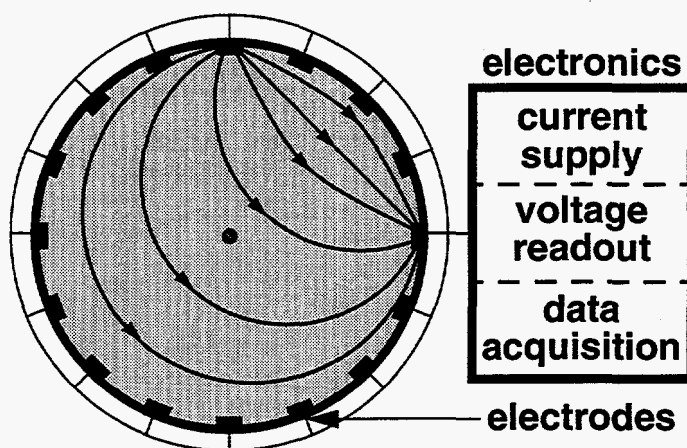
Figure 19. Schematic diagram of electrical-impedance tomography (EIT).

The methodology, efficiency, and accuracy of various EIT techniques continue to be a subject of research (e.g. Barber et al., 1983; Yorkey et al., 1987; Webster, 1990; Hua and Woo, 1990; Jones et al., 1993; Lin et al., 1993; O'Hern et al., 1995ab; Dickin and Wang, 1996; Loh and Dickin, 1996; Savolainen et al., 1996; Torczynski et al., 1996b; Shollenberger et al., 1997b; Mann et al., 1997). EIT techniques can be broadly grouped in terms of the problem dimensionality (2 or 3), the impedance model employed (e.g., resistive, capacitive), the numerical method used to discretize the equations

41

(e.g., finite-element method, boundary-element method), the representation of the impedance field (e.g., piecewise constant, exponential), the means by which the impedance field is modified during an iteration (e.g., back-projection between equipotential lines, Newton-Raphson), and the intended application (e.g., biomedical imaging, multiphase flow measurement).

The purpose of the present study is to implement an EIT technique suitable for making spatially resolved measurements of gas volume fraction in gas-liquid bubble-column flow. The medium is taken to be purely conducting (no capacitive effects), which is reasonable for polar liquids like water and which facilitates both hardware and software development. In contradistinction to the work of Lin et al. (1993), the emphasis here is not on the accurate determination of arbitrary gas-liquid interfaces or other sharp discontinuities in electrical properties. Instead, the medium under consideration (a continuum liquid phase within which a very large number of small gas bubbles are dispersed) is assumed to have smoothly varying electrical properties when averaged over length scales large compared with the bubble size and separation but small compared with the extent of the medium. Since variations of macroscopic quantities is gradual in the vertical direction for bubble-column flow, the electrical properties of the medium are assumed to have no variation in this direction, so the technique is two-dimensional, at least in this sense. Two reconstruction techniques have been examined: one employing a finite-element method with a Newton-Raphson scheme for minimization and the other employing a boundary-element method with Powell minimization.

2.4.1. EIT System
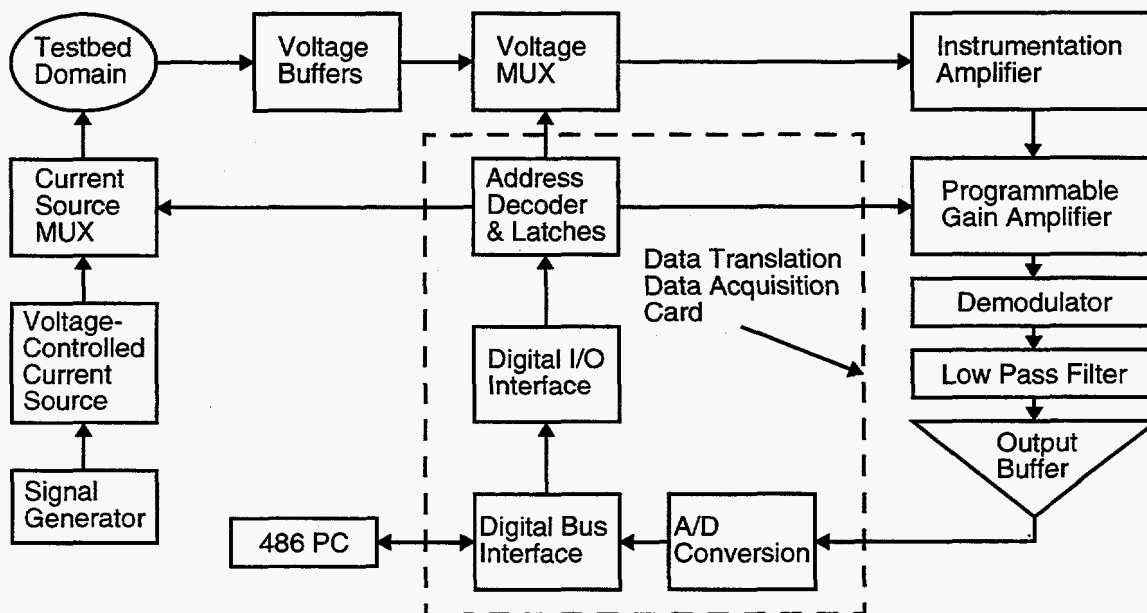
Figure 20. Block diagram of EIT hardware.

The EIT system developed herein consists of an electrode array mounted on a probe ring, a signal generator, a voltage-controlled current source (VCCS), multiplexers (MUXes) to and from the electrode array, an instrumentation amplifier, phase-sensitive demodulators, and a digital controller. A block diagram of the system is shown in Figure 20. The EIT system sources and sinks current at two ports, and voltages at all ports are measured relative to the sink port. The domain is excited with

a 50 kHz AC electric field, a frequency acceptable for air-water systems (cf. Ceccio and George, 1996). The injection current is created by a VCCS employing two operational amplifiers in a positive feedback design. Extremely high domain impedances should be avoided to prevent saturation of the VCCS. To acquire a set of projections with a good signal-to-noise ratio, significant current should be induced within the entire domain so as to produce measurable changes in the boundary voltages. This can be achieved by requiring a complete EIT measurement to utilize all distinct pairs of ports (without regard to order) as the source and sink ports. For N_e electrodes in the EIT setup, a complete EIT measurement consists of measuring the voltages $v_k^{(mn)}$ at all electrodes k for all $N_e(N_e-1)/2$ distinct pairwise combinations (mn) of electrodes, where electrodes m and n are the source and the sink. Thus, a complete measurement yields $N_e^2(N_e-1)/2$ voltage measurements. However, only $N_e(N_e-1)/2$ pieces of information are obtained, which correspond to the maximum number of independent resistors needed to describe an N_e-port resistive network (cf. Ceccio and George, 1996).

The electrode array is connected to the current source and sink via analog MUXes. MUXes are also used to connect the electrode array to the differential amplifier used to measure electrode voltages. Coaxial cable is used to carry the injection current to and from the electrodes surrounding the domain, and the shields of the cable are brought to the electrode voltage with voltage followers. A separate set of cables is used to connect the electrodes to the voltage MUXes to prevent the inclusion of any voltage drop occurring across the current lines, and the voltages on each electrode are buffered with a single operational amplifier. These voltage signals are passed to a differential amplifier which is used to measure the difference between the voltages on two electrodes. The differential amplifier has a good common mode rejection ratio (CMRR) and allows the measurement of voltage differences over a wide dynamic range.

The signal from the differential amplifier is demodulated with a phase-sensitive demodulator (PSD). Two demodulators are used to recover the in-phase and quadrature portion of the signal amplitude. The in-phase and quadrature demodulator output is low-pass filtered with a cutoff frequency of 25 kHz. The two voltage outputs of the PSD are then buffered and passed to the analog-to-digital converter on the digital controller board. A digital controller is used to select the current injection electrodes and perform the voltage measurements as well as acquire the demodulated signal levels. The data acquisition rate is 200 kHz, so the signal must be sampled at least four times to capture one period. Voltages are typically measured 64 times at each electrode to ensure an accurate average. An analog/digital interface is used to connect a PC to the EIT system.

The EIT system herein employs 16 electrodes, and these electrodes are placed at equal azimuthal intervals around the inner perimeter of a lucite cylindrical sections referred to as probe rings. The probe rings fabricated for this study have an inner diameter of 19.05 cm (7.5 inch) and can be used in two configurations, shown in Figure 21. If the ends are capped off, a probe ring can be used to study static objects immersed in water for validation experiments. If installed in a gas-liquid bubble column, a probe ring can be used to measure the material spatial distribution of a multiphase flow. Two types of electrodes have been employed, as shown in Figure 21: 0.25 inch $\times$ 3.0 inch strips of 0.003 inch-thick stainless steel referred to as strip electrodes, and 3 mm (0.125 inch) disks referred to as point electrodes. The principal advantage of using strip electrodes is that two-dimensional electric fields are obtained if the strip lengths are at least twice the probe ring diameter and if the conductivity field does not vary along the length of the strips. Unfortunately satisfying the first condition typically falsifies the second condition. Thus, three-dimensional solutions for the electric field are required, so point electrodes are preferred because they minimize the extent of the domain required by computational simulations. The principal disadvantages of point electrodes are that somewhat larger voltages are required to achieve the same current flow and that somewhat lower sensitivity is achieved. These are partially offset, however, by ease of construction, mounting, and alignment, high mechanical integrity even during vigorous flow, and good size-scaling properties.

ELECTRODE TYPES
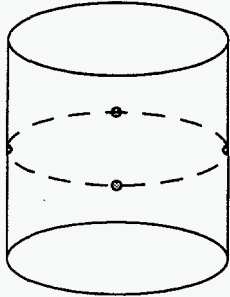
PROBE-RING INSTALLATIONS
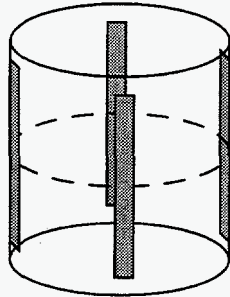
point
electrodes
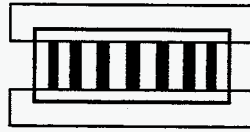
strip
electrodes

capped ends
for validation
experiments

bubble-column
installation for
multiphase flow
experiments
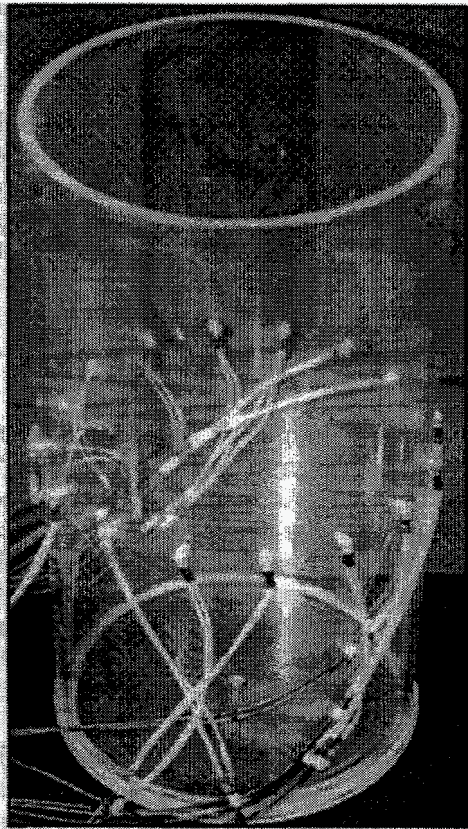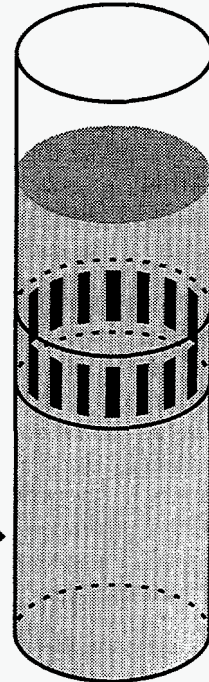
point
electrodes
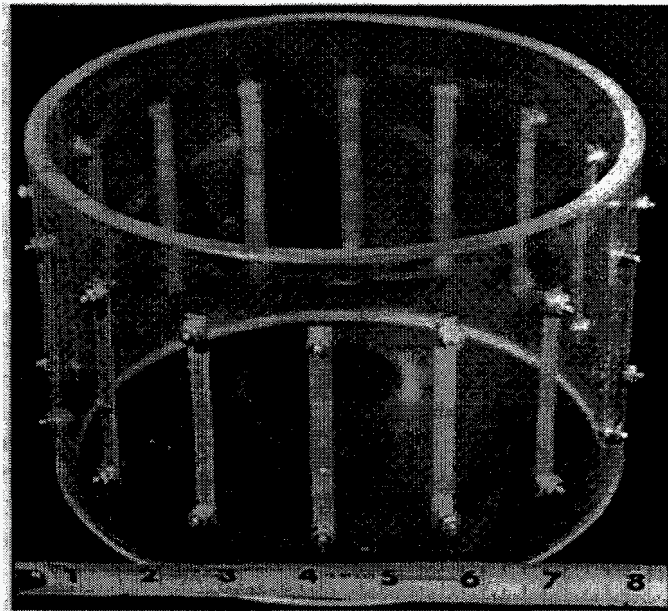
strip
electrodes

Figure 21. EIT strip and point electrodes and probe-ring installations.

2.4.2. EIT Reconstruction Algorithm: Overview

electrodes

tomographic reconstruction algorithm

measured currents and voltages

reconstructed impedance field
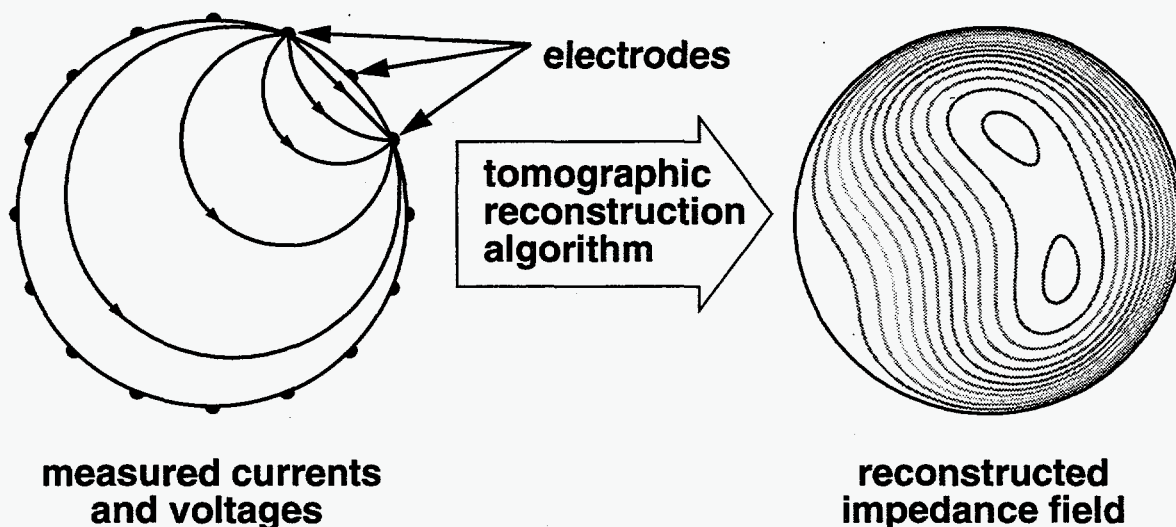
Figure 22. Schematic diagram of EIT.

As shown in Figure 22, for N_e electrodes and $N_e(N_e-1)/2$ source-sink combinations, the goal of EIT is to use the $N_e^2(N_e-1)/2$ experimental voltages at the electrodes on the boundary to infer the impedance distribution in the interior. As previously indicated, reconstruction algorithms are considerably more complex for EIT than for GDT since the current paths through the material depend on the impedance distribution, whereas the gamma-photon paths through the material are known a priori to be straight lines. Thus, EIT tomographic reconstruction algorithms continue to be a subject of research (e.g Yorkey et al., 1987; Webster, 1990; Hua and Woo, 1990; Jones et al., 1993; Ceccio and George, 1996). In this study, the basic approach of Yorkey et al. (1987) has been followed. The medium is taken to be purely resistive (no capacitive effects), the conductivity spatial distribution is adjusted until the computational voltages most closely match the experimental voltages. The finite-element method (FEM) is used to discretize the voltage equation, and a Newton-Raphson (NR) method is used to minimize the rms difference between the computational and experimental voltages. This approach is developed generally and is implemented for two-dimensional situations and for three-dimensional situations with only radial variations in the conductivity field.

The physical model describing current flow in a purely resistive medium is the combination of steady charge conservation and Ohm's Law:

$$\nabla \cdot \mathbf{J} = 0, \tag{20}$$

$$\mathbf{J} = -\sigma\nabla V, \tag{21}$$

which yield

$$\nabla \cdot [\sigma\nabla V] = 0 \text{ in the domain,} \tag{22}$$

$$J_n = \mathbf{n} \cdot \mathbf{J} = -\mathbf{n} \cdot \sigma\nabla V \text{ on the boundary,} \tag{23}$$

45

where V is the voltage (in V), σ is the conductivity (in $\Omega^{-1}m^{-1}$), $\mathbf{J}$ is the current flux vector (in A/m^2), and $\mathbf{n}$ is the unit normal vector pointing outward on the domain boundary. The equation describing the voltage field is of the Laplace form, so proper boundary conditions require specifying either V (Dirichlet condition) or J_n (Neumann condition) everywhere on the boundary. For the situation considered here, J_n is specified everywhere on the boundary. For this specification to be consistent, the total current flow out of (and into) the domain must be zero. This is satisfied since all of the current injected from one electrode into the domain is removed by another electrode. Since no voltage values are prescribed anywhere, a voltage field that is a solution to the above equations is unique only to within an arbitrary additive constant. To remove this ambiguity so that a solution can be obtained, the voltage must be specified at exactly one point in the domain. If the solution so obtained is offset by any arbitrary amount, the result is also a solution to the equations. Effectively, this means that each voltage solution has an arbitrary voltage offset as an adjustable parameter available to minimize the rms difference between the computational and experimental voltages.

Numerical solution of the Laplace equation describing the voltage field can be accomplished using a wide variety of standard methods. However, EIT has certain unusual features. The first is that the voltage equation is solved many times for the same conductivity field but with only slightly different boundary conditions, namely injection and withdrawal from different electrode pairs, as indicated previously. A numerical method should take advantage of this fact. The second feature is that the electrodes have small widths compared to the inter-electrode separation. It is therefore desirable to replace these small, distributed electrodes with infinitesimal electrodes (i.e. true mathematical points) in computations to avoid excessive resolution requirements in the vicinity of an electrode. These infinitesimal electrodes are taken to be two-dimensional points for strip electrodes and three-dimensional points for point electrodes. One difficulty with this replacement is that the electrode voltage scales inversely with the electrode width and formally becomes infinite (as does the current flux) if the distributed electrodes are replaced with mathematical points. Fortunately, this difficulty is circumvented in discretized forms of the voltage equation since the finite spatial resolution of the discretization prevents infinite values from occurring. Another difficulty with this replacement is that the voltages determined at current-carrying electrodes (the source and the sink) are no longer correctly determined. However, since they depend sensitively on the electrode geometry and the unknown contact resistance between the electrode and the conducting medium, the voltages at current-carrying electrodes should not be used when minimizing the rms difference between the computational and experimental voltages. This results in the loss of N_e pieces of information, the unknown N_e contact resistances.

It is convenient to nondimensionalize the physical quantities of interest in the following manner. Without loss of generality, assume that the current passing between each source-sink electrode pair is always the same and is described in terms of a current I_e (in A) and a length scale R (in m) by the current per unit length I_e/R for infinitesimal strip electrodes and by the current I_e for infinitesimal point electrodes. Also without loss of generality, assume that the medium under examination has an average conductivity on the order of the constant σ_0. Then the nondimensionalization presented in Table 1 is appropriate, and the symbols denoting dimensional quantities will be used to denote nondimensional quantities without exception for the remainder of this section.

Table 1. Nondimensionalization employed in EIT theoretical development.

Quantity	Dimensional	Nondimensional
Position	$\mathbf{x}$	$\mathbf{x}/R$
Conductivity	σ	σ/σ_0
Current Flux	J_n	$R^2 J_n/I_e$
Voltage	V	$\sigma_0 R V/I_e$

electrodes = 1,2,3,4
reference point = 0
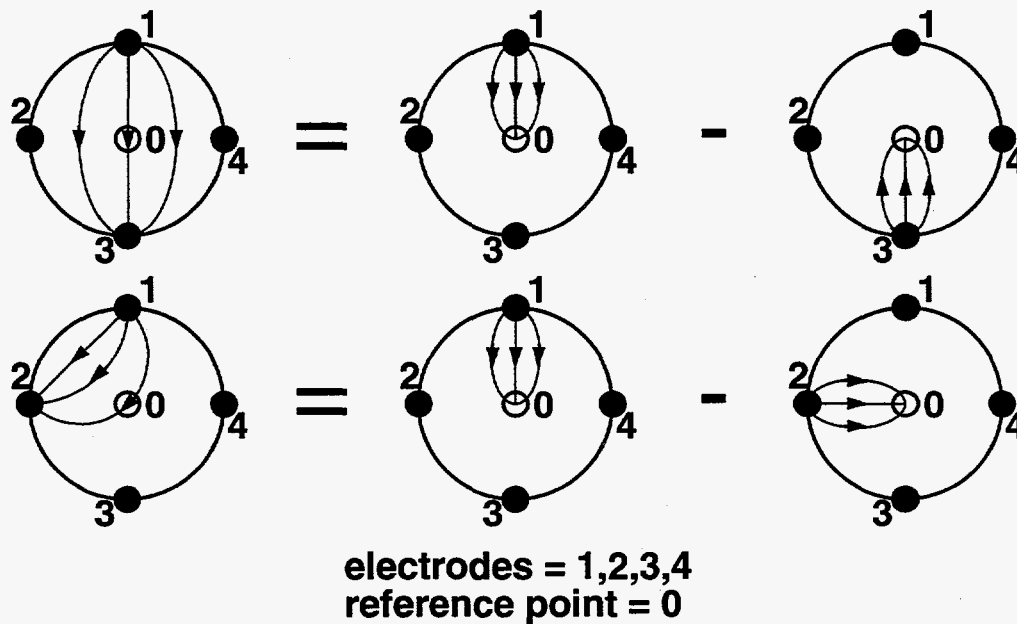
Figure 23. Linearity allows all EIT solutions to be built up from fewer solutions.

A considerable reduction of computational work can be achieved through application of the principle of linearity, as illustrated in Figure 23. As previously indicated, to determine the solution uniquely, the voltage must be specified at one point, henceforth called the reference point and denoted by "0". Suppose that the solution $V^{(k)}(\mathbf{x})$ corresponding to current injection at electrode k and current withdrawal at the reference point has been determined for all electrodes. Then the solution $V^{(mn)}(\mathbf{x})$ for the EIT case with current injection and withdrawal at electrodes m and n, respectively, can be built up using the linearity of the voltage equation (as shown in Figure 23) using the relation

$$V^{(mn)}(\mathbf{x}) = V^{(m)}(\mathbf{x}) - V^{(n)}(\mathbf{x}). \tag{24}$$

Thus, for N_e electrodes, only N_e solutions are required to determine all $N_e(N_e-1)/2$ EIT solutions. This economy is also achieved for computation of the Jacobians discussed later.

2.4.3. EIT Reconstruction Algorithm: Theory

For a two-dimensional system (i.e. with infinitesimal strip electrodes), the field equation and boundary condition for the voltage field $V^{(k)}(\mathbf{x})$ are as follows:

$$\nabla \cdot [\sigma \nabla V^{(k)}] = \delta(x)\delta(y) \text{ in the domain,} \qquad (25)$$

$$\mathbf{n} \cdot \sigma \nabla V^{(k)} = \delta(s - s^{(k)}) \text{ on the boundary,} \qquad (26)$$

where s is the arc length along the boundary, $s^{(k)}$ is the location of electrode k, δ is the Dirac delta function, and the reference point is placed at the origin without loss of generality. The delta-function terms in the field equation and the boundary condition represent current flow out of the domain at the reference point and into the domain from electrode k, respectively. For a three-dimensional system (i.e. with infinitesimal point electrodes), the single delta function in the boundary condition is replaced by the product of two delta functions in the coordinates needed to define the two-dimensional boundary surface, and the product of two delta functions in the field equation is replaced by a product of three delta functions in all three coordinates.

A Galerkin finite-element method (FEM) is used to discretize the voltage field:

$$V^{(k)}(\mathbf{x}) = \sum_{j=0}^{N_n} \phi_j(\mathbf{x}) V_j^{(k)}, \qquad (27)$$

where $V_i^{(k)}$ is the voltage at node i and $\phi_i(\mathbf{x})$ is the (global) basis function for node i. The standard FEM procedure is applied to generate equations for the nodal values of voltage: multiply the above equation by $\phi_i(\mathbf{x})$, integrate over the entire domain, apply integration by parts, and insert the boundary condition to specify the flux on the boundary. As indicated above, one voltage must be specified to generate a unique solution. The voltage at the reference point, denoted node 0, is set equal to zero. The voltage equation results from this approach, where M_{ij} is the global stiffness matrix and δ_{ij} is the Kronecker delta:

$$\sum_{j=1}^{N_n} M_{ij} V_j^{(k)} = \delta_{ik}, \ M_{ij} = \int \sigma \nabla \phi_i \cdot \nabla \phi_j dx dy, \text{ for } i = 1, ..., N_n. \qquad (28)$$

Note that the voltage equation is not applied at the reference node $i = 0$.

The conductivity field in the voltage field above is represented as a function of position:

$$\sigma = \sigma(\mathbf{x}; \{C_\alpha\}), \text{ with } \alpha = 1, ..., N_\sigma, \qquad (29)$$

where the C_α are N_σ independent adjustable parameters. This representation can be fairly arbitrary so long as $0 < \sigma < \infty$. Although the conductivity functions subsequently used are global and typically smooth, these restrictions are not required in this development. The voltages $V_i^{(k)}$ depend on the conductivity parameters C_α in a complex way. This dependence can be simplified considerably if the voltages $V_i^{(k)}$ are linearized about the particular values $\{C_\alpha\}$. This necessitates computation of the Jacobians $\partial V_i^{(k)}/\partial C_\alpha$. The Jacobian equations are calculated directly from the voltage equation using the chain rule, where the $M_{\alpha ij}$ are the derivatives of the global stiffness matrix:

$$\sum_{j=1}^{N_n} M_{ij}\left(\frac{\partial V_j^{(k)}}{\partial C_\alpha}\right) = -\sum_{j=1}^{N_n} M_{\alpha ij} V_j^{(k)} \, , \; M_{\alpha ij} = \int\left(\frac{\partial \sigma}{\partial C_\alpha}\right)\nabla\phi_i \cdot \nabla\phi_j dxdy \, , \text{ for } \left\{ \begin{array}{l} i = 1, \, ..., N_n \\ \alpha = 1, \, ..., N_\sigma \end{array} \right. . \qquad (30)$$

Note that the global stiffness matrix appears on the left-hand sides of the voltage equation and all of the Jacobian equations (i.e. for all values of α). This affords considerable numerical economy since only one LU (lower triangular, upper triangular) decomposition of the stiffness matrix has to be performed to solve both the voltage equation and the Jacobian equation.

The reconstructed conductivity field is characterized by C_α values minimizing the rms difference between the computational and experimental EIT voltages excluding voltages from current-carrying electrodes. This necessitates adjusting the C_α to minimize the quantity

$$\Gamma = \frac{1}{2}\sum_{k=1}^{N_e}\sum_{(mn)} w_k^{(mn)}[V_k^{(mn)} + V_0^{(mn)} - v_k^{(mn)}]^2 \, , \text{ with } V_k^{(mn)} = V_k^{(m)} - V_k^{(n)} \, , \qquad (31)$$

where the $v_k^{(mn)}$ are the experimental EIT electrode voltages at electrode k for source electrode m and sink electrode n. The weights $w_k^{(mn)}$ are chosen to exclude current-carrying electrodes:

$$w_k^{(mn)} = \left\{ \begin{array}{l} 0 \text{ if } k = m \text{ or } k = n \\ 1 \text{ otherwise} \end{array} \right. . \qquad (32)$$

Note that arbitrary voltage offsets $V_0^{(mn)}$ have been included in this relation. It might be argued that there should be only N_e arbitrary voltage offsets $V_0^{(k)}$ appearing as the combination $[V_0^{(m)} - V_0^{(n)}]$ in the above equation rather than the $N_e(N_e-1)/2$ voltage offsets $V_0^{(mn)}$ that have been used. Under ideal circumstances, this would be correct. However, electronic and experimental complexities suggest that the larger number of voltage offsets is more appropriate.

Minimization of Γ is achieved by solving the following system for the C_α and the $V_0^{(mn)}$:

$$\frac{\partial \Gamma}{\partial C_\alpha} = 0 \, , \text{ for } \alpha = 1, \, ..., N_\sigma \, ; \; \frac{\partial \Gamma}{\partial V_0^{(mn)}} = 0 \, , \text{ for all } (mn) \, . \qquad (33)$$

This minimization results in the following system of nonlinear equations for the C_α:

$$0 = \sum_{k=1}^{N_\sigma}\sum_{p=1}^{N_\sigma}\sum_{(mn)} w_k^{(mn)} w_p^{(mn)}[(V_k^{(mn)} - V_p^{(mn)}) - (v_k^{(mn)} - v_p^{(mn)})]\left(\frac{\partial V_k^{(mn)}}{\partial C_\alpha}\right), \qquad (34)$$

where the $V_k^{(mn)}$ and the $V_p^{(mn)}$ are functions of the C_α.

Since these equations in this system are nonlinear, a Newton-Raphson (NR) technique is used to solve them iteratively. The voltages $V_k^{(mn)}$ and $V_p^{(mn)}$ (but not their derivatives with respect to the C_α) are linearized about a particular set of values for the C_α, where the departures c_α from these values are small. The departures c_α are found to satisfy the following system of equations:

$$\sum_{\beta=1}^{N_\sigma} A_{\alpha\beta}c_\beta = B_\alpha, \qquad (35)$$

where the matrix $A_{\alpha\beta}$ and the vector B_α are given by the relations

49

$$A_{\alpha\beta} = \sum_{k=1}^{N_\sigma} \sum_{p=1}^{N_\sigma} \sum_{(mn)} w_k^{(mn)} w_p^{(mn)} \left\{ \frac{\partial V_k^{(mn)}}{\partial C_\alpha} \right\} \left\{ \frac{\partial V_k^{(mn)}}{\partial C_\beta} - \frac{\partial V_p^{(mn)}}{\partial C_\beta} \right\}$$

$$= \frac{1}{2} \sum_{k=1}^{N_\sigma} \sum_{p=1}^{N_\sigma} \sum_{(mn)} w_k^{(mn)} w_p^{(mn)} \left\{ \frac{\partial V_k^{(mn)}}{\partial C_\alpha} - \frac{\partial V_p^{(mn)}}{\partial C_\alpha} \right\} \left\{ \frac{\partial V_k^{(mn)}}{\partial C_\beta} - \frac{\partial V_p^{(mn)}}{\partial C_\beta} \right\}, \tag{36}$$

$$B_\alpha = \sum_{k=1}^{N_\sigma} \sum_{p=1}^{N_\sigma} \sum_{(mn)} w_k^{(mn)} w_p^{(mn)} \left\{ \frac{\partial V_k^{(mn)}}{\partial C_\alpha} \right\} \{ [v_k^{(mn)} - v_p^{(mn)}] - [V_k^{(mn)} - V_p^{(mn)}] \}$$

$$= \frac{1}{2} \sum_{k=1}^{N_\sigma} \sum_{p=1}^{N_\sigma} \sum_{(mn)} w_k^{(mn)} w_p^{(mn)} \left\{ \frac{\partial V_k^{(mn)}}{\partial C_\alpha} - \frac{\partial V_p^{(mn)}}{\partial C_\alpha} \right\} \{ [v_k^{(mn)} - v_p^{(mn)}] - [V_k^{(mn)} - V_p^{(mn)}] \}. \tag{37}$$

The c_α values obtained in this manner are used to update the conductivity parameters according to $C_\alpha \to C_\alpha + c_\alpha$. Since linearized voltages were used to determine these values, the resulting C_α values will not minimize Γ exactly. However, repetitions of this Newton-Raphson process ultimately converge to the C_α values that minimize Γ.

The resulting algorithm starts from an initial guess for the C_α and proceeds as follows:

1. Compute the M_{ij} and $M_{\alpha ij}$ matrices:

$$M_{ij} = \int \sigma \nabla \phi_i \cdot \nabla \phi_j dx dy, \quad M_{\alpha ij} = \int \left(\frac{\partial \sigma}{\partial C_\alpha} \right) \nabla \phi_i \cdot \nabla \phi_j dx dy. \tag{38}$$

2. Perform the LU decomposition of M_{ij}.

3. Solve for the voltages $V_i^{(k)}$ and the Jacobians $(\partial V_i^{(k)} / \partial C_\alpha)$:

$$\sum_{j=1}^{N_n} M_{ij} V_j^{(k)} = \delta_{ik}, \quad \sum_{j=1}^{N_n} M_{ij} \left(\frac{\partial V_j^{(k)}}{\partial C_\alpha} \right) = -\sum_{j=1}^{N_n} M_{\alpha ij} V_j^{(k)}. \tag{39}$$

4. Compute the matrix $A_{\alpha\beta}$ and the vector B_α:

$$A_{\alpha\beta} = \sum_{k=1}^{N_\sigma} \sum_{p=1}^{N_\sigma} \sum_{(mn)} w_k^{(mn)} w_p^{(mn)} \left\{ \frac{\partial V_k^{(mn)}}{\partial C_\alpha} \right\} \left\{ \frac{\partial V_k^{(mn)}}{\partial C_\beta} - \frac{\partial V_p^{(mn)}}{\partial C_\beta} \right\},$$

$$B_\alpha = \sum_{k=1}^{N_\sigma} \sum_{p=1}^{N_\sigma} \sum_{(mn)} w_k^{(mn)} w_p^{(mn)} \left\{ \frac{\partial V_k^{(mn)}}{\partial C_\alpha} \right\} \{ [v_k^{(mn)} - v_p^{(mn)}] - [V_k^{(mn)} - V_p^{(mn)}] \}. \tag{40}$$

5. Solve for the c_α:

$$\sum_{\beta=1}^{N_\sigma} A_{\alpha\beta} c_\beta = B_\alpha. \tag{41}$$

6. Update $C_\alpha \to C_\alpha + c_\alpha$ and test for convergence.

One special choice of the functional dependence of σ on the C_α is of particular importance because it reduces by one the number of Jacobian matrices that must be computed:

$$\sigma = \frac{\sigma_1(\mathbf{x};\{C_\alpha\})}{C_1}, \text{ with } \alpha = 2, ..., N_\sigma, \tag{42}$$

where $0 < C_1 < \infty$. From the voltage equation, it is clear that all voltages are proportional to C_1:

$$V_k^{(mn)} = C_1 V_{k,1}^{(mn)}, \tag{43}$$

where the voltages $V_{k,1}^{(mn)}$ are computed for $C_1 = 1$ and are functions of the C_α for $\alpha = 2, ..., N_\sigma$. Minimization results in the following system of (slightly less) nonlinear equations for the C_α:

$$0 = \sum_{k=1}^{N_\sigma} \sum_{p=1}^{N_\sigma} \sum_{(mn)} w_k^{(mn)} w_p^{(mn)} [C_1(V_{k,1}^{(mn)} - V_{p,1}^{(mn)}) - (v_k^{(mn)} - v_p^{(mn)})] \left\{ \begin{array}{l} V_{k,1}^{(mn)} \quad \text{for } \alpha = 1 \\ \dfrac{\partial V_{k,1}^{(mn)}}{\partial C_\alpha} \text{ for } \alpha = 2, ..., N_\sigma \end{array} \right\}, \tag{44}$$

Linearization of the voltages about particular values of the C_α for $\alpha = 2, ..., N_\sigma$ yields the following linear system for the small departures c_α:

$$\sum_{\beta=1}^{N_\sigma} \tilde{A}_{\alpha\beta} \left\{ \begin{array}{l} C_1 \quad \text{for } \beta = 1 \\ C_1 c_\beta \text{ for } \beta = 2, ..., N_\sigma \end{array} \right\} = \tilde{B}_\alpha, \tag{45}$$

where the matrix $\tilde{A}_{\alpha\beta}$ and the vector $\tilde{B}_\alpha$ are given by the relations

$$\tilde{A}_{\alpha\beta} = \sum_{k=1}^{N_\sigma} \sum_{p=1}^{N_\sigma} \sum_{(mn)} w_k^{(mn)} w_p^{(mn)} \left\{ \begin{array}{l} V_{k,1}^{(mn)} \quad \text{for } \alpha = 1 \\ \dfrac{\partial V_{k,1}^{(mn)}}{\partial C_\alpha} \text{ for } \alpha = 2, ..., N_\sigma \end{array} \right\} \left\{ \begin{array}{l} V_{k,1}^{(mn)} - V_{p,1}^{(mn)} \quad \text{for } \beta = 1 \\ \dfrac{\partial V_{k,1}^{(mn)}}{\partial C_\beta} - \dfrac{\partial V_{p,1}^{(mn)}}{\partial C_\beta} \text{ for } \beta = 2, ..., N_\sigma \end{array} \right\}, \tag{46}$$

$$\tilde{B}_\alpha = \sum_{k=1}^{N_\sigma} \sum_{p=1}^{N_\sigma} \sum_{(mn)} w_k^{(mn)} w_p^{(mn)} \left\{ \begin{array}{l} V_{k,1}^{(mn)} \quad \text{for } \alpha = 1 \\ \dfrac{\partial V_{k,1}^{(mn)}}{\partial C_\alpha} \text{ for } \alpha = 2, ..., N_\sigma \end{array} \right\} \{[v_k^{(mn)} - v_p^{(mn)}]\}. \tag{47}$$

When this particular approach is used, the quantities C_1 and $C_1 c_\alpha$ for $\alpha = 2, ..., N_\sigma$ are the unknowns when solving the linear system. From these quantities, it is straightforward to determine the c_α for $\alpha = 2, ..., N_\sigma$. The c_α values obtained in this manner are used to update the conductivity parameters according to $C_\alpha \rightarrow C_\alpha + c_\alpha$ for $\alpha = 2, ..., N_\sigma$. Of course, the updated value of C_1 is determined directly. As previously indicated, since linearized voltages were used to determine these values, the resulting C_α values will not minimize Γ exactly. However, repetitions of this Newton-Raphson process ultimately converge to the C_α values that minimize Γ.

2.4.4. EIT Reconstruction Algorithm: FEMEIT Implementation

A computer code called FEMEIT has been written to implement the approach discussed in the previous section. Although intended for two-dimensional problems, FEMEIT was written so that development of a three-dimensional version would be straightforward. Although to date it has been applied only to circular domains, FEMEIT can handle general two-dimensional domains, including multiply connected domains and domains with internal electrodes, so long as electrode widths are small compared to inter-electrode distances. Since electrodes are represented as mathematical points, a node must be placed at each electrode. Currently FEMEIT uses 3-node linear triangle elements to assemble the M_{ij} and $M_{\alpha ij}$ matrices (a three-dimensional extension would probably use 4-node tetrahedrons). These elements, although of low order, were chosen for several reasons. The quantities $\nabla \phi_i \cdot \nabla \phi_j$ are constant within an element, which is both straightforward to implement and allows this quantity to be brought out from inside the integrals. Thus, the integration can focus on integrating the conductivity function over the elements, independent of the values of $\nabla \phi_i \cdot \nabla \phi_j$. Also, circular domains are easily filled using triangles. The conductivity function is chosen to be a global function and is currently selected from a library of choices in a subroutine. At present, Cartesian polynomials, radial polynomials, products of radial polynomials and sines and cosines, and a 5-parameter quadrant interpolation function are available. Incorporation of additional functional forms into this subroutine is straightforward. The integration of the conductivity function is performed using a 4-point quadrature over each triangular element. FEMEIT uses SLATEC subroutines for the solution of the linear systems and has been compiled on both Sun and IBM machines. A 15-parameter reconstruction of 16-electrode data using a mesh with 441 nodes requires somewhat under 2 minutes on the IBM.

FEMEIT requires four input data files. Examples of each are shown in Appendix A.

1. `nodelm.dat` This file contains the mesh information.

    (a) The first line has the number of nodes.

    (b) Subsequent lines have node number, node x, node y (1 node per line).
    Important: the last node must be an internal non-electrode node and will have zero voltage.

    (c) The first line after the nodes has the number of elements.

    (d) Subsequent lines have element number and node numbers (1 element per line).

2. `exinfo.dat` This file contains the electrode nodal locations.

    (a) The first line has the number of electrodes N_e.

    (b) Subsequent lines have the electrode number and the node number (1 electrode per line).

3. `exdata.dat` This file contains the experimental data. If there are N_e electrodes, then results for $N_e(N_e - 1)/2$ experiments are expected.

    (a) The first line for each experiment has the current-injecting electrode number, the current-withdrawing electrode number, and the current per unit length (in A/m).

    (b) Subsequent lines for each experiment have the electrode voltages (in V) given in order from electrode 1 to electrode N_e.

4. `conpar.dat` This file contains conductivity function and parameter information and convergence requirements.

    (a) The first line has the following six variables:

52

The maximum relative change in nodal conductivity per iteration.

Damping factor lower and upper bounds between 0 and 1. The relative change in the conductivity parameters is bounded by these parameters.

A tolerance on the relative change in the conductivity parameters. Iterations continue until the relative change falls below this value.

A tolerance on the relative degree to which the equations are satisfied. Iterations continue until the equations are satisfied to better than this value.

A geometric length scale used to normalize all coordinates, including those used within the selected model for σ.

(b) The second line has the following variables:

The maximum number of iterations.

An integer denoting the model for spatial variation of σ.

The number of conductivity (fitting) parameters used with this model.

The number of internal (nonvarying) parameters used with this model.

(c) The following lines contain:

Starting guesses for all the conductivity parameters.

Values for all the internal parameters.

FEMEIT performs some error checking to make sure that the correct number of parameters have been entered for the model selected. Five models have been implemented:

1. Sums of polynomials in x and y: $\sigma = \Sigma_\beta x^{m_\beta} y^{n_\beta} C_\beta$ with conductivity parameters $\{C_\beta\}$ and internal parameters $\{m_\beta\}$ and $\{n_\beta\}$ (integers). There are exactly twice as many internal parameters as conductivity parameters.

2. Sums of products of powers of r with functions of θ: $\sigma = \Sigma_\beta r^{m_\beta} \text{trig}(|n_\beta|\theta) C_\beta$ with conductivity parameters $\{C_\beta\}$ and internal parameters $\{m_\beta\}$ and $\{n_\beta\}$ (integers), where trig = cos if $n_\beta < 0$, trig = sin if $n_\beta > 0$, and trig = 1 if $n_\beta = 0$. There are exactly twice as many internal as conductivity parameters.

3. An axisymmetric piecewise linear interpolation in radius with $\sigma = C_\beta$ at $r = R_\beta$. There are equal numbers of conductivity and internal parameters. The radii R_β are supplied in ascending order. The last one must be the radius of the outer circle. The first one cannot be 0. The conductivity is constant at C_1 within the first radius.

4. A "bubble" centered at the origin with conductivity parameters C_1, C_2 and internal parameters P_1, P_2 such that $C_1 > 0$, $C_2 > 0$, $0 < P_1 < 1$, and $P_2 > 0$:

$$\sigma = C_1 \left\{ 1 + \frac{P_1}{2} \left[\tanh\left(\frac{r - C_2}{P_2}\right) - \tanh\left(\frac{r + C_2}{P_2}\right) \right] \right\}. \tag{48}$$

5. A "bubble" centered at (C_3, C_4): as above but having $r = \sqrt{(x - C_3)^2 + (y - C_4)^2}$ with conductivity parameters C_1, C_2, C_3, C_4 and internal parameters P_1, P_2 such that $C_1 > 0$, $C_2 > 0$, $0 < P_1 < 1$, and $P_2 > 0$:

FEMEIT produces three output data files. Examples of each are shown in Appendix A.

1. `parcon.dat` This file contains the values of the conductivity parameters at the end of the last iteration. Its format is essentially identical to `conpar.dat`, and it can be copied directly to `conpar.dat` if a restart is desired. It also shows the change in each parameter during the last iteration.

2. `nodcon.dat` This file contains the conductivity values at each node. Each line contains the node number, the conductivity at that node and the change in the conductivity at that node during the last iteration.

3. `iter.log` This file contains the iteration history (also written to the screen).

Several other smaller codes have been written to assist in validating and using FEMEIT.

1. `postfd` This code takes the FEMEIT output files and creates a FIDAP neutral file `postfd.fdneut`, which can be processed with `ficonv` and `fipost`.

2. `msheit` This code generates triangular element meshes for circles. It creates files `nemesh.dat` and `prinfo.dat`, to be copied to `nodelm.dat` and `exinfo.dat`. The origin is always the last node.

3. `ansoln` This code uses the analytical solution for the voltage field observed with a constant conductivity in a circular domain with a source at (x_0, y_0) and a sink at $(x_0, -y_0)$ to generate "numerical experimental data" in the file `andata.dat`, to be copied to `exdata.dat`.

$$V(x, y) = \left(\frac{I}{2\pi\sigma_0 R}\right)\ln\left[\frac{(y_0 + y)^2 + (x_0 - x)^2}{(y_0 - y)^2 + (x_0 - x)^2}\right]. \tag{49}$$

4. `fuldat` This code takes adjacent-electrode results from FIDAP simulations and uses linearity to create a full data set for all pairwise electrode combinations, which is contained in `fuldat.dat`, to be copied to `exdata.dat`.

FEMEIT is capable of reconstructing a conductivity field accurately so long as two things are true. First, the conductivity field must be capable of being represented by the conductivity function used by FEMEIT to describe it. Second, the FEM mesh used by FEMEIT must be adequate to represent both the solution and the conductivity function. Not only must there be sufficient nodes and elements, but also the elements in the vicinity of electrodes must have aspect ratios close to unity. The latter requirement arises from the singular behavior of the voltage near mathematical point electrodes, as discussed earlier. Failing this, excessive resolution may be needed near electrodes. Also, FEMEIT will not be able to return a conductivity field if it is allowed to use more parameters to represent the conductivity field than it has pieces of information (not data).

2.4.5. EIT Reconstruction Algorithm: FEMEIT Validation

Three approaches have been used to validate FEMEIT. The first involved comparison with the analytical solution for the voltage fields produced by infinitesimal strip electrodes in a circular domain when the conductivity is constant. The second involved a systematic mesh-refinement study of the reconstruction of a nontrivial conductivity field from voltages calculated by FIDAP using this conductivity field. The third involved comparison with a BEM code called 2DynaEIT developed by Dynaflow, Inc. (Duraiswami et al., 1995; O'Hern et al., 1995a) to determine the size and location of an insulating cylindrical inclusion (ICI) placed within a circular domain.

The first type of validation exercise involved using the analytical result for the voltage distribution with a constant conductivity σ_0 in a circular domain in which a current I/R per unit length is injected at the point (x_0, y_0) and withdrawn at the point $(x_0, -y_0)$:

$$V(x, y) = \left(\frac{I}{2\pi\sigma_0 R}\right)\ln\left[\frac{(y_0 + y)^2 + (x_0 - x)^2}{(y_0 - y)^2 + (x_0 - x)^2}\right]. \tag{50}$$

As in O'Hern et al. (1995), a 16-electrode EIT apparatus was considered. The codes `ansoln` and `fuldat` were used to generate the boundary voltages for all possible electrode pairs from the analytical solution. These boundary voltages, along with mesh information and specification of the conductivity function type, were the inputs to the FEMEIT code. For this study, the conductivity is taken to be an unknown constant (i.e. there was exactly one unknown parameter in the minimization of the rms voltage difference). In all cases examined, the conductivity value was correctly determined by FEMEIT when a moderate nodal density was employed (a few hundred nodes and elements).

The second type of validation exercise involved using the finite-element code FIDAP (Fluid Dynamics International, 1995) to compute the boundary voltages for a 16-electrode apparatus in the presence of a complicated electrical conductivity spatial distribution. The prescribed conductivity field is specified to be a linear combination of $\{1, x, y, x^2, xy, y^2, x^3, x^2y, xy^2, y^3, x^4, x^3y, x^2y^2, xy^3, y^4\}$ that goes to unity on the perimeter of the circular domain and dips to slightly below 0.4 in the upper right quadrant, as shown in the bottom right of Figure 24. This pattern was chosen to represent what might be observed if an excess of gas volume fraction were present in the upper right quadrant. FIDAP was used to solve the 16 adjacent-electrode conduction problems on the highly refined mesh of 9-node isoparametric quadrilaterals, shown in the bottom left of Figure 24, and `fuldat` was used to create a full EIT data set containing the results of all 120 distinct pairwise experiments. FEMEIT was used to analyze this numerically created data set. The conductivity field was represented by the function

$$\sigma = C_1 + C_2 x + C_3 y + C_4 x^2 + C_5 xy + C_6 y^2$$
$$+ C_7 x^3 + C_8 x^2 y + C_9 xy^2 + C_{10} y^3 + C_{11} x^4 + C_{12} x^3 y + C_{13} x^2 y^2 + C_{14} xy^3 + C_{15} y^4, \tag{51}$$

and 5 different meshes were examined, all of which are shown in Figure 24. Although mesh A, the most coarse mesh, did little more than indicate the rough amount of spatial variation in the conductivity field, mesh B, the next most coarse mesh, yielded a reasonable result. The most highly refined mesh employed here, mesh E, did an excellent job in reproducing the conductivity field. If the conductivity function $\sigma = C_1$ were used instead of the above conductivity function, FEMEIT with the most refined mesh yields a (uniform) conductivity of 0.603, which is a reasonable estimate of the average conductivity of the complicated conductivity field, $2/3$. Note that for this example, FIDAP has been used to generate a data set and to postprocess FEMEIT results but not to solve the FEM problems during the EIT reconstruction.
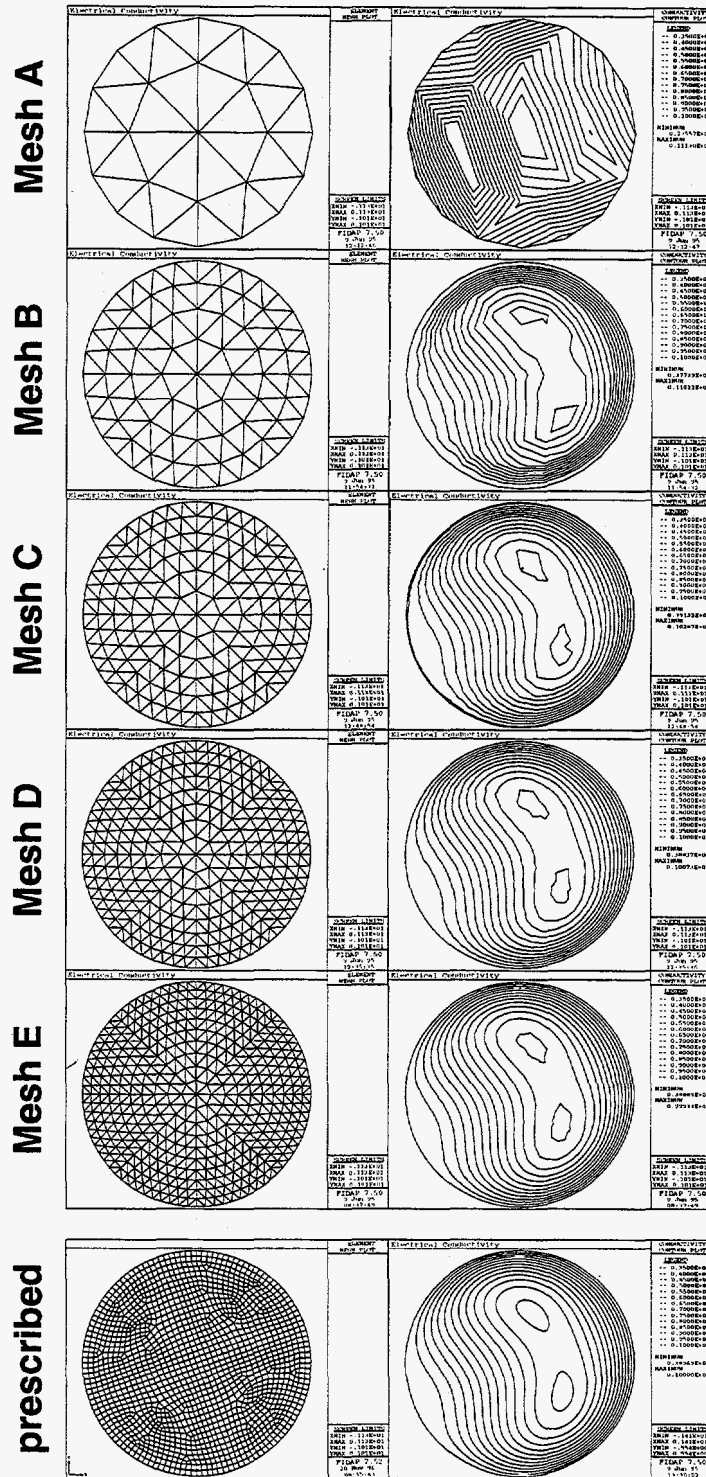
Figure 24. EIT mesh refinement studies. Good convergence is observed.

The third type of validation exercise involved using the codes FEMEIT and 2DynaEIT (Duraiswami et al., 1995; O'Hern et al., 1995a) to reconstruct the size and position of an ICI placed within a circular domain with constant conductivity. In this particular example, the domain was taken to have a radius of $R = 1$, within which the conductivity was prescribed to have the following spatial variation:

$$\sigma = \begin{cases} 0 \ , \ 0 \le r < 0.5 \\ 1 \ , \ 0.5 \le r \le 1 \end{cases} . \tag{52}$$

For both codes, numerical data sets were generated to provide the required input. FIDAP (Fluid Dynamics International, 1995) was used to generate the required voltage data for FEMEIT as previously discussed, and the validation code 2DynaEIT_fwd was used to generate the voltage data for 2DynaEIT. Unfortunately, the FIDAP data set could not be used by 2DynaEIT, which requires smooth boundary data at present, rather than voltages only at electrodes, as would be provided by an experiment. It is anticipated that this limitation will be removed in the future from 2DynaEIT.

Both codes require the type of conductivity variation to be specified. FEMEIT was instructed to use model 5, a "bubble" of arbitrary radius and position with arbitrary conductivity outside the bubble. The width of the bubble boundary was set to $2P_2 = 0.1$, and the ratio of the conductivities inside and outside the bubble was set to $1 - P_1 = 0.02$. 2DynaEIT was instructed to look for a circular "bubble" of arbitrary radius and position, where the bubble here is a zero-thickness boundary separating a region of zero conductivity from a region of unity conductivity. In both cases, the bubble was specified to have an initial radius of 0.2 and an initial position of $(0.7, 0.3)$, and the conductivity was taken to be zero inside the bubble and unity outside the bubble.

Figure 25 shows the results from the FEMEIT and 2DynaEIT reconstructions. The mesh used by FEMEIT is shown and consists of 441 nodes and 800 linear triangle elements. Since 2DynaEIT is a BEM code, only the boundary was meshed. In this exercise, both the domain boundary and the bubble boundary had 16 nodes equidistantly placed. The final positions of the nodes on the bubble are shown in Figure 25. Although the initial guess was quite far from the actual conductivity field, both codes accurately reconstructed the actual field. Interestingly, the times required by the codes to converge were almost the same (a few minutes on a workstation).

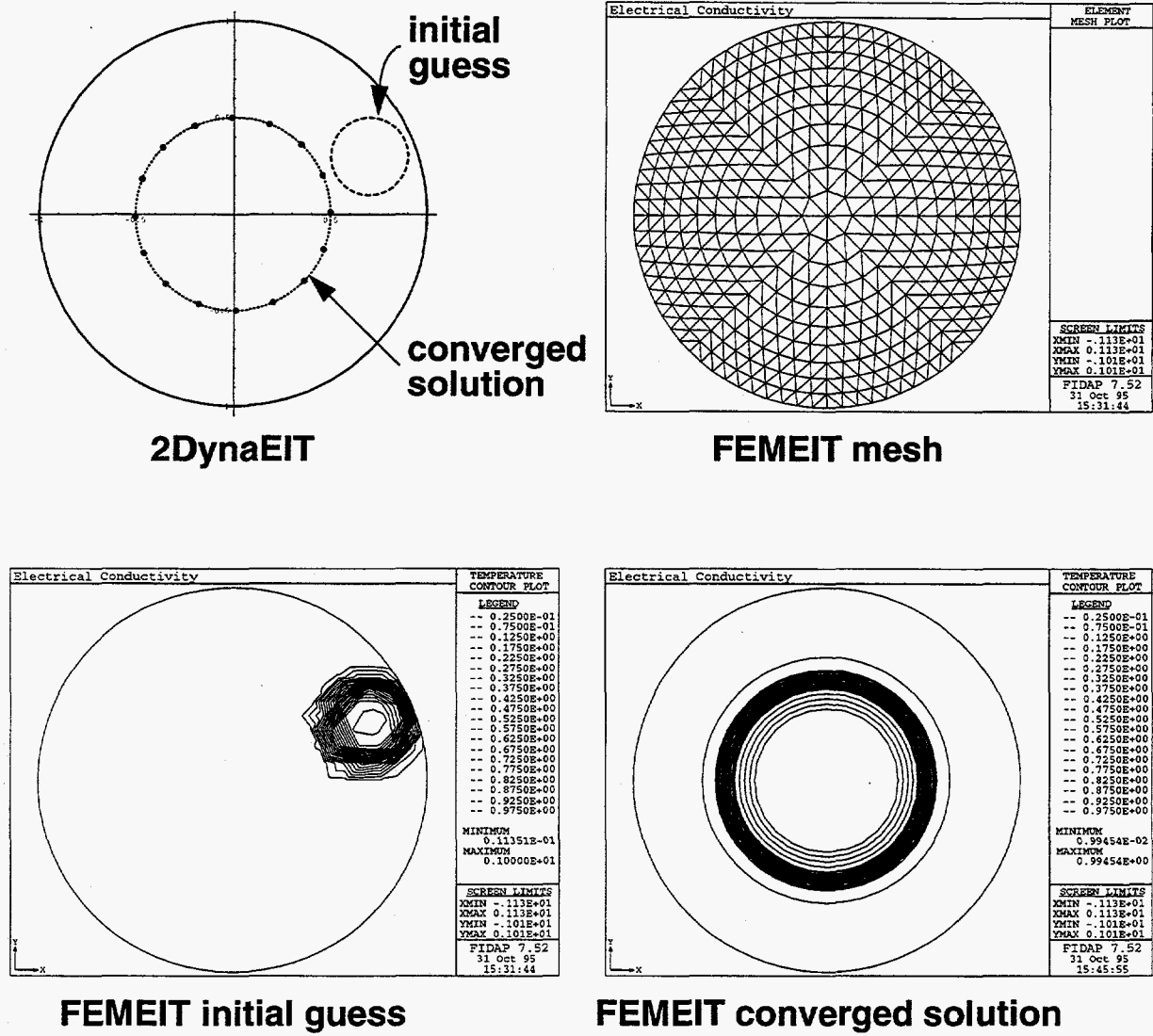# insulating cylindrical inclusion (ICI) reconstructions

2DynaEIT

FEMEIT mesh

FEMEIT initial guess

FEMEIT converged solution

Figure 25. 2DynaEIT (Duraiswami et al., 1995) and FEMEIT ICI reconstructions.

58

2.4.6. EIT Reconstruction Algorithm: Extensions

As presently configured, FEMEIT is capable of utilizing two-dimensional experimentally generated data: electrodes must have small widths and long lengths (infinitesimal strip electrodes) compared to their separations. As previously discussed, the assumption of two-dimensionality is difficult to satisfy in practice. As a first step toward a three-dimensional code with capabilities similar to FEMEIT, another code called EITA3D has been written for infinitesimal point electrodes around an infinite cylindrical domain within which the conductivity field is parametrized according to $\sigma = \sigma_1(r;C_2)/C_1$. With this choice, no additional Jacobian information is required for the parameter C_1, but a Jacobian must still be computed for the parameter C_2. Since the voltages $V_{k,1}^{(m)}$ depend only on the parameter C_2 and the conductivity spatial variation is purely radial, it is practical to compute the voltages once for all (e.g. with FIDAP) for particular choices of the function σ_1 at many values of the parameter C_2. Two types of conductivity fields have been examined thus far:

$$\sigma_1 = \begin{cases} 0 \, , \, 0 \le r/R < C_2 \\ 1 \, , \, C_2 \le r/R \le 1 \end{cases} \text{ with } 0 \le C_2 < 1 \text{ (an ICI or "hole")}, \tag{53}$$

$$\sigma_1 = 1 + C_2[2(r/R)^2 - 1] \text{ with } -1 < C_2 \le 1 \text{ (a parabolic variation)}. \tag{54}$$

For each type of conductivity field, FIDAP was used to compute the $V_{k,1}^{(m)}$ at roughly 20 C_2 values spanning the allowed range. A variant of a standard cubic-spline algorithm (Press et al., 1986) is used to compute both the $V_{k,1}^{(m)}$ and the $\partial V_{k,1}^{(m)}/\partial C_2$ for arbitrary C_2 values within the allowed range. Thus, EITA3D performs no FEM calculations directly but rather uses the voltage values previously computed by FIDAP to determine the updates.

Figure 26 shows the results of applying EITA3D to a data set generated by FIDAP using a conductivity field having the "hole" type of variation with $C_1 = 1$ and $C_2 = 0.1$. Despite being provided with the rather poor initial guesses of $C_1 = 0.5$ and $C_2 = 0.8$, EITA3D is observed to converge smoothly to the correct values after only 9 iterations. Note, however, that this cannot be called a true validation exercise since FIDAP was used to create both the input data set and the FEM data used by EITA3D to determine C_1 and C_2.

As presently configured, 2DynaEIT is not yet capable of utilizing experimentally generated data: current injection is taken to be a smooth function of arc length around the outer boundary rather than at discrete electrodes as in the experiments, exactly one boundary node per electrode is strictly enforced, and the conductivity spatial variation consists of regions of zero conductivity embedded in a constant-conductivity background. All of these issues appear to be resolvable if given sufficient resources.

insulating cylindrical inclusion (ICI) reconstruction
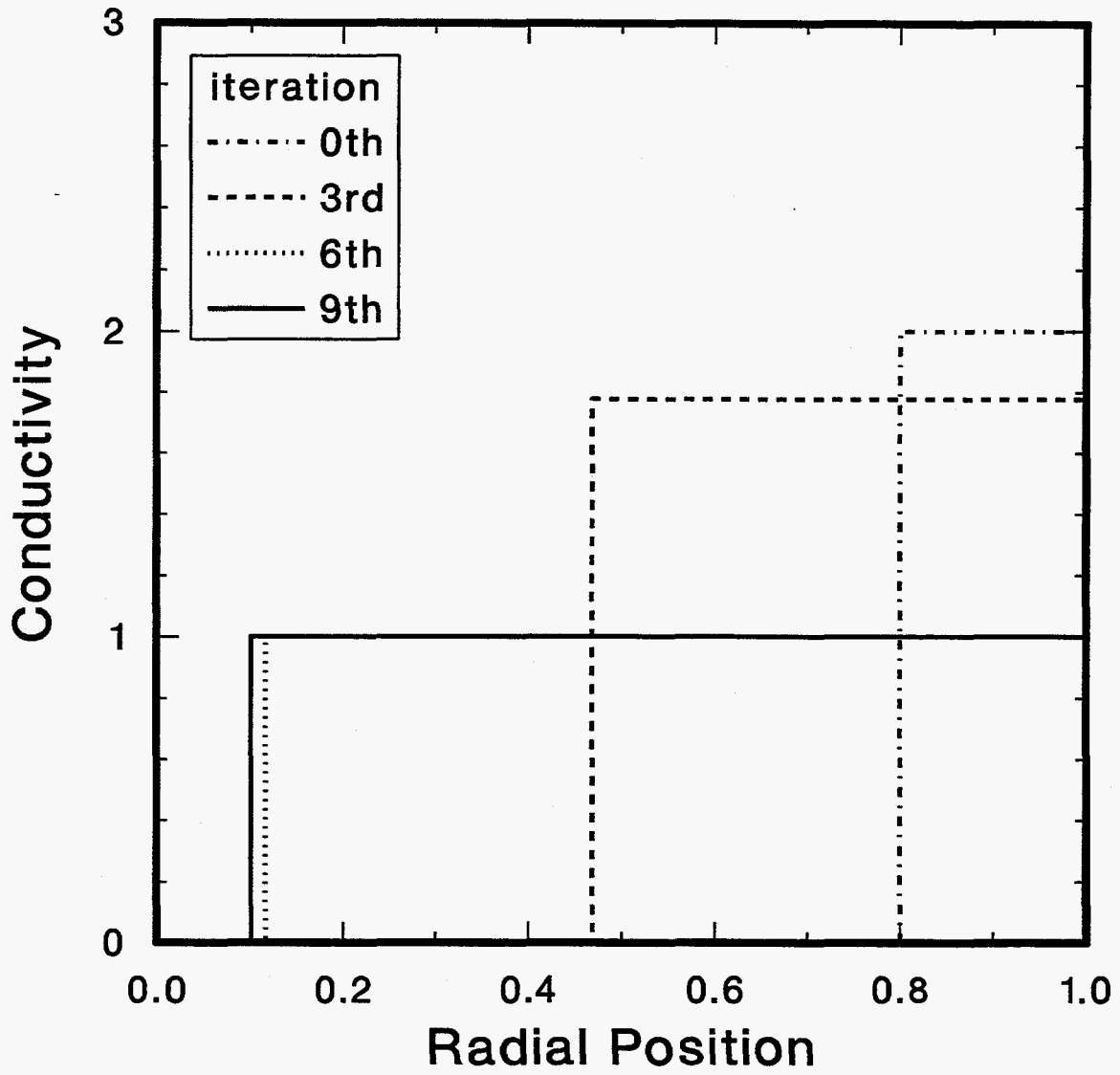
Figure 26. EIT determination of radius of an ICI using point electrodes and EITA3D.

3. Preliminary Validation Efforts

3.1. Wax/Catalyst (WCD) Experiments

As indicated earlier, to develop tomographic diagnostics to measure phase volume fraction spatial distributions in opaque multiphase flows, it is important to quantify the amount of data that is needed by tomographic reconstruction algorithms and how the quality of the reconstruction is affected by the amount of data used in the reconstruction. To this end, a set of wax/catalyst disks (WCDs) were designed and fabricated.

3.1.1. WCD Description

large signature pattern **quadrant calibration pattern**

0.04"

◄──────── 8 inch ────────►   ◄──────── 8 inch ────────►

hole diameters:
1.2, 0.4, 0.4, 0.04 inch;
irregular placement

hole diameters:
1/4, 1/8, 1/16 inch;
2 diameters apart

Figure 27. Wax/catalyst disk (WCD) samples with hole patterns.

Figure 27 shows the two WCDs that were fabricated. The WCDs are 20 cm (8 inches) in diameter and 5 cm (2 inches) thick. Fabrication proceeded by mixing 40% of iron-based catalyst powder by mass into molten Gulftene wax (roughly $C_{40}H_{82}$) until the powder was fairly uniformly distributed in the

wax. The mixture was then poured into molds and allowed to cool. Once solidified, the disks were removed from the molds, which was facilitated by the very slight shrinkage that occurred during cooling and solidification.

Two distinct hole patterns were bored into the disks, as shown in Figure 27. The "large signature" pattern consisted of four holes, three of which were large compared with the expected size of bubbles in the bubble column (typically a f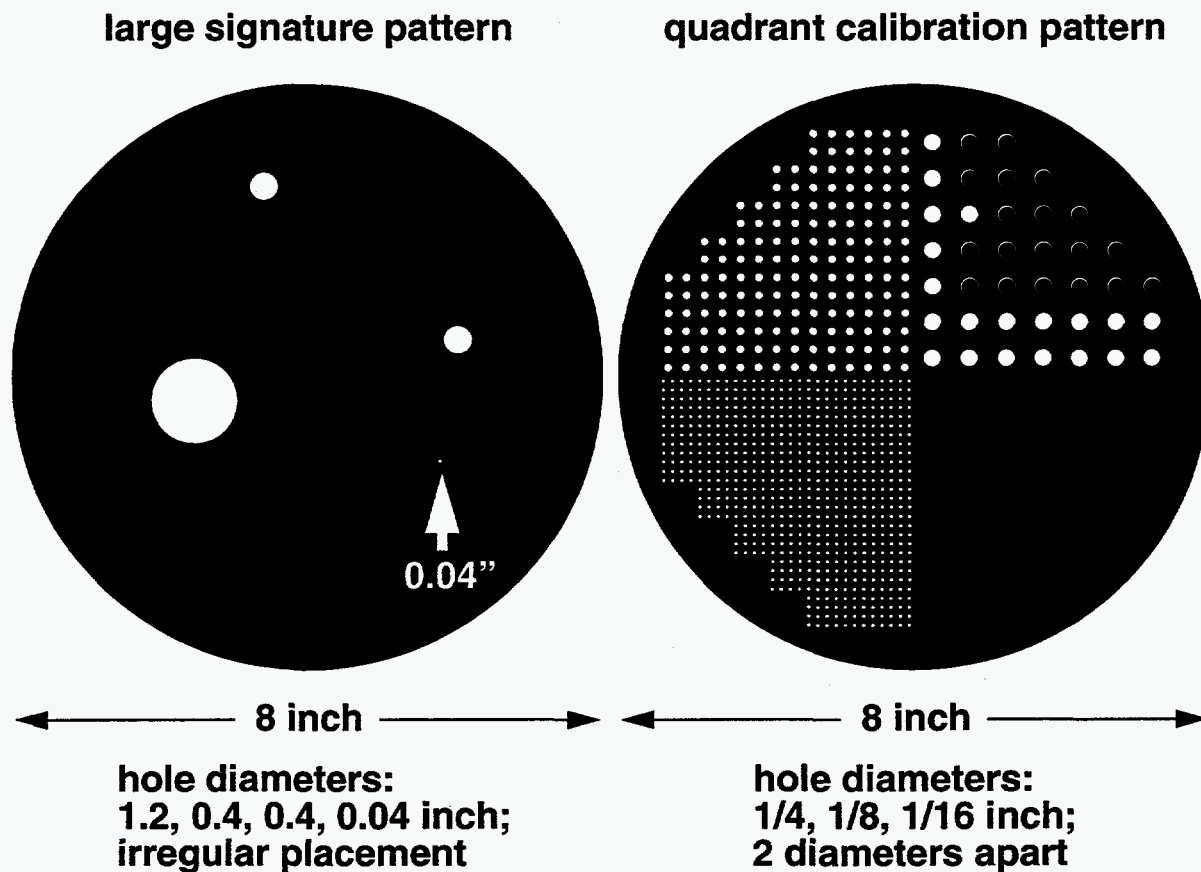ew millimeters). The "quadrant calibration" pattern consisted of one quadrant with no holes and three quadrants with the same average volume fraction occupied by the holes ($\pi/16 \approx 0.2$) with the hole diameters differing by a factor of 2 in adjacent quadrants.

3.1.2. WCD Experimental Results from XRT

To develop a GDT diagnostic technique to measure phase-volume-fraction distributions in multiphase flows, it is important to quantify the amount of data that is needed by tomographic reconstruction algorithms to accurately determine the material spatial distribution. More specifically, it is necessary to determine how the GDT reconstruction is degraded when progressively fewer projections and/or rays per projection are used for the reconstruction. Here, the terms "projection" and "ray" refer to the relative orientations of the object and a detector, respectively, with respect to the tomography system. This effect is important to quantify because one of the goals of this effort is the development of diagnostics capable of application in an industrial setting, in which it is often desirable to minimize the amount of data that must be acquired.

Since GDT and XRT employ the same physical phenomenon (attenuation of MeV-energy photons passing through the material to be examined), the previously discussed XRT facility at Sandia (Thompson and Stoker, 1997) was used to quantify the effect of the quantity of data on the quality of the tomographic reconstruction of the material distribution. Of particular interest was the minimum number of rays required to produce a reasonable reconstruction, where a single ray represents a measurement by a particular virtual detector for a particular translational position and a particular rotational position of the material to be examined. As previously indicated, since the multiphase flows ultimately to be examined by GDT are highly unsteady and spatially variable at the microscale, only macroscale information is sought (i.e. averages over a region of space that is small compared to the vessel but large compared to bubble or particle sizes). Thus, data requirements are expected to be substantially less restrictive in this application than for detailed XRT imaging of solid parts.

Three XRT data sets were obtained using the WCDs discussed in the previous section. These data sets were acquired using the following WCD configurations: the large-signature disk, the quadrant-calibration disk, and the quadrant-calibration disk surrounded with a 1.59 cm (5/8 inch) thick steel jacket fabricated by wrapping about 400 layers of 38 μm (0.0015 inch) thick sheet steel around its circumference. The purpose of the latter test was to examine the impact of a thick-walled steel vessel on the reconstruction of the material distribution within since most multiphase flows of industrial interest are contained within thick-walled vessels. Each XRT data set consisted of 360 projections of 620 rays per projection (approximately a quarter of a million data points) for a planar slice through the middle of the disk. To examine the effect of the number of rays on the quality of the tomographic reconstruction, additional data sets were created from the initial data set by systematically discarding certain rays. For the large-signature disk, entire projections were discarded: for example, every other projection was discarded to create the 180-projection data set from the original 360-projection data set. For the quadrant-calibration disk both without and with the steel jacket, 42 reduced data sets were generated from all possible combinations of 9, 18, 36, 45, 90, 180, and 360 projections with 31, 62, 124, 155, 310, and 620 rays per projection. Note that the data set (360,620), which denotes 360 projections and 620 rays per projection, is the full data set (223,200 data points)

and that the data set (9,31) is the most sparse data set (only 279 data points), so these data sets span roughly 3 orders of magnitude in amount of data.

18 projections   **36 projections**   **90 projections**

180 projections   **360 projections**   **360 projections (enlarged)**
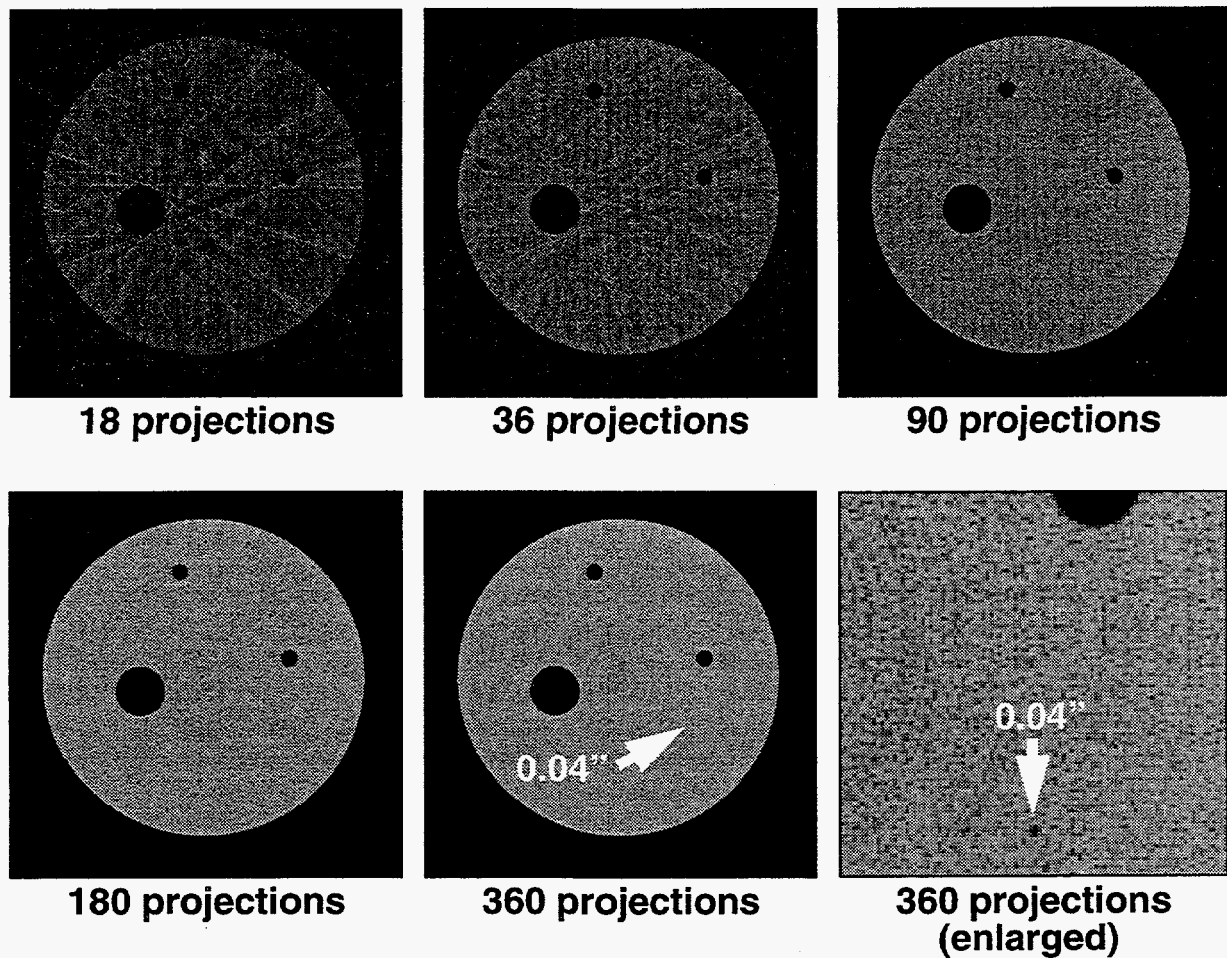
All cases have 620 rays per projection.

Figure 28. XRT resolution study for "large-signature" WCD.

Figure 28 shows the XRT reconstructions achieved for the large-signature WCD. Several observations can be made about these reconstructions. First, in all cases, the tomographic reconstructions are excellent. The three larger holes are accurately reproduced even with only 18 projections (i.e a factor of 20 less data than with 360 projections). However, the smallest hole is only marginally discernible for the cases with 18, 36, and 90 projections. Second, the errors produced by low resolution are streaks in the images, rather than smeared-out regions, and these streaks are always tangent to the edges of holes or the sample perimeter. Third, the amount of data used with 18 projections (11,160 points) is still rather large.
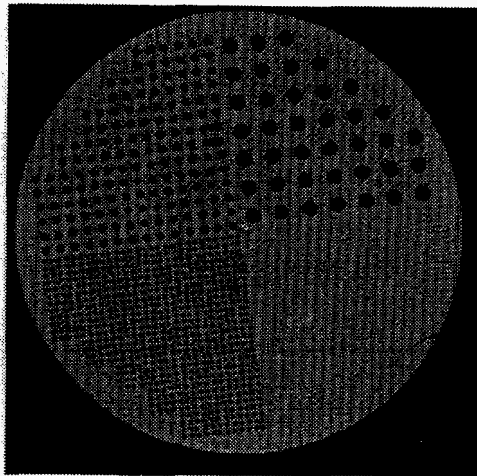
(620,360): 360 projections, 620 rays per projection   **(36,31): 36 projections, 31 rays per projections**
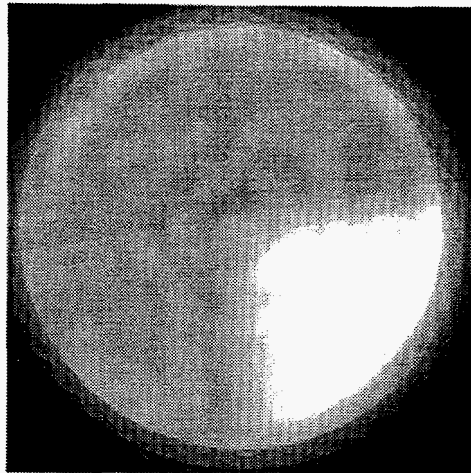
Figure 29. XRT resolution study for "quadrant calibration" WCD.

Figure 29 shows 2 of the 42 XRT reconstructions achieved for the quadrant-calibration WCD in the absence of the steel jacket. Several observations can be made about these reconstructions. First, as was true for the previous XRT experiments, the high-resolution reconstructions are excellent. The smallest diameter holes are individually visible, as are imperfections in the sample itself such as cracks near the edge and two misdrilled 1/8-inch holes. Second, the type of degradation observed in the reconstruction depends strongly on which data are discarded. Keeping the number of projections constant while reducing the number of rays per projection has the effect of gradually averaging out the data smoothly. As the number of rays per projection is decreased, the smallest holes first blur together to produce a relatively uniform background that is noticeably different from the undrilled region. Further reductions in the number of rays per projection blur out the medium holes and ultimately the large holes. Thus, reducing the number of rays per projection while fixing the number of projections acts like a spatial filter and averages out small-scale features. Keeping the number of rays per projection constant while reducing the number of projections has a rather different effect: the reconstructions become progressively more "streaky" where the streaks have the appearance of "shadows" of the holes. This was noted previously for the large-signature WCD.

Exactly the same type of XRT data set as the above was taken for the quadrant-calibration WCD with the steel jacket in place, and reduced data sets were produced in the identical manner. As was true for the previous XRT experiments, the high-resolution reconstructions were excellent. Although the steel casing clearly had a very strong signature, even the smallest diameter holes were individually visible, as were imperfections in the sample itself that were previously noted. The types of image degradation caused by reducing the number of projections or the number of rays per projection were observed to be identical to those observed in the absence of the steel jacket.

For slurry-phase bubble-column reactors, the void-fraction distribution is composed primarily of large numbers of rather small bubbles, the number density of which probably varies in a relatively smooth fashion from location to location. Thus, rather than trying to resolve very large numbers of individual bubbles, it is preferable to measure the void fraction averaged over small volumes of fluid that are

large compared to individual bubbles and inter-bubble separations but small compared to the size of the reactor and the length scale over which the bubble size distribution and number density vary appreciably. The XRT reconstructions are seen to accomplish this for the WCDs when sufficiently few rays per projection are employed so long as enough projections are used. For example, the reconstruction based on data set (36,31) is very good when judged by the standard of determining the macroscale material distribution in the sense of averaging over small volumes rather than resolving individual holes: all three drilled quadrants are clearly seen to have the same value for the average solid volume fraction, which is significantly different from the undrilled quadrant. However, using few projections with many rays does not accomplish this. Data set (9,124) possesses the same number of data points (1116) as data set (36,31), but its reconstruction (not shown but similar to those for the large-signature WCD) is much poorer in the above sense. Interestingly, the reconstruction from a "streaky" data set such as (9,124) contains information that could be used to extract hole diameters and spacings, perhaps via FFT or other standard image-processing techniques, so long as the data set was time-resolved, rather than time-averaged. This has not been investigated.

To reiterate, quite accurate XRT reconstructions of macroscopic material distribution have been produced using data sets with as few as 36 31-ray projections (1116 data points). Reconstructions based on data sets with the same number of data points but fewer projections with more rays are not as satisfactory. Thus, if restricted in the amount of data, it appears to be better to bias data collection in favor of more projections with fewer rays per projection. These observations also have ramifications for axisymmetric systems. If the field to be reconstructed is axisymmetric, only one projection is required (no new information is provided by additional projections). As a result, accurate reconstructions of fairly arbitrary axisymmetric fields can be achieved with as few as 31 rays (and possibly fewer if the field is sufficiently smooth). Thus, GDT data at roughly 30 horizontal positions is required to produce a reasonable reconstruction of the material distribution in a roughly axisymmetric system like a bubble column.

3.2. Boxed Bubble Column (BBC) Experiment

As previously discussed, the GDT system implemented herein produces inherently time-averaged data because of the long times required to collect data. However, most multiphase flows, particularly flow in a bubble column, are not steady at the microscale, and many are not steady at the macroscale for conditions of interest. Thus, some questions remain about the ability of the GDT system to produce accurate information. More specifically, if temporal variations of material distribution are large, then the use of an average intensity to determine an average attenuation coefficient will produce considerable error. This question could in principle be addressed by collecting counts for many short periods along each ray or path, determining the path-averaged attenuation for each of these periods, and temporally averaging the path-averaged attenuation (not the intensity as is currently done) prior to performing the tomographic reconstruction. Unfortunately, this is difficult to do in practice due to the large thicknesses of material to be penetrated. For example, in a bubble column, the time to collect even a few hundred counts can be comparable to hydrodynamic time scales (perhaps up to several seconds). As a result, RTR was investigated as a possible way to acquire information about temporal variations of material distribution in bubble-column flows. Of particular interest was to ascertain whether RTR could be successfully applied to observe temporal variations in the material distribution in bubble-column flows and if so to determine whether these temporal variations are large enough to invalidate using the temporally averaged intensity to calculate the temporally averaged attenuation.
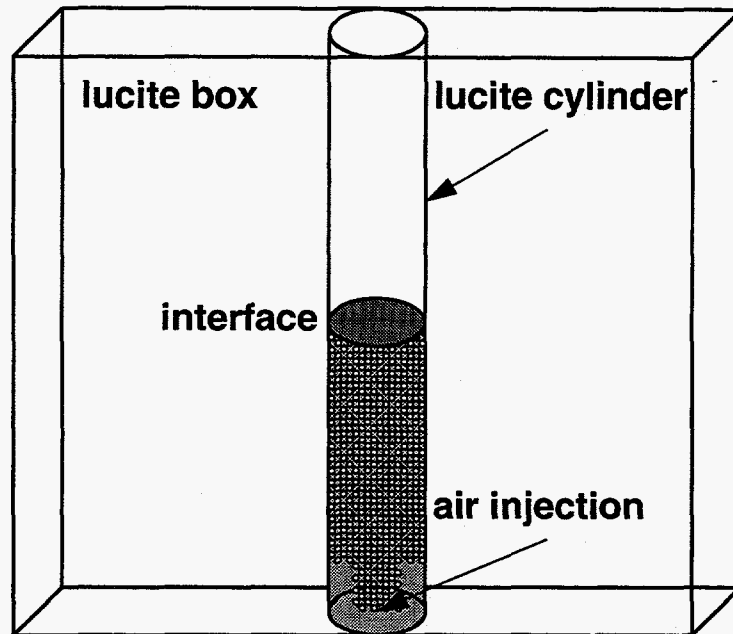
3.2.1. BBC Experimental Setup

Figure 30. Boxed bubble-column experiment.

Figure 30 shows a schematic diagram of the boxed bubble-column (BBC) experiment. The column itself consisted of a lucite cylinder with an inner diameter of 10.16 cm (4 inches), a wall thickness of 0.635 cm (0.25 inches), and a height of 91.44 cm (36 inches). This cylinder was placed within a lucite box having a height equal to that of the cylinder, an inner width of 12.70 cm (5 inches), a lateral width of 43.18 cm (17 inches), and a wall thickness of 1.27 cm (0.5 inches). The purpose of the box was to allow the column to be surrounded with water to produce a region of comparable attenuation at all lateral positions relative to the cylinder axis as was thought to be necessary to produce adequate contrast. However, as it turned out, images recorded with the box filled with water did not seem to be of better contrast than those recorded with the box empty, and the latter were more visually instructive.

The BBC was typically operated as follows. The column was filled with water to a height of 60.96 cm (24 inches), and air was injected from a single tubular nozzle with inner and outer diameters of 0.79 mm and 1.57 mm centered at the bottom of the column. Air flow was produced by a small compressor attached to the orifice by a length of tubing. Adjusting the compressor pressure controlled the air flow rate, with higher pressures corresponding to higher flow rates. Unfortunately, it was not possible to quantify the relationship between the compressor pressure and the resulting volumetric flow rate of the air that resulted.
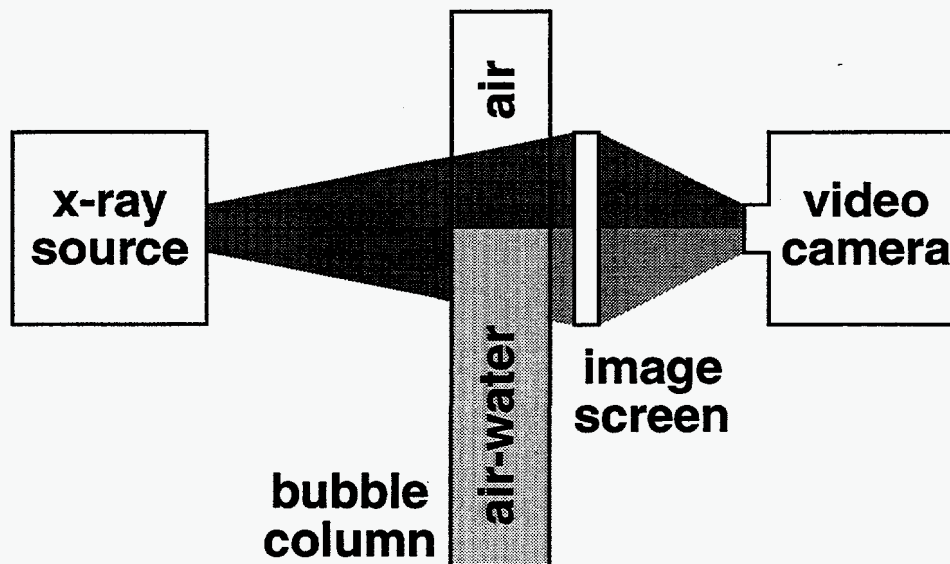
3.2.2. BBC Experimental Results from RTR

Figure 31. Schematic diagram of RTR applied to BBC experiment.

Figure 31 shows a schematic diagram of the previously described RTR system applied to the BBC experiment. The BBC was filled with water to a height of 60.96 cm (24 inches) prior to the tests and was positioned such that the undisturbed air-water interface lay just below the center of the field of view for the XRT system. Air flow was initiated and held constant while video recording were made at the standard video frame rate for a long period of time. The video results were analyzed following the tests using image-processing software. Tests were performed for several air flow rates and for the box filled with water and empty.

Figure 32 shows images recorded with the box empty for three sets of air flow rates: no air flow; slow air flow, and fast air flow. These images were produced by averaging large numbers of images for each air flow rate. Several features are apparent from these images. The time-averaged interface is observed to thicken with increasing air flow rate (the undisturbed interface position is indicated in each image). This corresponds to the visual observation that the gas-liquid interface becomes more agitated with increasing air flow rate. Also, interface midpoint is seen to be higher and the attenuation in the region below the interface is seen to decrease with increasing air flow, as would be expected since the amount of gas present in the multiphase mixture increases with the air flow rate. From comparing a few individual frames to the average images, temporal variations did not appear to be large except in the vicinity of the gas-liquid interface. However, extensive analysis of many more frames using the available image-processing software is required to confirm and quantify this conclusion. The attenuations observed with this small-diameter bubble column suggest that application of this RTR system to large-diameter bubble-column vessels with steel walls is unlikely to produce satisfactory results.
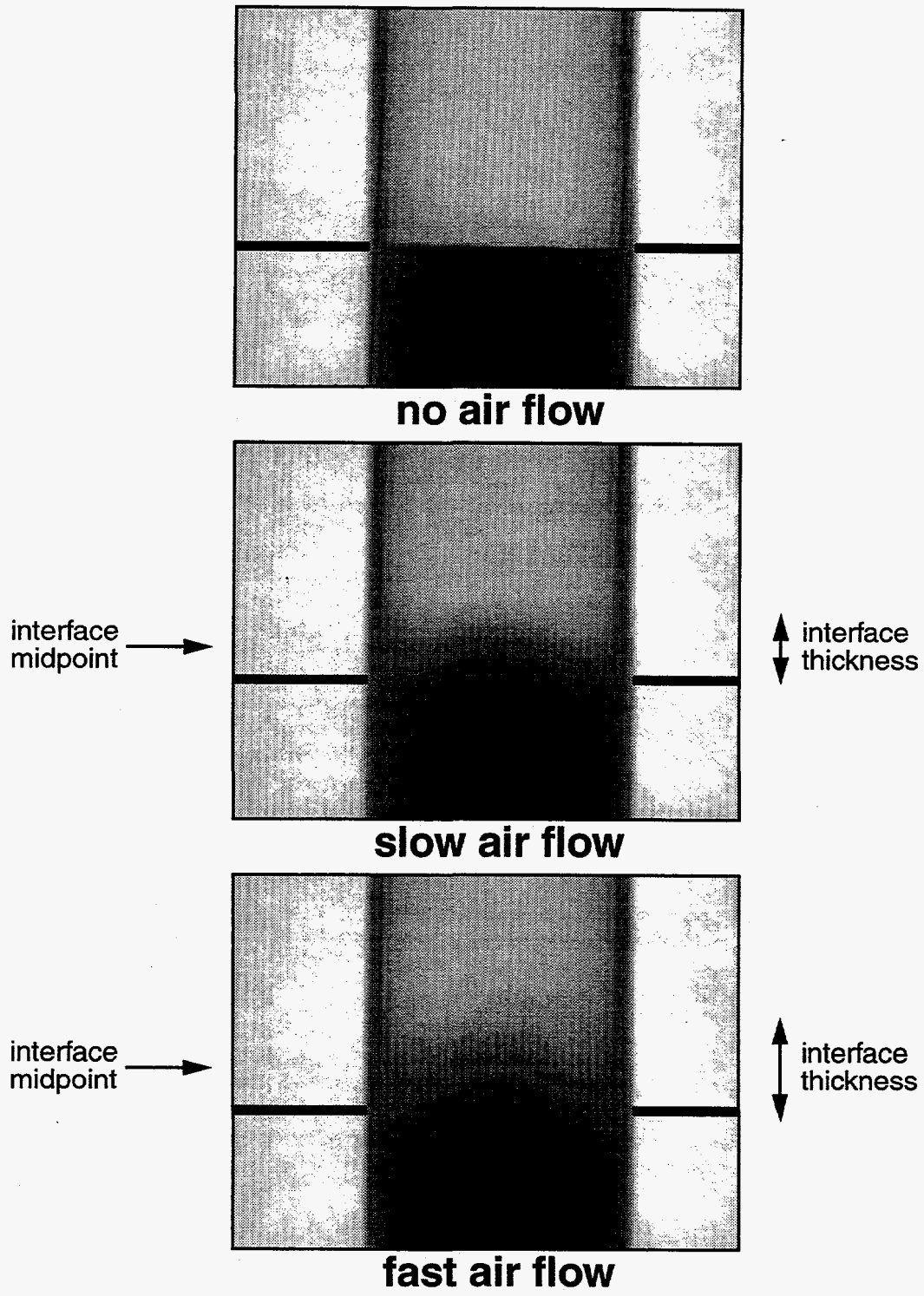
no air flow

slow air flow

interface
midpoint →

← interface
thickness

fast air flow

interface
midpoint →

← interface
thickness

Figure 32. RTR results for BBC experiment.

3.3. Insulating Cylindrical Inclusion (ICI) Experiments

As previously discussed, computational validation exercises were performed to assess the capability of the computer code FEMEIT to produce accurate reconstructions of a spatially varying conductivity field. FEMEIT has also been validated by comparison to experiments employing known and well controlled conductivity fields.

A nontrivial spatially varying conductivity field was produced by inserting an insulating cylindrical inclusion (ICI) into a homogeneous conducting liquid, as shown in Figure 33. More specifically, insulating tubes of known diameters were placed within the EIT probe ring employing strip electrodes, and the EIT system was used to measure the electrode voltages during current flow. These electrode voltages were then used as inputs to the code FEMEIT to determine the diameter and position of the ICI. A limited number of experiments were also performed using the EIT probe ring with point electrodes. These data sets were analyzed using the code EITA3D, as appropriate for point, rather than strip, electrodes.

3.3.1. ICI Experimental Setup
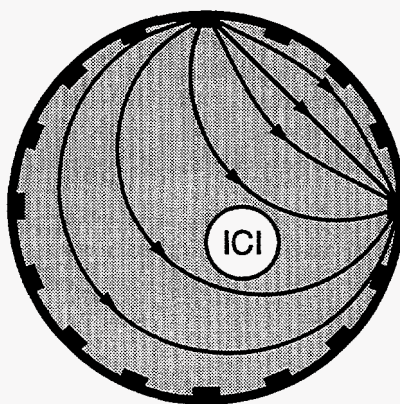
top view

Figure 33. Schematic diagram of EIT with an insulating cylindrical inclusion (ICI).

The EIT probe ring employing 16 strip electrodes was used for the FEMEIT validation experiments. To create a two-dimensional field, the probe ring was capped off on the bottom with a lucite plate mounted flush to the bottom of the electrodes, a PVC cylinder of known diameter (the ICI) was placed eccentrically at a particular position within the probe ring, and the probe ring was filled with water to the top of the electrodes.

The EIT probe ring employing 16 point electrodes was used for the EITA3D validation experiments. The probe ring, 2 diameters in height, was capped at the bottom, a lucite cylinder of known diameter (the ICI) was placed concentrically within the probe ring, and the probe ring was filled with water to the top.

The same electronics hardware was used for both probe rings. A small amount of salt was added to the water as needed to bring the liquid conductivity to roughly 1 mS/cm. The internal capacitance and resistance of the electronics were adjusted to yield minimal signal-to-noise ratio for these conditions.

3.3.2. ICI Experimental Results from EIT

For the FEMEIT validation experiments, a 6.92 cm (2.725 inch) hollow PVC tube was used as the ICI. Two different positions of the ICI were examined, one eccentric and one concentric with respect to the probe ring. For each position, all EIT voltages were measured 6400 times each, which required roughly 10 minutes. The averages of these measurements were the inputs to FEMEIT. To reconstruct the size and position of the ICI, FEMEIT used a conductivity function of the form:

$$\sigma = C_1 \left\{ 1 + \frac{P_1}{2} \left[\tanh\left(\frac{r - C_2}{P_2}\right) - \tanh\left(\frac{r + C_2}{P_2}\right) \right] \right\}, \tag{55}$$

where $r^2 = (x - C_3)^2 + (y - C_4)^2$, $\{C_1, C_2, C_3, C_4\}$ are adjustable conductivity parameters, and $\{P_1, P_2\}$ are nonadjustable parameters. This function represents a circular region of radius C_2 centered at (C_3, C_4) with a boundary thickness proportional to $2P_2$, well inside of which the conductivity is approximately $C_1(1 - P_1)$ and well outside of which the conductivity is approximately C_1. If P_1 is chosen close to but smaller than unity and P_2 is taken to be small compared with C_2, this function represents an insulating cylinder, where its position, radius, and external conductivity are free to vary. FEMEIT calculations were performed using mesh E (the most highly refined mesh from the numerical validation exercises, see Figure 24) and the above function with the nonadjustable parameters assigned values of $1 - P_1 = 0.02$ and $2P_2 = 0.1$, where the lucite cylinder has been normalized to unity radius. The sizes and positions of the ICI reconstructions are shown in Figure 34 and agree well with the experimental sizes and positions, also shown in Figure 34. No dependence on the initial values of the adjustable parameters was seen in the reconstructions: the calculations consistently yield values of 6.91 cm (2.72 inch) for the ICI diameter.

For the EITA3D validation experiments, long hollow lucite tubes were used as the ICIs. Two different concentrically-positioned ICIs and two cases without ICIs were examined, as shown in Table 2. For each ICI, all EIT voltages were measured 6400 times each, and the averages of these measurements were the inputs to EITA3D. To reconstruct the size of the ICI, EITA3D used a conductivity function (based on FIDAP voltages) of the form:

$$\sigma = \sigma_1 / C_1, \quad \sigma_1 = \begin{cases} 0, & 0 \le r/R < C_2 \\ 1, & C_2 \le r/R \le 1 \end{cases} \quad \text{with } 0 \le C_2 < 1. \tag{56}$$

The agreement between the experimental and computational sizes is fairly good although EITA3D consistently overpredicts the ICI diameter (in fact, small-diameter objects can be predicted when none are present, as shown in Table 2). The cause of this overprediction is not known at present.

Table 2. EITA3D reconstructions of ICI diameters.

Experimental diameter	Reconstructed diameter
0 cm (0 inch)	1.04 cm (0.41 inch)
0 cm (0 inch)	1.55 cm (0.61 inch)
5.72 cm (2.25 inch)	5.99 cm (2.36 inch)
10.19 cm (4.01 inch)	10.52 cm (4.14 inch)

actual
position
and size
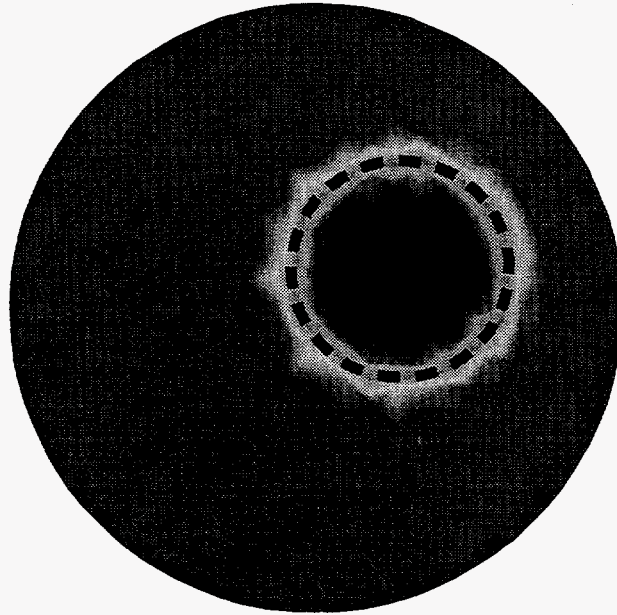
eccentric placement

actual
position
and size

concentric placement

Figure 34. EIT reconstructions of insulating cylinders using strip electrodes.

4. Experimental Testbeds and Results

4.1. Transparent Bubble Column (TBC) Experiment

A transparent bubble column (TBC) experiment was used as a test bed for diagnostics development and is shown in Figure 35. Although not capable of operation at the high pressures and temperatures of industrial interest, this bubble column facilitated simultaneous implementation and rapid modification of multiple types of diagnostic techniques. Optical techniques, such as flow visualization and LR, can be applied because of the transparent nature of the TBC experiment. Pressure-based techniques, such as DP, can be used if pressure taps penetrate the side wall. Radiation-based techniques, such as GDT, are facilitated by virtue of the side wall, which was fairly thin and made of low-density material because of the absence of imposed pressurization or heating. Electrical techniques, such as BEI, EIT, and the EBP, can be applied without concern about the effects of current-transport through the side wall since it is insulating. Geometric modifications, such as installation of alternate spargers or probe rings, could also be carried out easily and quickly.
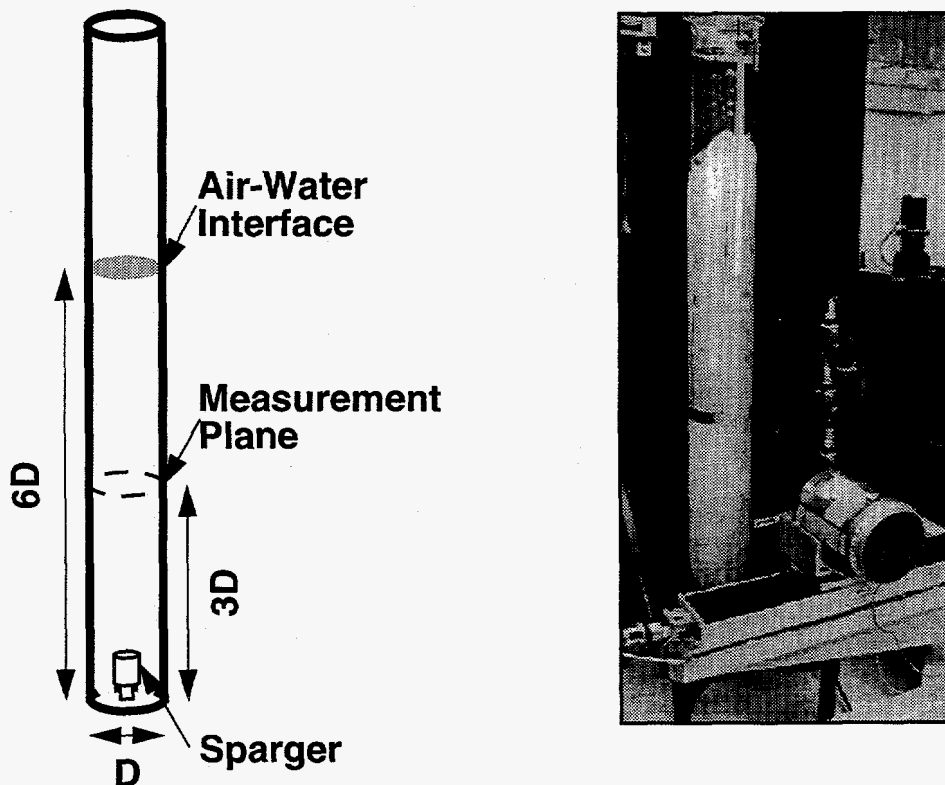

Figure 35. The transparent bubble-column (TBC) experiment.

72

4.1.1. TBC Experimental Setup

The TBC experiment is a lucite tube held in place by a unistrut frame (see Figure 35). The lucite tube has outer and inner diameters of 20.32 cm (8 inch) and 19.05 cm (7.5 inch), respectively, a wall thickness of 0.635 cm (0.25 inch), and a height of 1.83 m (72 inch). The working fluids generally are air and water although some other liquids can be used, and operation is at ambient temperature and pressure. To preclude overflow during air flow, the column is filled with water to an initial height of only 1.14 m (45 inch), a height-to-diameter ratio of 6. Gas is introduced near the bottom of the column via a sparger. Two spargers have been employed to date. The original sparger used in the TBC experiment was a 9 cm diameter ring spiral made from 0.635 cm (0.25 inch) OD copper tubing in which 12 downward-facing holes of 0.08 inch diameter were drilled at equal azimuthal intervals. Another sparger was subsequently developed and installed in the TBC experiment, as shown in Figure 36. This sparger is a hollow toroidal ring with a 10.16 cm (4 inch) center-line diameter and is made from stainless steel tubing with a 0.95 cm (0.375 inch) diameter and a 0.165 cm (0.065 inch) wall through which 10 downward-facing holes of 0.159 cm (0.0625 inch) diameter have been drilled at equal azimuthal separations. As currently configured, air flow rates of up to 600 lpm (liters per minute) are routinely achievable, which correspond to gas superficial velocities up to 35 cm/s. It is also possible to introduce a significant amount of a third phase of solid particulates into the column, such as sand or glass spheres.
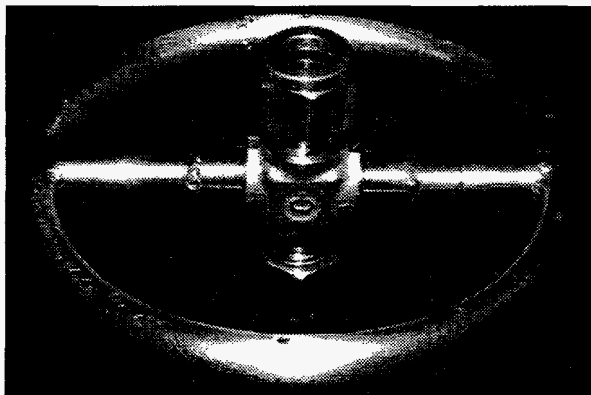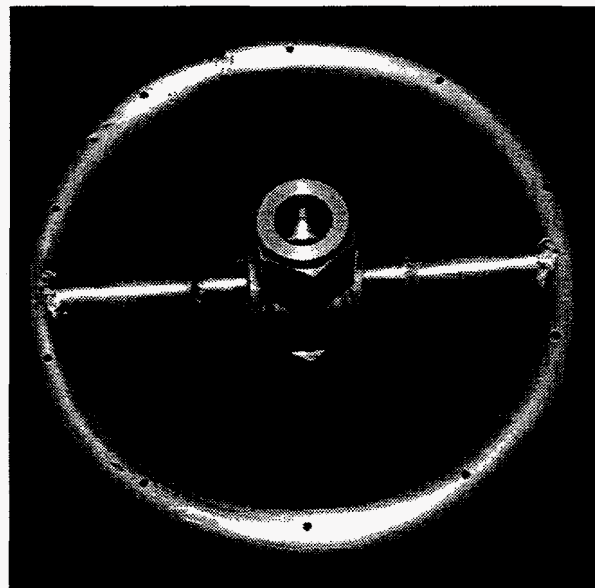
side view   **top view**

Figure 36. Sparger (final design) in TBC.

The LR and DP diagnostics are applied routinely to the TBC experiment. For the LR technique, the gas-liquid interface can be observed visually and compared with ruled markings on the column for quantitative values. If necessary, a video camera and a VCR can be used to record this information for post-test analysis or image-processing. For the DP technique, five pressure transducers have been installed to measure the pressure within the column. These transducers are located at vertical intervals equal to the inner diameter and resolve axial (and temporal) variations in the pressure.

Additional diagnostics can be installed as needed for development, validation, and data collection. GDT can be applied directly with no modification to the TBC experiment simply by positioning the traverse appropriately so that the arms surround the lucite column. Applying BEI or EIT requires installation of the corresponding probe ring within the column. This was facilitated by sectioning the column into two halves and fabricating short connecting sections that seal to the column and probe-ring exteriors using O-rings. The EBP was deployed by installing a special lucite section into the column, which contains a tap through which the EBP support is inserted.

Applying electrical techniques imposed two additional constraints on the TBC experiment. First, the presence of a grounded conductor anywhere in the liquid-filled portion of the column was found to exert a strong effect on electrical data. To prevent this from occurring, all conducting fittings were removed or electrically isolated, including the sparger. Second, it was discovered that the evaporation produced by dry air flowing through the water can cool it by as much as 2-4 K over an hour of operation. Since the electrical conductivity of water is temperature-dependent and decreases with decreasing temperature, the cooler water appears more insulating to electrical techniques. If this effect is ignored, the cooled water causes electrical techniques to register the presence of air even when no air was present, as shown in Figure 37. To compensate for evaporative cooling, three controllable 80-W immersion heaters were installed in the column and are used to maintain the water temperature at a prescribed value to 0.1 K.
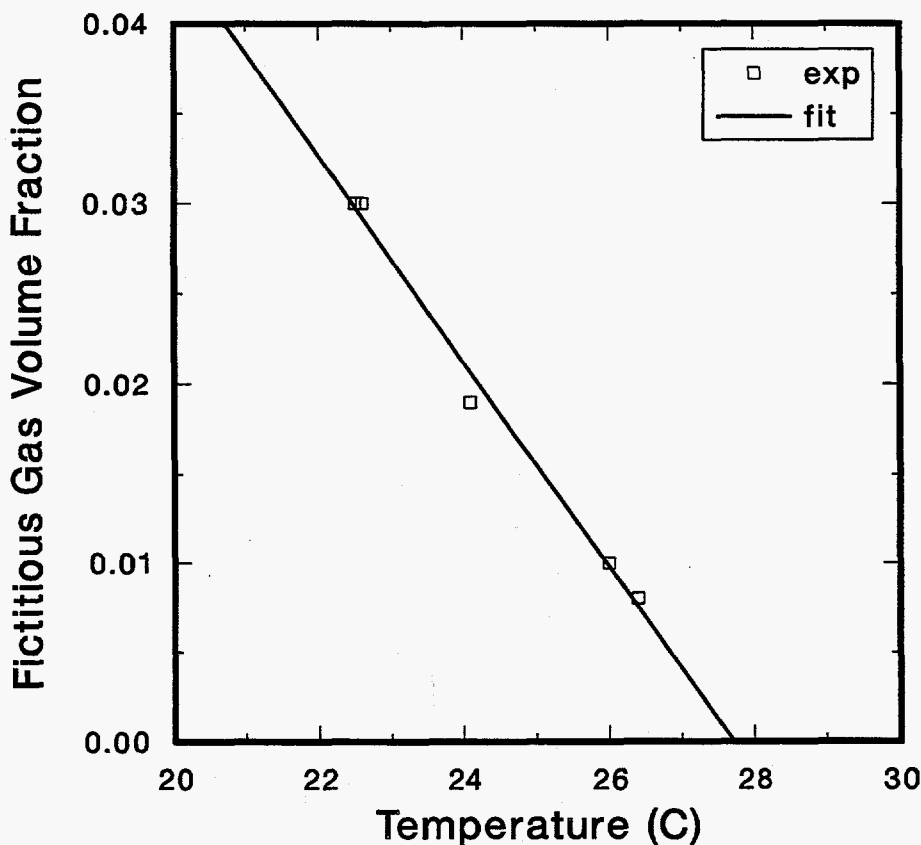

Figure 37. Temperature-dependent electrical conductivity can give spurious results.

4.1.2. TBC Experimental Results

Gas-liquid two-phase flow experiments and gas-liquid-solid three-phase flow experiments have been performed in the TBC experiment (Torczynski et al., 1996a). Air and water were the working fluids, and sand (silicon dioxide particles with diameters in the 0.1-0.4 mm range) was used for the solid particulate phase in the three-phase experiments. The original spiral-ring sparger was used for these experiments, and the column was filled with the prescribed amount of sand (none for the two-phase experiments) and with sufficient water so that the interface was 6 diameters above the bottom of the column in the absence of air flow.

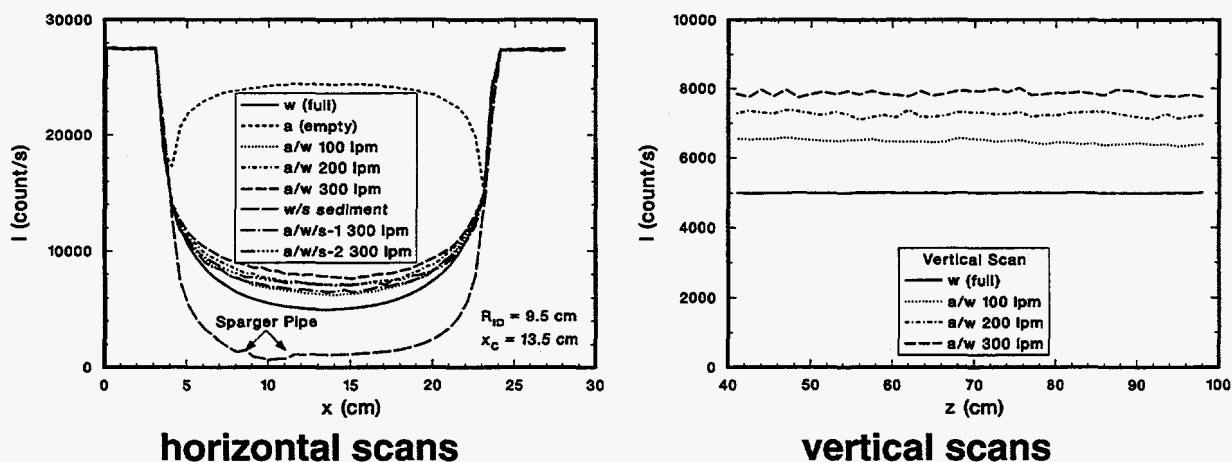**horizontal scans**   **vertical scans**

Figure 38. Count-rate results from GDT in TBC.

GDT scans were performed at various locations for several flow conditions in the TBC experiment. Count-rate results for all of these scans are shown in Figure 38, in which "a", "w", and "s" denote air, water, and sand, respectively. Horizontal GDT scans with the column centered at $x = 13.5$ cm were performed at two vertical locations: 3 diameters above the bottom of the column for all flow conditions and in the sediment layer that exists near the bottom of the column prior to initiating air flow for three-phase experiments. For all horizontal scans, attenuation measurements were made at 0.5 cm intervals across the width of the column. This yielded 38 horizontal positions, which previously were shown to be sufficient to produce an accurate reconstruction of the material distribution for axisymmetric conditions. Horizontal GDT scans were performed with the column empty of water (full of air) and full of water (empty of air) for calibration purposes, with gas-liquid flow at air flow rates of 100, 200, and 300 lpm, and with gas-liquid-solid flow at an air flow rate of 300 lpm, where an air flow rate of 300 lpm corresponds to a gas superficial velocity of 17.7 cm/s. Vertical GDT scans were also performed for the gas-liquid flow conditions above, where attenuation measurements were made directly through the diameter at 1.5 cm intervals in the vertical direction from 40 cm to 100 cm above the bottom of the column. The purpose of the vertical scans was to verify that the material distribution did not change significantly in the vertical direction, which is indeed seen to be the case from Figure 38.

For comparison purposes, two other methods were used to yield information about the gas volume fraction. First, LR measurements were performed to determine the average gas volume fraction for the entire column. Second, DP measurements were performed to determine the average gas volume fraction in a one-diameter length of the column centered about the GDT measurement plane.
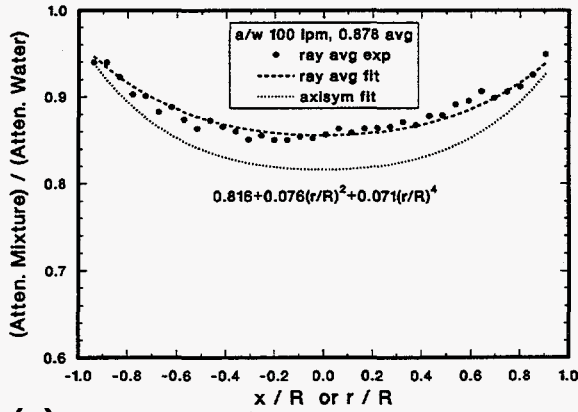
Figure 39 shows the GDT results for the gas-liquid and gas-liquid-solid flows described above in the TBC experiment. Four of the plots (a-d) in Figure 39 show the variation of the normalized mixture attenuation as a function of horizontal or radial position for the flow conditions that were examined. The symbols indicate the experimentally measured normalized attenuation coefficient averaged along the paths (rays), essentially the values $\{(x_i, \psi_i)\}$ required by the GDT reconstruction algorithm. The dashed curves are polynomial fits to these values using quartic polynomials of the form $b_0 + b_1(x/R)^2 + b_2(x/R)^4$. Quartic polynomials were chosen because polynomials of lower degree produced much less satisfactory fits and polynomials of higher degree did not produce significantly better fits. The dotted curves are the resulting polynomial reconstructions of the radial variation of the attenuation coefficient and as such have the form $a_0 + a_1(r/R)^2 + a_2(r/R)^4$.

For two-phase flow, knowledge of the normalized mixture attenuation coefficient is sufficient to permit determination of the phase volume fractions of the two phases. The gas-volume-fraction radial profiles for the two-phase conditions are shown in the fifth plot (e) for the air flow rates examined. As is typical of gas-liquid flows in bubble columns, the gas volume fraction is largest on axis, monotonically decreases toward the side wall, and increases with increasing gas flow rate. For this particular experiment, the gas-volume-fraction radial profiles are also observed to become more blunt with increasing gas flow rate. This observation is probably not true in general, however. Table 3 shows a comparison between the average gas volume fractions determined from the LR, DP, and GDT techniques. The agreement is reasonably good, particularly since each technique averages over a different volume of the column (the entire column for LR, a cylinder that is one diameter high for DP, and a thin cross-sectional slice for GDT). Also, the GDT measurements indicate a modest but systematic departure from axisymmetry, so it is not altogether surprising that gas-volume-fraction values determined by applying an axisymmetric GDT reconstruction algorithm should depart slightly but systematically from values determined by other techniques not assuming axisymmetry. Unfortunately, it is not possible to determine the precise amount of departure from axisymmetry without multiple projections (i.e. scans from different azimuthal angles). It was this observed asymmetry that motivated the improved sparger design, previously discussed.
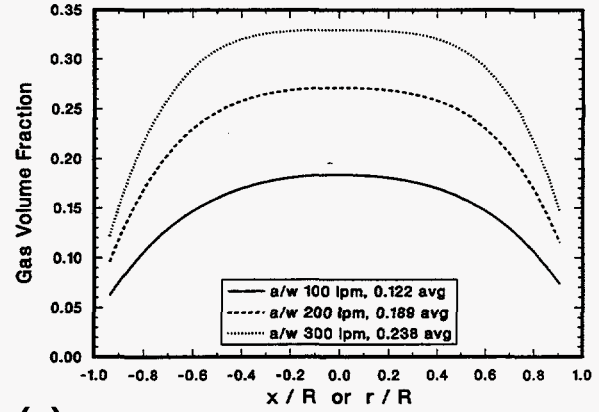
Table 3. Average gas volume fractions in TBC.

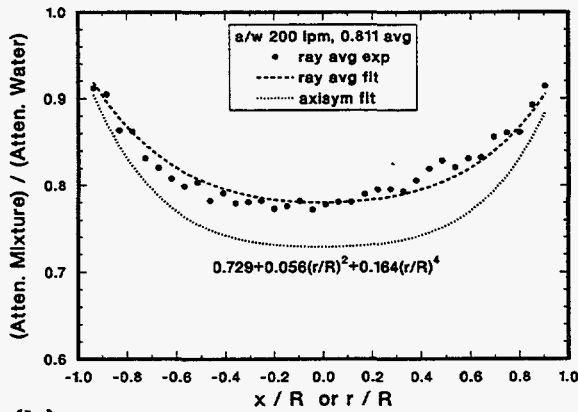| Air Flow (lpm)	Solid Phase	Sup. Vel. (cm/s)	LR	DP	GDT
100	absent	5.9	0.11	0.11	0.12
200	absent	11.8	0.17	0.17	0.19
300	absent	17.7	0.22	0.20	0.24
300	present	17.7	-	-	0.23

For three-phase flow, GDT and the phase rule (phase volume fractions sum to unity) do not provide enough information to determine all three unknown phase-volume-fraction spatial distributions (i.e. for air, water, and sand). To achieve closure, an additional relation is required. One possible assumption is that all of the sand suspended in the flow (as differentiated from the sediment layer of sand at the bottom of the column) is distributed uniformly within the liquid phase: the solid and liquid volume fractions are proportional throughout the flow. Since the bubble-induced mixing appears strong, this assumption seems reasonable. Note, however, that this assumption constrains the radial variations of the liquid and solid volume fractions to be proportional.

(a)

a/w 100 lpm, 0.878 avg
• ray avg exp
- - - ray avg fit
······ axisym fit

$0.816+0.076(r/R)^2+0.071(r/R)^4$

(b)

a/w 200 lpm, 0.811 avg
• ray avg exp
- - - ray avg fit
······ axisym fit

$0.729+0.056(r/R)^2+0.164(r/R)^4$

(c)

a/w 300 lpm, 0.762 avg
• ray avg exp
- - - ray avg fit
······ axisym fit

$0.671+0.017(r/R)^2+0.251(r/R)^4$

(d)

a/w/s 300 lpm, 0.873 avg
• ray avg exp
- - - ray avg fit
······ axisym fit

$0.766+0.061(r/R)^2+0.231(r/R)^4$

(e)

a/w 100 lpm, 0.122 avg
a/w 200 lpm, 0.189 avg
a/w 300 lpm, 0.238 avg

Mixture attenuation coefficients:
    (a) 100 lpm, gas-liquid
    (b) 200 lpm, gas-liquid
    (c) 300 lpm, gas-liquid
    (d) 300 lpm, gas-liquid-solid
Experimental results for attenuation:
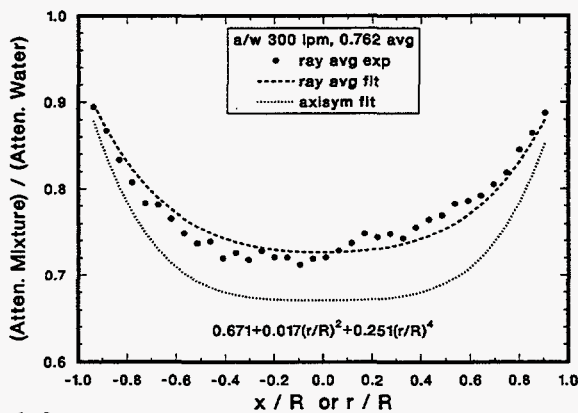   Symbols: averages along path (ray)
Computational results for attenuation:
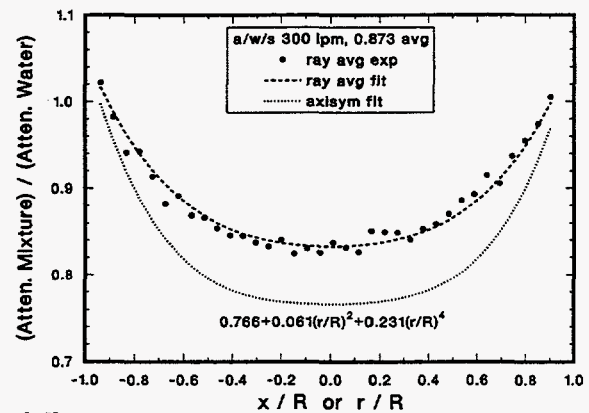   Dashed curves: polynomial fits to symbols
    Dotted curves: polynomial reconstructions
Gas-volume-fraction summary plot:
    (e) 100, 200, 300 lpm, gas-liquid

Figure 39. Gas-liquid and gas-liquid-solid results from GDT in TBC.

77

To determine the constant of proportionality, it is necessary to determine the amount of sand suspended during air flow. This was accomplished by measuring the height of the sediment layer that remained unsuspended during air flow and using the known volume fraction of sand in the sediment layer, 0.63. This quantity had been determined prior to the experiments in the following manner. A large graduated cylinder was filled with 1000 cm^3 of water (991 g mass) and 1000 cm^3 of (initially dry) sand (1534 g mass). The water-sand mixture was composed of two regions, a sediment region on the bottom and a water region on the top. The total volume of these two regions was measured to be 1630 cm^3, yielding a sand volume of 630 cm^3. Thus, densely packed sand has a volume fraction of 0.63. As a check, the intrinsic mass density of the sand grains was calculated from the above mass and volume and found to be 2.44 g/cm^3, which is close to the value of 2.65 g/cm^3 for pure SiO$_2$ (cf. Weast, 1973). An additional check comes from the GDT horizontal scan of the sediment without air flow, which indicated a normalized attenuation coefficient of 1.937 for the sand-water sediment. Since the sediment has a sand volume fraction of 0.63 and a water volume fraction of 0.37, the normalized attenuation coefficient for sand is 2.487. Since the attenuation coefficient of water is 0.0858 cm^{-1}, the experimentally determined attenuation coefficient for sand is 0.2134 cm^{-1}, which is close to the theoretical value of 0.2041 cm^{-1} for pure SiO$_2$ (Lamarsh, 1983).

Prior to initiating air flow, 8.37 kg of sand, with an equivalent height of 19.1 cm, was added to the TBC experiment, which had previously been filled with water to a height of 76.2 cm. When an air flow of 300 lpm was initiated, the undistorted sediment layer remaining on the bottom was found to be 7.6 cm thick, so the suspended water and sand (i.e. not in the sediment region) have effective heights of 73.4 cm and 7.2 cm, respectively. The ratio of these heights yields a value of 0.098 for the constant of proportionality relating the sand and water volume fractions (valid only for this particular experiment). Figure 39 shows the normalized mixture attenuation as a function of horizontal or radial position for these flow conditions. Note that the normalized mixture attenuation exceeds unity near the side wall. This is possible because the attenuation coefficient of sand is more than twice the attenuation coefficient of water, which was used in the normalization. Figure 40 shows the volume-fraction radial profiles for gas-liquid and gas-liquid-solid flow at 300 lpm, with average values shown in the plot legends. Interestingly, the solid phase had only a minimal effect on the air volume fraction, both in average value and in radial variation. This observation should not be assumed to apply in general to other experimental conditions.
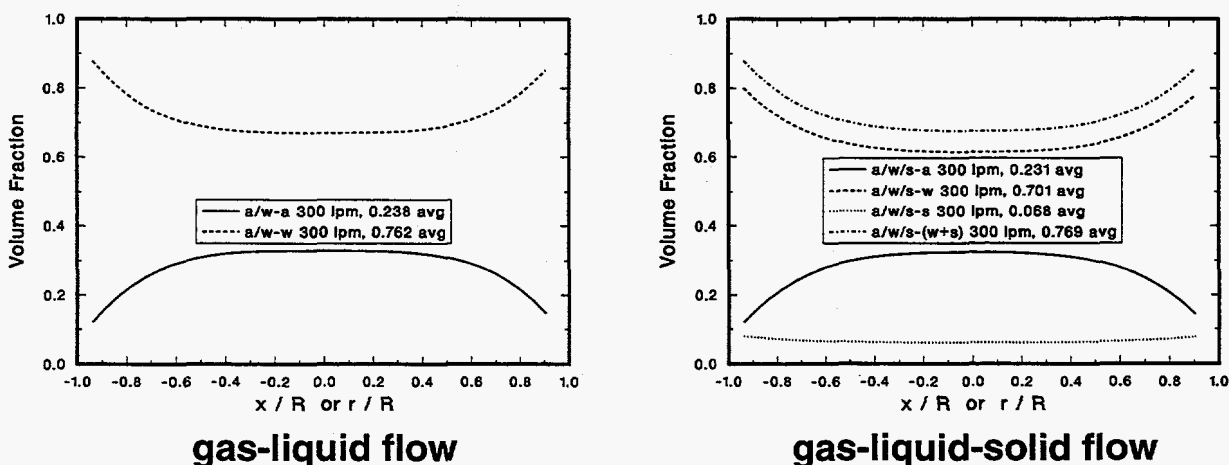

gas-liquid flow   **gas-liquid-solid flow**

Figure 40. Phase volume fraction results from GDT in TBC.

78

4.2. Slurry Bubble-Column Reactor (SBCR) Experiment

A slurry-bubble-column reactor (SBCR) experiment served as a test bed for diagnostics development and is shown in Figure 41. This test bed is capable of operation at the large pressures, temperatures, gas flow rates, and length scales of industrial interest. Despite its size, this bubble column enables implementation and modification of many, but not all, of the diagnostic techniques previously discussed. Optical techniques, such as flow visualization and LR, can be applied only in a limited sense through the view ports. Pressure-based techniques, such as DP, can be applied because of the availability of pressure ports through the side wall. Radiation-based techniques, such as GDT, can be used despite the thick, high-density side wall. The application of electrical techniques, such as BEI, EIT, and the EBP, inside the SBCR vessel remains a subject of research due to the conducting wall. Limited geometric modifications, such as installation of alternate spargers, probe rings, or internals, can be carried out without excessive difficulty.
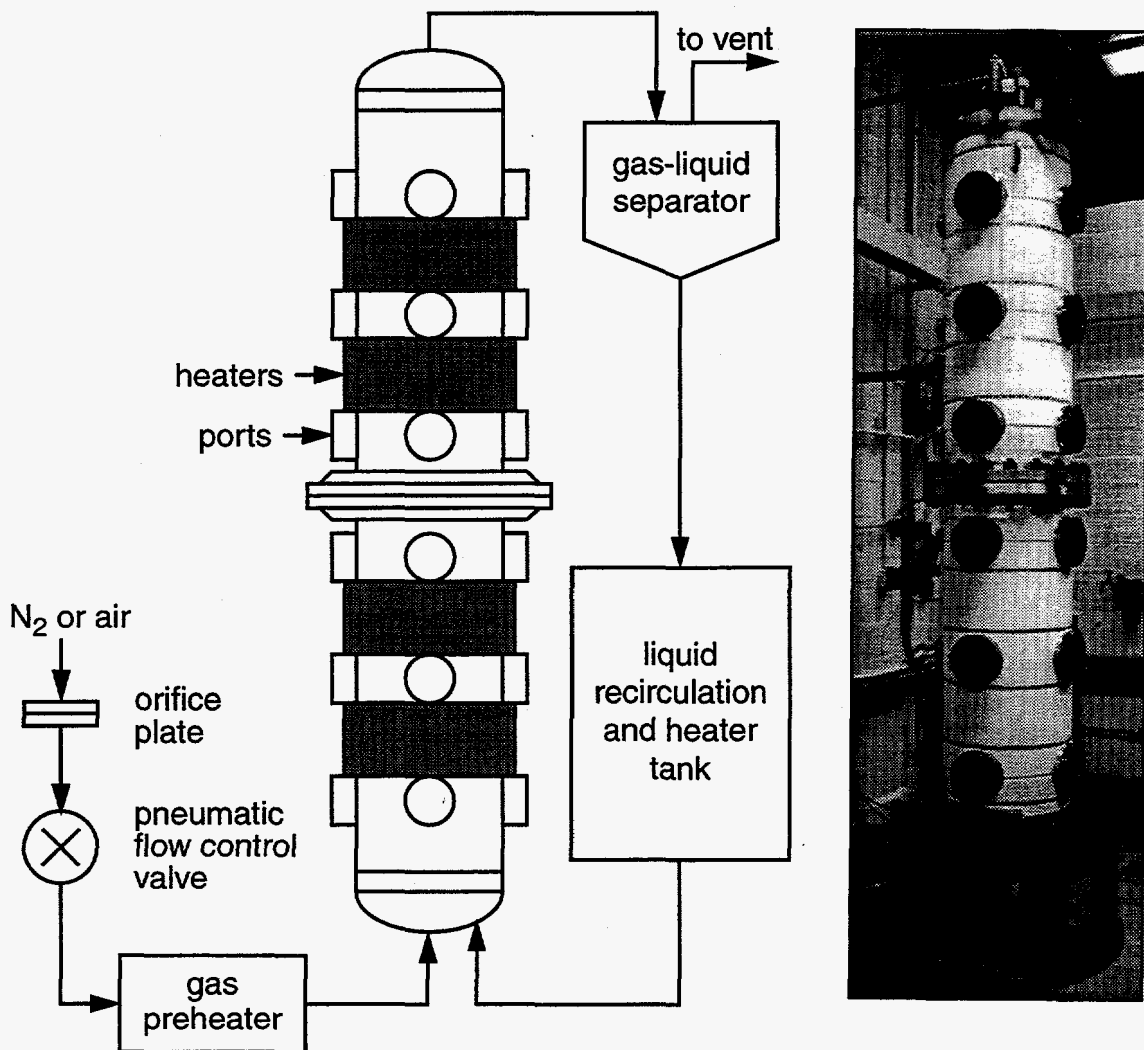

Figure 41. The slurry bubble-column reactor (SBCR) experiment.

4.2.1. SBCR Experimental Setup

An SBCR experiment, shown in Figure 41, has been utilized to facilitate development and validation of multiphase-flow diagnostics capable of operating at industrially relevant conditions. The vessel is made out of stainless steel and has an inner diameter of 0.48 m (19.0 inch), a height of 2.75 m, and a wall thickness of 1.27 cm (0.5 inch). The vessel has 12 visual ports and 12 instrumentation ports distributed at 6 vertical locations, with the 4 ports (2 of each type) at each vertical location separated by 90° intervals. Pressure transducers and thermocouples are installed at instrumentation ports at each vertical level and at other critical locations throughout the flow system. A computer-controlled data acquisition system and custom software are available to monitor, record, and control flow conditions.

The Sandia wind tunnel supply of clean, dry air is used to produce the air flow within the SBCR vessel. Gas is drawn from a 50 ft^3 surge tank, which is maintained at 255 psi by a 5200 ft^3 air storage tank. A sparger is used to introduce the gas into the vessel. The sparger is a 15 cm diameter toroidal ring formed from 1.1 cm diameter stainless steel tubing with 12 upward-facing holes with diameters of 0.3175 cm (0.125 inch) at equal azimuthal spacing. The gas velocity entering the vessel is set using a pneumatic flow control valve that uses the pressure drop across an orifice plate as the control parameter. Gas flow rates are calculated from the orifice plate pressure differential and other relevant flow conditions, and the pressure inside the vessel is maintained using a back-pressure regulator. Gas superficial velocities of up to 0.4 m/s, which produce churn-turbulent flows in most liquids, and gas volume fractions up to 0.4 can be routinely achieved in the SBCR vessel with this gas flow system. Gas is exhausted through a pipe with an inner diameter of 3.3 cm (1.3 inch) from the top of the vessel, passes through a cyclone gas-liquid separator to remove any entrained liquid droplets, and is vented to a fume hood duct leading to the roof.

Operation of the SBCR experiment is possible for pressures up to 690 kPa (100 psig) and for temperatures up to 200 °C. Elevated temperatures in the column are attained by preheating the gas to the desired temperature using a 50 kW preheater. Further temperature control is achieved by four sets of 3 kW silicone rubber heaters located at four axial locations along the vessel and covered by a layer of insulation. Each set of heaters is controlled separately, allowing the vessel to be maintained at either uniform or axially varying temperature distributions. Tests indicate that temperature uniformity can be maintained to within 2 K inside the vessel.

4.2.2. SBCR Experimental Results

Gas-liquid experiments have been performed in the SBCR vessel using water and Drakeol 10 with air sparging at several pressures (Adkins et al., 1996; Jackson et al., 1996ab). Drakeol 10 is a light mineral oil used in SBCRs. A wide pressure range was examined because gas-liquid bubble-column flow is known to depend significantly on pressure. The vessel is filled to four diameters above the sparger prior to initiating air flow, and GDT scans are taken two diameters above the sparger. Additionally, DP is used to determine average gas holdup values for the volumes between pairs of transducers. Figure 42 shows the DP gas holdup results for air-water and air-Drakeol 10 at gas superficial velocities up to 0.25 m/s and pressures up to 432 kPa (62.6 psia). Also shown are predictions of the Zuber-Findlay correlation (Zuber and Findlay, 1965):

$$\varepsilon_G = \frac{U_G}{C_0 U_G + C_1 [\zeta g (\rho_L - \rho_G)/\rho_L^2]^{1/4}} \approx \frac{U_G}{C_0 U_G + C_1 [\zeta g / \rho_L]^{1/4}}, \tag{57}$$

where ε_G is the average gas holdup, U_G is the gas superficial velocity, ρ_L and ρ_G are the liquid and gas densities, ζ is the surface tension, g is the gravitational acceleration, and both C_0 and C_1 are empirical coefficients determined from this data set so that the correlations fit this data set:

$$C_0 = \left\{ \begin{array}{l} 8.43 \exp[-P/(138 \text{ kPa})] \text{ air-water} \\ 3.83 \exp[-P/(460 \text{ kPa})] \text{ air-Drakeol 10} \end{array} \right\}, \, C_1 = \left\{ \begin{array}{l} 1.53 \text{ air-water} \\ 2.13 \text{ air-Drakeol 10} \end{array} \right\}. \qquad (58)$$
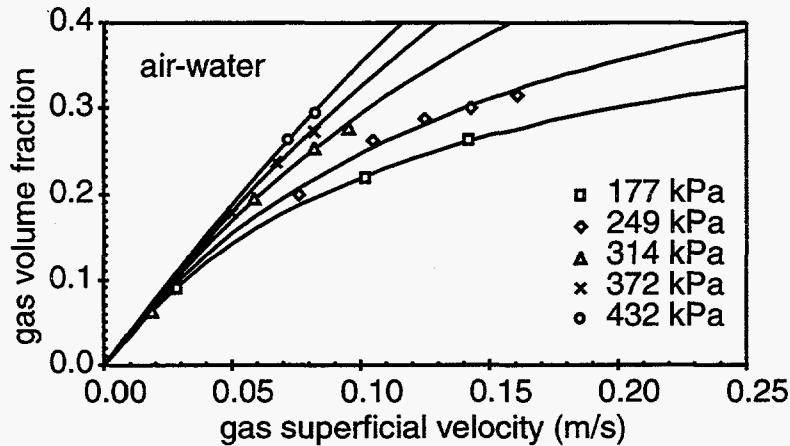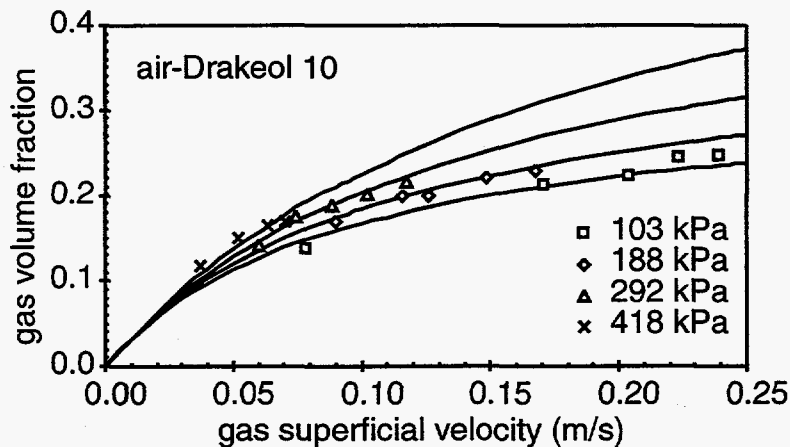
Figure 42. Gas volume fraction results from DP for gas-liquid flow in SBCR.

Figure 43 shows GDT results for gas-liquid experiments with air-water and air-Drakeol 10, with 30 s and 60 s of counting time per point, respectively. One GDT scan is shown for each liquid, and gas-volume-fraction radial profiles are shown as functions of gas superficial velocity and pressure. Gas volume fractions are significantly higher with water than with Drakeol 10 despite the fact that Drakeol 10 is 30 times as viscous as water. For both liquids, increasing the pressure while holding the gas superficial velocity constant increases the gas volume fraction uniformly throughout the flow, whereas increasing the gas superficial velocity while holding the pressure constant increases the gas volume fraction more near the axis than near the side wall.
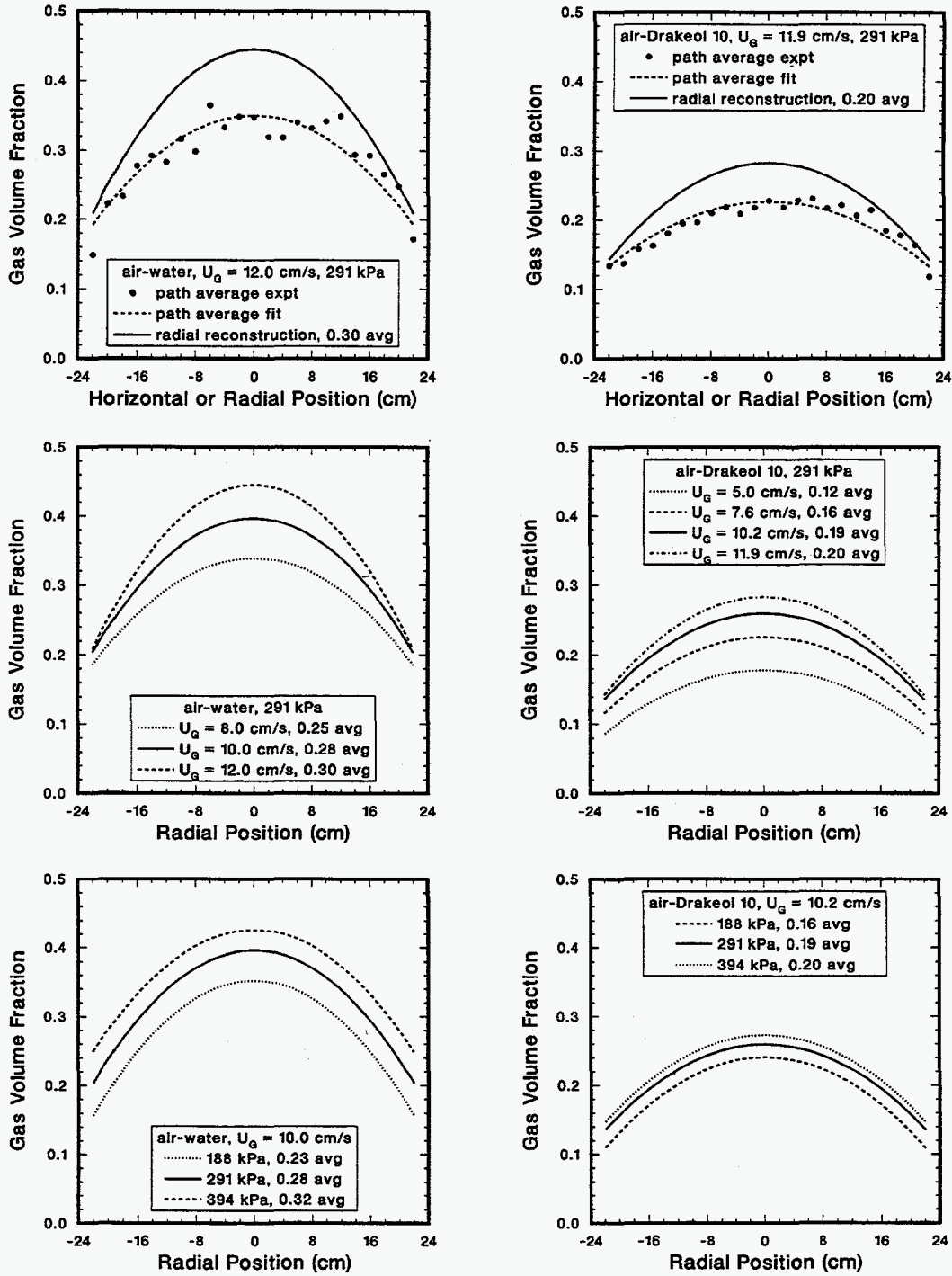
all scans at L/D = 2

Figure 43. Gas volume fraction results from GDT for gas-liquid flow in SBCR.

Table 4. Average gas volume fraction values from GDT and DP for air-water in SBCR.

P (kPa)	U_G (cm/s)	ε_G^{GDT}	ε_G^{DP}
141	12.5	0.21	0.21
208	14.6	0.27	0.25
253	15.7	0.29	0.29
230	8.6	0.20	0.20
285	10.8	0.25	0.25
330	12.0	0.28	0.31
299	6.6	0.19	0.20
360	8.6	0.24	0.24
390	10.2	0.27	0.29

Table 4 and Figure 44 show a comparison of the average gas volume fractions from GDT and DP for air-water and air-Drakeol 10 tests in the SBCR experiment. The DP results are plotted as a function of vertical position normalized by the SBCR vessel diameter and represent volumetric averages over approximately one diameter of height centered about the plotted points. The GDT results are shown as solid symbols. For a wide range of pressures and gas superficial velocities, the GDT and DP values are seen to be in reasonable agreement for the air-water tests. A similar comparison for air-Drakeol 10 does not yield quite as good agreement, with the GDT values slightly but systematically lower than the DP values. The cause of the discrepancy is not known at present and will be the focus of future investigations. It may be related to the fact that the gas volume fraction values determined by DP do not vary strongly with vertical position in the air-water tests, suggesting that the flow is nearly fully developed. For the air-Drakeol 10 tests, the DP results indicate that the gas distribution is changing considerably in the vertical direction. The DP technique is believed to be most accurate for fully developed flow, so the GDT results are conjectured to be more accurate for the air-Drakeol 10 tests. From these results it is clear that the range of applicability of DP continues to remain a topic of investigation.
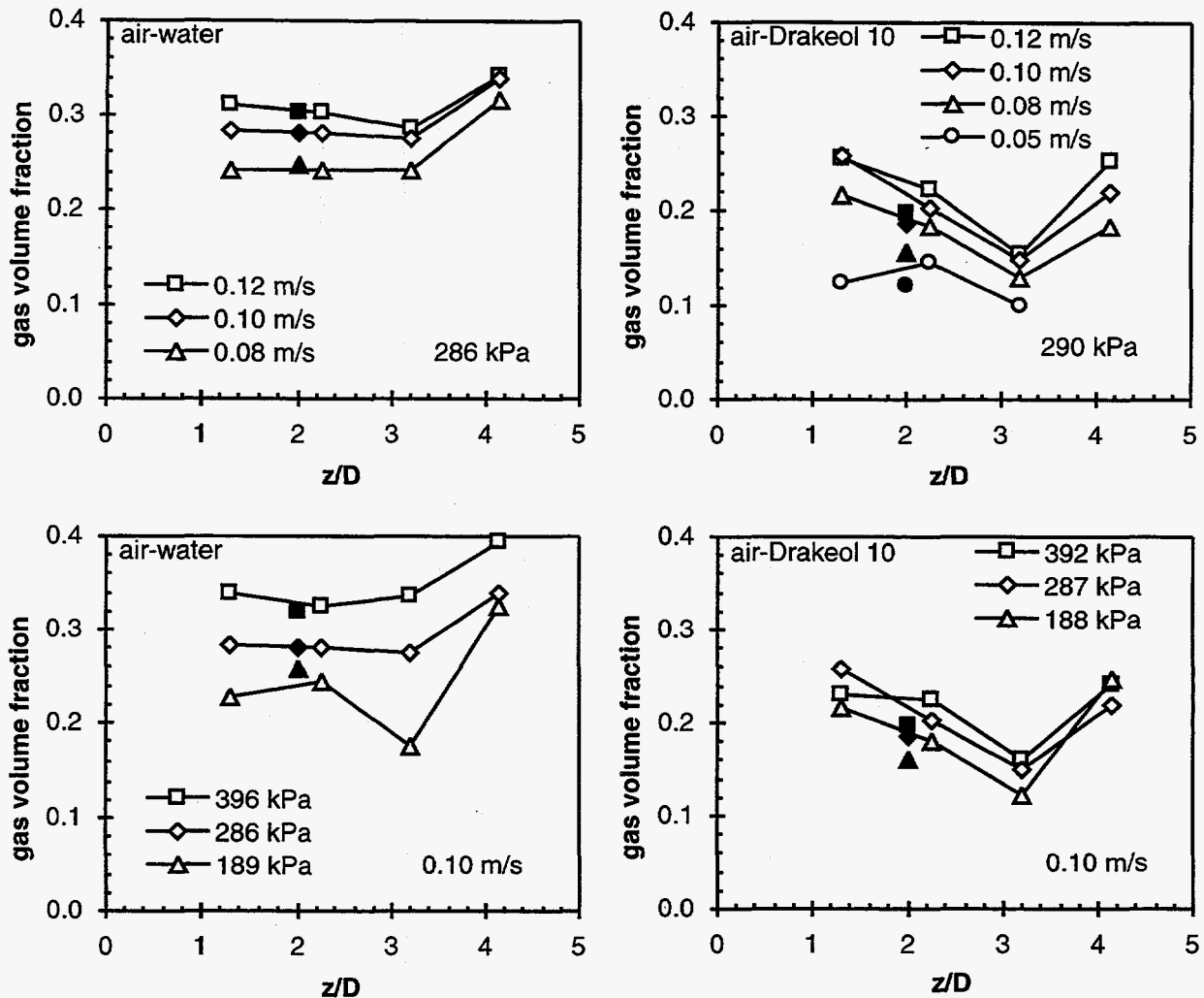
Figure 44. Gas volume fraction vertical variation from DP and GDT in SBCR.

4.3.   Two-Phase Experiments Combining GDT and EIT

As has been previously discussed, measuring material distribution in three-phase flows requires application of two complementary diagnostic techniques, such as GDT and EIT. A necessary preliminary step en route to three-phase measurements is the application of GDT and EIT to two-phase flows since each technique should be capable of independently determining the phase volume fraction spatial variation. Since the GDT system has already been validated extensively for gas-liquid flows, as presented in previous sections, it can be used to assess the behavior the EIT system for multiphase-flow measurements. To this end, two types of multiphase flow are examined with both techniques: liquid-solid flows with dilute concentrations of small spherical insulating solid particles mixed uniformly in a conducting liquid, and gas-liquid flows in the TBC experiment. The latter is a more rigorous test since the gas bubbles are larger, nonspherical, deformable, densely concentrated, and nonuniformly distributed.

84

4.3.1. Liquid-Solid Flow (LSF) Experiment

A liquid-solid flow has been examined with both GDT and EIT to validate the quality of the measurements taken with EIT. A flow of particle-laden liquid was chosen for investigation for several reasons. First, the amount of solid introduced into the experiment can be carefully controlled and, for a closed volume, remains constant for all time. Knowledge of the average solid volume fraction thus provides a good check on the diagnostics. Second, unlike gas bubbles, solid particles can be small, uniform-diameter spheres that do not deform or otherwise change their shape during the experiment (so long as conditions are not harsh enough to fracture the particles). Third, a mixer can be employed to generate a relatively uniform distribution of solids throughout most of the flow geometry. Fourth, the solid particles and the liquid medium can be chosen without difficulty to have significantly different gamma attenuation coefficients and electrical conductivities so that both GDT and EIT can be applied to determine the phase volume fraction spatial variation.

Schematic diagrams of the experimental setup and diagnostics are shown in Figure 45. The flow apparatus consisted of a Lexan cylinder (19 cm inner diameter, 0.635 cm wall thickness, 76 cm height) closed at the bottom and the top, into which a mixer was inserted. A Sargent-Welch mixer (model S-76509-80B) was used. The mixer system consisted of a compact impeller assemblage positioned 1 cm above the bottom of the cylinder interior, a motor mounted above the top end of the cylinder, and a shaft (0.8 cm diameter with the coating, described below) connecting the impeller to the motor. The shaft passed through a small concentrically-positioned hole in the top end of the cylinder, around which an "overflow" volume was placed to ensure the absence of free-surface effects (e.g. a vortical "funnel" due to swirling) in the cylinder interior during mixing. A mixer speed of 600 rpm was used for all solid volume fractions, as needed to achieve a roughly uniform distribution (to the eye) of particles within the liquid. For solid volume fractions much in excess of 0.03, large fluctuating motions and solid volume fraction variations were visually apparent, so solid volume fractions were restricted in this study to no larger than about 0.03 although even at this value some solid volume fraction variations were discernible.

The nominal (volume-averaged) solid volume fraction ε_s^{NOM} was specified in the following manner. Glass spheres with a mean diameter of 80 µm were used. A prescribed volume of these spheres, as determined by weight and the known density of the glass, was introduced into the cylinder, and water was added until the remaining volume was filled. Water was selected because its electrical conductivity can be adjusted by dissolving a small known amount of salt (sodium chloride) in it. Typical electrical conductivities of the salt-water solution were around 1 mS/cm. However, temperature variations and their effects on the precise ionic composition of water were large enough to alter the conductivity appreciably, necessitating the calibration measurements discussed below. Glass spheres were selected for the following reasons. First, they are fairly rugged and are easily separated from water by settling. Second, glass is an insulator compared to (non-deionized) water, so EIT can in principle discriminate between glass spheres and water. Third, glass attenuates gamma photons more strongly than does water, so GDT can also discriminate between glass and water.

The presence of the mixer shaft is somewhat problematic for both techniques. For GDT, it produces extra attenuation when the gamma beam passes through it. In this study, these anomalous points are not used in performing the reconstruction. For EIT, placing a good conductor like the mixer's steel shaft in the center of the cylinder would significantly distort the electric field lines, so the shaft and impeller were coated with a layer of insulating paint to mitigate this effect. The presence of a small-diameter (relative to the cylinder), concentrically-positioned, insulated inclusion was expected to have only a small effect on the electrical behavior of the system, and this was verified by taking EIT measurements using water (no particles) both with and without the mixer shaft.
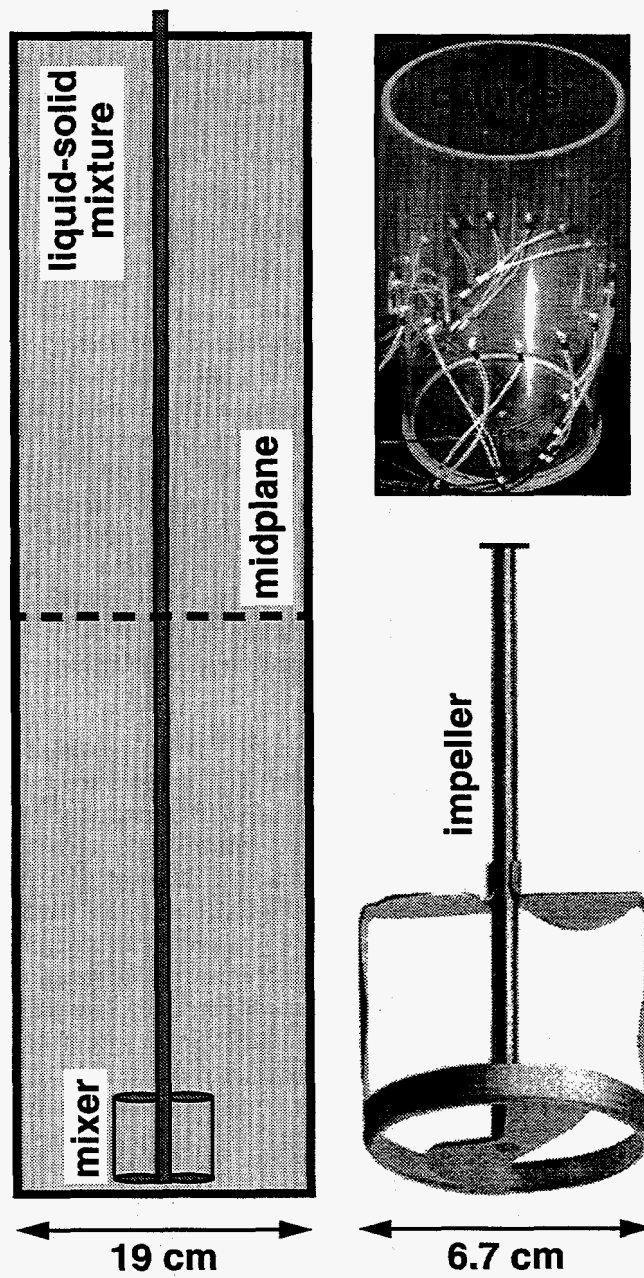
Figure 45. The liquid-solid flow (LSF) experiment.

Three sets of experiments were performed in this study, as summarized in Table 5. In each set, a prescribed amount of glass spheres was introduced to the cylinder, and the remainder of the volume was filled with water. Mixing was then initiated for a 30-minute period, which was determined to be long enough for the system to come to a statistically stationary state. GDT and EIT were successively applied, where the GDT and EIT scans required 4 and 10 minutes, respectively. Mixing was then terminated, and the solid-liquid mixture was allowed to remain quiescent for a 5-minute period, which was long enough for the spheres to settle to the bottom of the water-filled cylinder. Following this settling period, EIT was applied again. This second EIT measurement was necessary for calibration purposes because the conductivity of the water was altered by soluble contaminants unavoidably introduced when the spheres were added. Although this trace amount of contaminant material had a negligible effect on GDT, as verified by additional GDT measurements, its effect on the water conductivity was comparable in magnitude to that of the suspended solid particles.

Table 5. Conditions and results for LSF experiment.

| Case	ε_s^{NOM}	$[\mu_m/\mu_w]_{av}$	ε_s^{GDT}	$[\sigma_m/\sigma_w]_{av}$	ε_s^{EIT}
1	0.010	1.015	0.011	0.982	0.012
2	0.020	1.030	0.021	0.968	0.021
3	0.030	1.057	0.040	0.940	0.041

Figure 46 shows a compilation of results corresponding to the cases delineated in Table 5. One of the plots shows the GDT measurements of μ_m/μ_w, the path-averaged mixture attenuation coefficient normalized by the attenuation coefficient of water, as a function of x/R, the normalized horizontal position of the measurement path. The data points near $x = 0$ are anomalous because the gamma beam passes through or near the mixer shaft and are not shown. Several observations can be made from this plot. First, despite some variations due to the unsteady nature of the flow, the profiles are relatively uniform. Second, μ_m/μ_w increases monotonically with increasing ε_s^{NOM}. The GDT reconstruction algorithm was used for these cases to determine $[\mu_m/\mu_w]_{av}$, the average of μ_m/μ_w in the cross section, as shown in Table 5 and in Figure 46 plotted against ε_s^{NOM}. In these calculations, the attenuation coefficient profile was taken to be spatially uniform. Additional calculations performed using radially parabolic profiles were found to yield almost identical profiles and averages (the reconstructions were not improved significantly in quality by the additional degree of freedom). The $[\mu_m/\mu_w]_{av}$ values were converted into the solid volume fractions ε_s^{GDT} in Table 5 and in one of the plots in Figure 46 using the following relation:

$$\varepsilon_s^{GDT} = \frac{[\mu_m/\mu_w]_{av} - 1}{[\mu_s/\mu_w] - 1}, \tag{59}$$

where the attenuation coefficients of water and the glass spheres are given by $\mu_w = 0.0858$ cm^{-1} and $\mu_s = 0.209$ cm^{-1}. The EIT reconstruction code EITA3D was applied to determine $[\sigma_m/\sigma_w]_{av}$, the average electrical conductivity of the mixture normalized by that of the liquid, which is shown in Table 5 and in Figure 46 plotted against ε_s^{NOM}. Nearly identical average conductivities were obtained when using either a spatially uniform conductivity distribution or a radially parabolic distribution, so a uniform distribution was employed, being simpler and equally accurate for this experiment. The quantity $[\sigma_m/\sigma_w]_{av}$ is seen to decrease monotonically with increasing ε_s^{NOM}. The $[\sigma_m/\sigma_w]_{av}$ values were converted into the solid volume fractions ε_s^{EIT} in Table 5 with the Maxwell-Hewitt relation:

$$\varepsilon_s^{\text{EIT}} = \frac{1 - [\sigma_m/\sigma_w]_{\text{av}}}{1 + (1/2)[\sigma_m/\sigma_w]_{\text{av}}}.$$ (60)
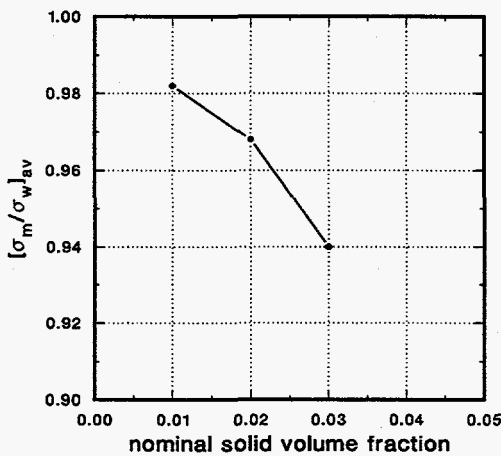
The solid volume fractions determined by GDT and EIT are in close agreement with each other for all cases and with the nominal values for the first two cases. Case 3 is interesting in that the GDT and EIT values are in agreement with each other but are somewhat higher than the nominal value. It is conjectured that the mixing may not have been strong enough to produce a uniform axial distribution of glass spheres throughout the cylinder for a nominal solid volume fraction of 0.03.
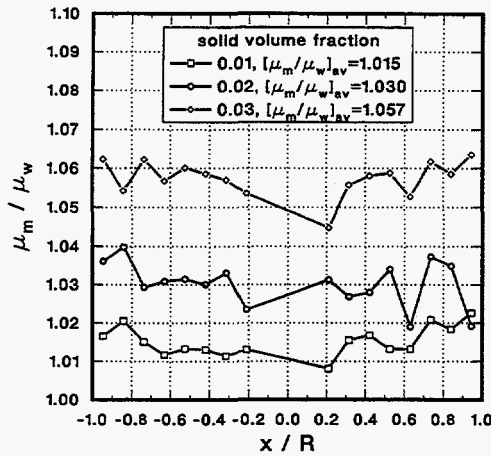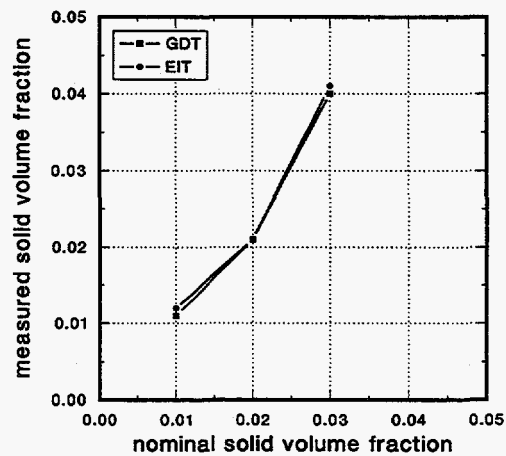

(a) GDT scans
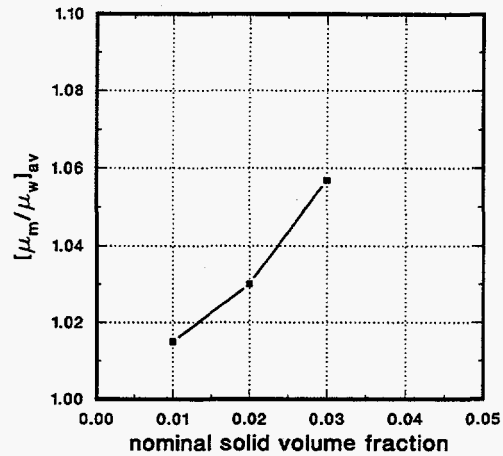
(b) average attenuation from GDT

(c) average conductivity from EIT

(d) volume fractions from GDT and EIT

Figure 46. Solid volume fraction results from GDT and EIT in LSF.

4.4. Application of GDT and EIT to TBC

As previously indicated, two types of information are required to determine material distribution in three-phase flows. For gas-liquid-solid flows, GDT and EIT are good candidates for such measurements. GDT is most sensitive to the presence of the dense phases (the liquid and the solid), EIT observes the presence of the conducting phases (usually the liquid), and the remainder of the volume is filled with the nondense nonconducting phases (usually the gas). However, EIT, being less technically mature than GDT, requires extensive validation in two-phase flows prior to application to three-phase flows, for which direct validation may not be possible. The LSF experiment was the first step toward this validation, employing a conducting liquid phase and an insulating solid phase. This experiment has several features not present in many two-phase flows of interest. The dispersed phase was composed of solid particles that were small compared to any macroscopic dimensions, approximately spherical, geometrically unchanging, volumetrically fairly dilute, and fairly uniformly distributed in space.

It is of interest to apply EIT to a two-phase system without these features as a more rigorous validation test. This is particularly important since the Maxwell-Hewitt relation relies on spherical particles that are small compared to the curvature of mean field lines and are randomly but statistically uniformly distributed in space. Bubble-column flows severely strain these assumptions at higher gas volume fractions. For example, a simple-cubic lattice of touching spheres has a volume fraction of $\pi/6 \approx 0.52$, so gas volume fractions around 0.4 (often observed) probably produce bubbles with shapes that are significantly deformed from spheres.

Two-phase gas-liquid flow in the TBC experiment was selected for this type of validation exercise. As in the LSF experiment, the dispersed phase (air bubbles) is insulating, and the liquid phase (water) is conducting. However, the bubbles are typically on the order of a few millimeters in diameter which is substantially bigger than the 80 μm glass spheres used in the LSF experiment and comparable to the electrode size in the EIT point-electrode probe ring. Bubbles of this size are fairly deformable, unlike the glass spheres, and gas volume fractions on the order of 0.3 can be routinely achieved, as opposed to the maximum value of about 0.04 encountered in the LSF experiment.

Both GDT and EIT were applied to the TBC experiment to measure material distribution in gas-liquid flow. Air and water were chosen to be the working fluids, and the toroidal-ring sparger was employed for these experiments. Figure 47 shows a schematic of the TBC experiment including the measurement plane (diagram at left), the TBC with the GDT system in place (photograph in middle), and the TBC with the EIT system in place (photograph at right). In this application, the EIT probe ring with point electrodes was employed. This probe ring samples the volume of the TBC experiment within plus or minus roughly one diameter of the measurement plane. As indicated previously for electrical techniques, a small amount of salt was added to the water to set the conductivity to approximately 1 mS/cm, and heaters placed at four vertical stations were active to prevent conductivity changes due to air-flow-induced evaporation of water.
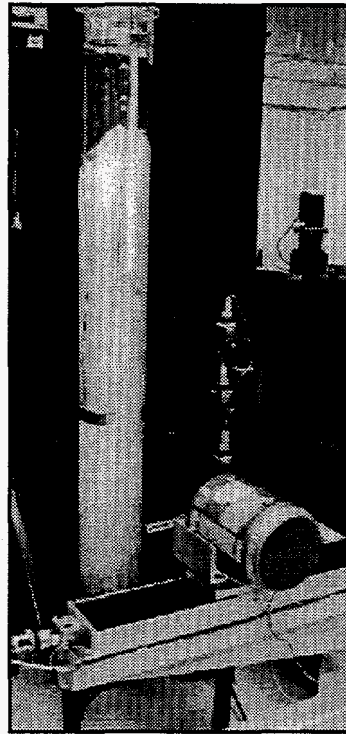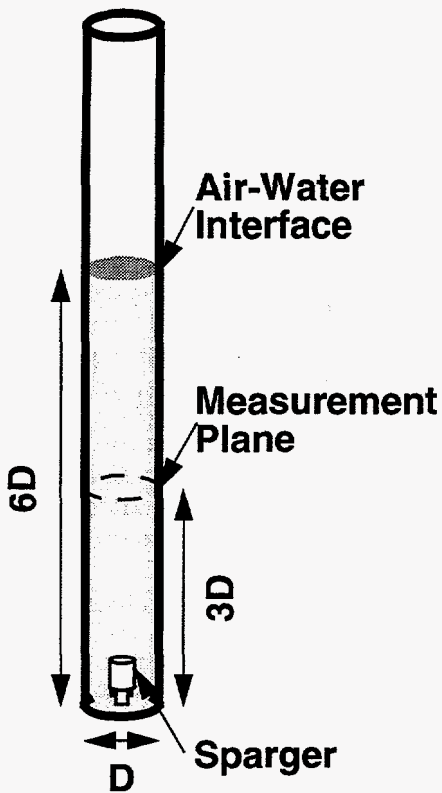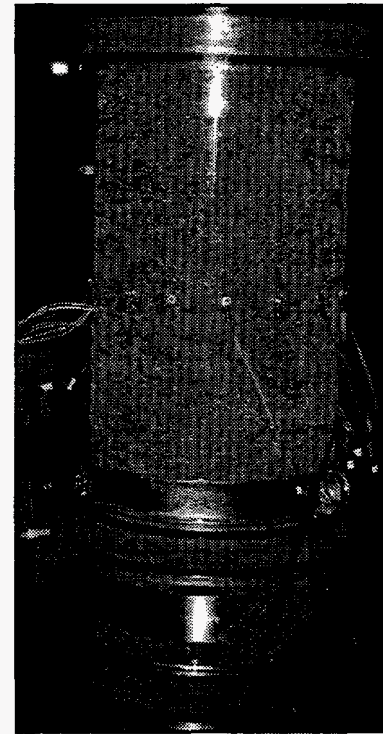
Figure 47. GDT and EIT installed in TBC for measuring gas-liquid flow.

Two air flow rates were examined in the TBC experiment: 100 and 200 lpm, which correspond to gas superficial velocities of 5.9 and 11.8 cm/s, respectively. GDT measurements were taken at 1 cm intervals across the measurement plane, and a parabolic attenuation profile was used to perform the reconstruction. Higher-degree polynomials were not found to give significantly different reconstructions. The EIT probe ring with 16 point electrodes was used to acquire voltage data, and the code EITA3D was used to perform the reconstructions. The EIT voltages used to perform the reconstructions were the averages of 6400 complete EIT measurements (i.e. each of the 1920 voltages from the 120 source-sink electrode pairs is measured 6400 times). A parabolic variation in conductivity was used by EITA3D to produce the reconstructions, and the Maxwell-Hewitt relation was used on a point-by-point basis to convert the conductivity profile into a gas volume fraction profile. Note that a parabolic conductivity profile is not transformed into a parabolic gas volume fraction profile by the Maxwell-Hewitt relation.
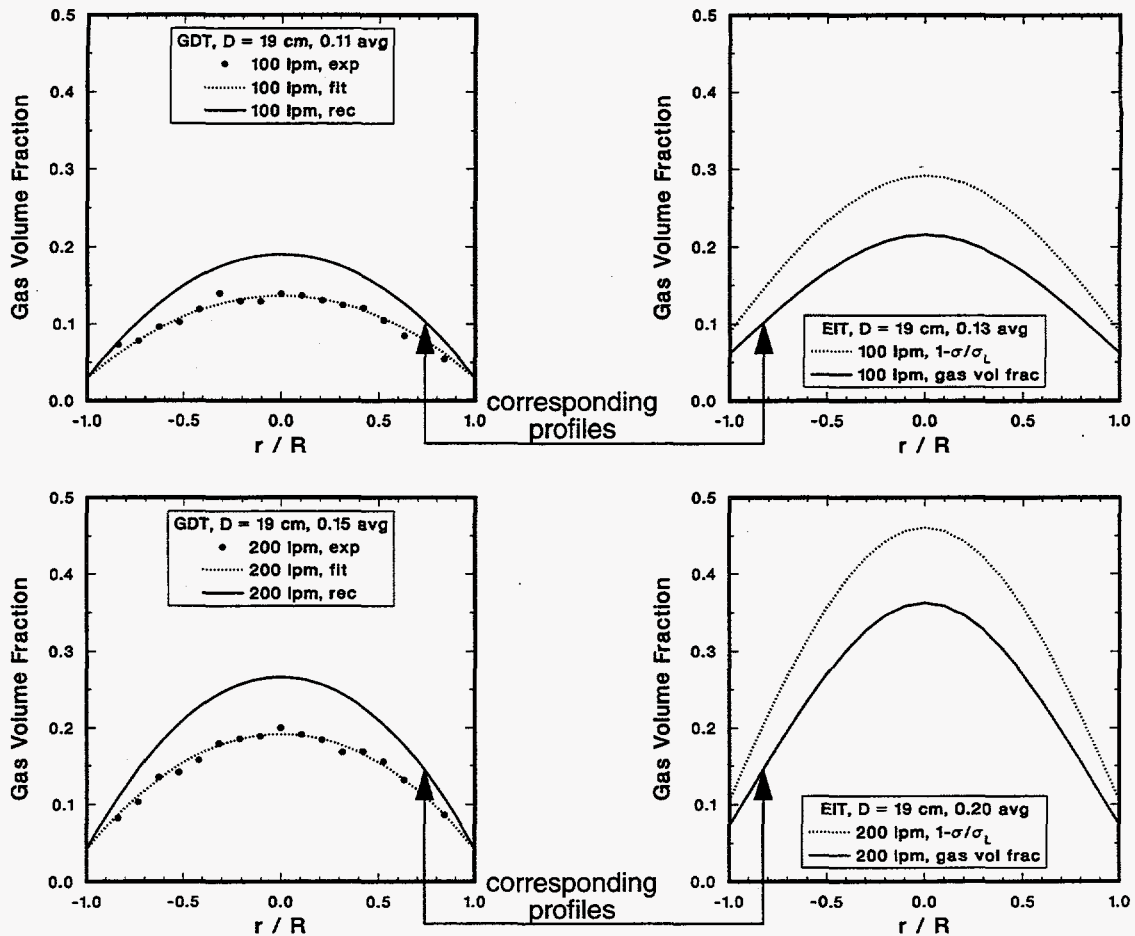
Figure 48. GDT and EIT results at same conditions in TBC.

Figure 48 shows GDT and EIT results in the TBC experiment for the two air flow rates examined. The GDT results are shown on the left, with symbols denoting the path-averaged values, the dotted curves denoting quadratic polynomials fits through the symbols, and the solid curves denoting the reconstructed gas volume fraction profiles. The GDT results exhibit high symmetry with the improved sparger design, suggesting that the assumption of axisymmetry is a good one although nonaxisymmetric variations cannot be rigorously ruled out. As is generally observed, the gas volume fraction is largest on axis and smallest at the side walls and increases preferentially near the axis with increasing gas flow rate. The EIT results are shown on the right side of Figure 48, with the dotted curves denoting the reconstructed conductivity profiles and the solid curves denoting the reconstructed gas volume fraction profiles. The EIT gas-volume-fraction profiles exhibit the same features but have somewhat higher values than the GDT profiles. The GDT profiles were found to be in good agreement with DP results and therefore are believed to be the more accurate. The over-prediction by EIT of the gas volume fraction in the TBC gas-liquid flows is reminiscent of the fact that EIT slightly but consistently overpredicted the diameters of ICIs: the amount of insulator is slightly overestimated in both types of validation exercises.

Several effects have been investigated or are currently under investigation as possible causes for this overprediction. The presence of a grounded conductor anywhere in the column was found to exert a profound effect on the EIT data, so all conducting fittings, including the sparger, were removed or electrically isolated prior to acquiring the data shown in Figure 48. Since the electrical conductivity of water decreases with decreasing temperature caused by evaporation, heaters were used to maintain a constant water temperature to within 0.1 K, which greatly reduces spurious changes in conductivity due to temperature. Other possibilities for the observed discrepancy include electronics and capacitive effects, electrode size (comparable to bubble size so that bubbles could conceivably cover electrodes), the parabolic representation of the conductivity spatial variation in the code EITA3D, the Maxwell-Hewitt relation used to convert electrical conductivity to gas volume fraction, and temporal averaging that occurs due to the time needed to acquire a data set.

The most likely causes of the discrepancy probably are capacitive effects, electrode size, temporal averaging, and the parabolic representation of the conductivity field. These will be systematically addressed in the next EIT probe ring, which is currently under development. Electrodes will be somewhat larger, perhaps about 1 cm in diameter, and only 8 electrodes will be used. This will increase the signal-to-noise ratio by considerably reducing the voltage drop experienced when current enters or exits the multiphase flow so that the voltage differences between electrodes will be a much larger proportion of the total voltage difference between the source and the sink. Using fewer but more sensitive electrodes will also reduce the temporal averaging that is required. The possibility of an electrode being covered by a bubble or bubbles will also be greatly reduced. Since capacitance is proportional to frequency, the electronics will be modified to operate over a 20-50 kHz range to assess this effect. Also, the use of a separate, real-time measurement of liquid conductivity will be investigated as a means of obviating the need for calibration measurements. A code similar to FEMEIT will be written to perform three-dimensional simulations with fairly general conductivity spatial variations.

5. Conclusions

Gamma-densitometry tomography (GDT) and electrical-impedance tomography (EIT) systems have been developed and applied to measure material distribution in two-phase and three-phase flows. Two bubble-column test beds, one at laboratory scale and one at industrial scale, have been employed to facilitate diagnostics development and validation. GDT and EIT have been applied to these test beds and related experiments, and comparisons have been made with techniques such as level rise (LR) and differential pressure (DP). When two techniques could be compared, fairly good to very good agreement has been observed.

GDT is the most mature technique and is now routine in application. It has successfully measured material distributions for gas-liquid flows in large steel-walled vessels. EIT is not as mature. While applied successfully to measure the distribution of a dilute suspension of small insulating glass spheres in water, EIT has not yet been completely successful in measuring material distributions in gas-liquid bubble-column flow. Several factors have been identified where significant improvements can be made. DP was found to be a reliable indicator of volumetrically averaged material-distribution properties for bubble-column flow, at least when these properties do not vary strongly in the vertical direction.

A. FEMEIT Files

The following files were used to generate one of the FEMEIT validation examples shown previously. Some files have had portions removed for brevity.

```
nodelm.dat
441
   1 0.996917E+00 0.784591E-01
   2 0.987688E+00 0.156434E+00
   3 0.972370E+00 0.233445E+00
(some lines removed for brevity)
439 0.919545E-01 -.919545E-01
440 0.130043E+00 0.000000E+00
441 0.000000E+00 0.000000E+00
800
   1    80    1  152
   2     1    2   81
   3     2    3   82
(some lines removed for brevity)
798   438   437   427
799   439   438   429
800   440   439   431


exinfo.dat
16
   1    5
   2   10
   3   15
   4   20
   5   25
   6   30
   7   35
   8   40
   9   45
  10   50
  11   55
  12   60
  13   65
  14   70
  15   75
  16   80
```

```
exdata.dat
1    2 0.10000E+03
  0.62400E+03 0.00000E+00 0.23600E+03 0.26900E+03
  0.28400E+03 0.29300E+03 0.30000E+03 0.30600E+03
  0.31000E+03 0.31400E+03 0.31900E+03 0.32300E+03
  0.32900E+03 0.33700E+03 0.35200E+03 0.38500E+03
1    3 0.10000E+03
  0.77700E+03 0.38900E+03 0.10000E+01 0.27200E+03
  0.32000E+03 0.34300E+03 0.35900E+03 0.37300E+03
  0.38300E+03 0.39100E+03 0.39900E+03 0.40900E+03
  0.41900E+03 0.43500E+03 0.45800E+03 0.50600E+03
(some lines removed for brevity)
15   16 0.10000E+03
  0.24200E+03 0.27700E+03 0.29100E+03 0.30000E+03
  0.30700E+03 0.31200E+03 0.31800E+03 0.32200E+03
  0.32700E+03 0.33100E+03 0.33700E+03 0.34600E+03
  0.36000E+03 0.39400E+03 0.63100E+03 0.00000E+00


conpar.dat
0.8 0.1 1. 0.00001 0.00001 1.
50 4 4 2
0.3
0.3
0.
0.
0.99
0.03


parcon.dat
0.80000E+00  0.10000E+00  0.10000E+01  0.10000E-04  0.10000E-04  0.10000E+01
50    4    4    2
0.28613E+00 -.48785E-07    1
0.98310E-01 -.35085E-06    2
-.73243E+00 -.19771E-05    3
0.28811E+00 0.89886E-06    4
0.99000E+00
0.30000E-01


nodcon.dat
1 0.28613E+00 -.48785E-07
2 0.28613E+00 -.48785E-07
3 0.28613E+00 -.48785E-07
(some lines removed for brevity)
439 0.28613E+00 -.48785E-07
440 0.28613E+00 -.48785E-07
441 0.28613E+00 -.48785E-07
```

95

References

Adkins, D. R., Shollenberger, K. A., O'Hern, T. J., and Torczynski, J. R., 1996, "Pressure Effects on Bubble Column Flow Characteristics," in *ANS Proceedings of the 1996 National Heat Transfer Conference*, THD-Vol. 9, American Nuclear Society, LaGrange Park, IL, pp. 318-325.

Barber, C. D., Brown, B. H., and Freeston, I. L., 1983, "Imaging Spatial Distributions of Resistivity Using Applied Potential Tomography," *Electronics Letters*, Vol. 19, pp. 933-935.

Brown, G. O., Stone, M. L., and Gazin, J. E., 1993, "Accuracy of Gamma Ray Computerized Tomography in Porous Media," *Water Resources Research*, Vol. 29, No. 2, pp. 479-486.

Ceccio, S. L., and George, D. L., 1996, "A Review of Electrical Impedance Techniques for the Measurement of Multiphase Flows," *Journal of Fluids Engineering*, Vol. 118, pp. 391-399.

Crowe, C. T., Troutt, T. R., and Chung, J. N., 1996, "Numerical Models for Two-Phase Turbulent Flows," *Annual Reviews of Fluid Mechanics*, Vol. 28, pp. 11-43.

Deckwer, W.-D., and Schumpe, A., 1993, "Improved Tools for Bubble Column Reactor Design and Scale-Up," *Chemical Engineering Science*, Vol. 48, No. 5, pp. 889-911.

Devanathan, N., Moslemian, D., and Dudukovic, M. P., 1990, "Flow Mapping in Bubble Columns Using CARPT," *Chemical Engineering Science*, Vol. 45, No. 8, pp. 2285-2291.

Dickin, F., and Wang, M., 1996, "Electrical Resistance Tomography for Process Applications," *Measurement Science and Technology*, Vol. 7, No. 3, pp. 247-260.

Dudukovic, M. P., Devanathan, N., and Holub, R., 1991, "Multiphase Reactors: Models and Experimental Verification," *Revue de L'Institut Francais du Petrole*, Vol. 46, No. 4, pp. 439-465.

Dudukovic, M. P., Degaleesan, S., Gupta, P., and Kumar, S. B., 1997, "Fluid Dynamics in Churn-Turbulent Bubble Columns: Measurements and Modeling," in Symposium on Gas-Liquid Two-Phase Flows, edited by T. J. O'Hern, J. Bataille, U. S. Rohatgi, M. Shoukri, J. Navickas, I. Celik, American Society of Mechanical Engineers, New York, in press.

Duraiswami, R., 1993, "Bubble Density Measurement Using an Inverse Acoustic Scattering Technique," in *Cavitation and Multiphase Flow Forum*, FED-Vol. 153, edited by O. Furuya, American Society of Mechanical Engineers, New York, pp. 67-73.

Duraiswami, R., Sarkar, K., and Chahine, G. L., 1995, *2DynaEIT: A Boundary Element Code for Efficient Electric Impedance Tomography -- Theory and Test Cases*, Dynaflow Report 95012_1_SAND, Dynaflow, Inc., Fulton, MD.

Dyakowski, T., 1996, "Process Tomography Applied to Multi-Phase Flow Measurement," *Measurement Science and Technology*, Vol. 7, pp. 343-353.

Elghobashi, S., 1994, "On Predicting Particle-Laden Turbulent Flows," *Applied Scientific Research*, Vol. 52, pp. 309-329.

Fan, L.-S., and Tsuchiya, K., 1993, "Bubble Flow in Liquid-Solid Suspensions," in *Particulate Two-Phase Flow*, edited by M. C. Roco, Butterworth-Heinemann, New York, Chapter 23.

Fluid Dynamics International, 1996, *FIDAP Users Manual*, version 7.6, Fluid Dynamics International, Evanston, IL.

Herman, G. T., 1983, "The Special Issue on Computerized Tomography," *Proceedings of the IEEE*, Vol. 71, No. 3, pp. 291-292.

Hewitt, G. F., 1978, *Measurement of Two-Phase Flow Parameters*, Academic Press, London.

Howard, J. N., editor, 1985, *Applied Optics*, Vol. 24, No. 23.

Hua, P., and Woo, E. J., 1990, "Reconstruction Algorithms," in *Electrical Impedance Tomography*, edited by J. G. Webster, Adam Hilger, Bristol and New York, Chapter 10.

Ingber, M. S., Womble, D. E., and Mondy, L. A., 1994, "A Parallel Boundary Element Formulation for Determining Effective Properties of Heterogeneous Media," *International Journal for Numerical Methods in Engineering*, Vol. 37, pp. 3905-3919.

Jackson, N. B., Torczynski, J. R., Shollenberger, K. A., O'Hern, T. J., and Adkins, D. R., 1996a, "Sandia Support for PETC Fischer-Tropsch Research: Experimental Characterization of Slurry-Phase Bubble-Column Reactor Hydrodynamics," in *Proceedings of the First Joint Power and Fuel Systems Contractors Conference: Indirect Liquefaction*, Pittsburgh Energy Technology Center, Pittsburgh.

Jackson, N. B., Torczynski, J. R., Shollenberger, K. A., O'Hern, T. J., and Adkins, D. R., 1996b, "Hydrodynamic Characterization of Slurry Bubble-Column Reactors for Fischer-Tropsch Synthesis," in *Proceedings of the Thirteenth Annual International Pittsburgh Coal Conference*, Vol. 2: "Coal-Energy and the Environment," edited by S.-H. Chiang, University of Pittsburgh Center for Energy Research, Pittsburgh, PA, pp. 1226-1231.

Jaeger, H. M., Nagel, S. R., and Behringer, R. P., 1996, "Granular Solids, Liquids, and Gases," *Reviews of Modern Physics*, Vol. 68, No. 4, pp. 1259-1273.

Jamialahmadi, M., Branch, C., and Müller-Steinhagen, H., 1994, "Terminal Bubble Rise Velocity in Liquids," *Transactions of the Institution of Chemical Engineers*, Vol. 72, Part A, pp. 119-122.

Jones, O. C., Lin, J.-T., Ovacik, L., and Shu, H.-J., 1993, "Impedance Imaging Relative to Gas-Liquid Systems," *Nuclear Engineering and Design*, Vol. 141, pp. 159-176.

Joshi, J. B., Patil, T. A., Ranade, V. V., and Shah, Y. T., 1990, "Measurement of Hydrodynamic Parameters in Multiphase Sparged Reactors," *Reviews in Chemical Engineering*, edited by N. R. Amundson, and D. Luss, Freund Publishing House, London, pp. 73-227.

Kashiwa, B. A., Padial, N. T., Rauenzahn, R. M., and VanderHeyden, W. B., 1993, *A Cell-Centered ICE Method for Multiphase Flow Simulations*, Los Alamos Report LA-UR-93-3922, Los Alamos National Laboratory, Los Alamos, NM.

Kashiwa, B. A., and Rauenzahn, R. M., 1994, *A Multimaterial Formalism*, Los Alamos Report LA-UR-94-771, Los Alamos National Laboratory, Los Alamos, NM.

Knoll, G. F., 1979, *Radiation Detection and Measurement*, John Wiley & Sons, New York, p. 346.

Krishna, R., and Ellenberger, J., 1996, "Gas Holdup in Bubble Column Reactors Operating in the Churn-Turbulent Regime," *AIChE Journal*, Vol. 42, No. 9, pp. 2627-2634.

Kumar, S. B., Devanathan, N., Moslemian, D., and Dudukovic, M. P., 1994, "Effect of Scale on Liquid Recirculation in Bubble Columns," *Chemical Engineering Science*, Vol. 49, No. 24, Part B, pp. 5637-5652.

Kumar, S. B., Moslemian, D., Dudukovic, M. P., 1995a, "A γ-Ray Tomographic Scanner for Imaging Voidage Distribution in Two-Phase Flow Systems," *Flow Measurement and Instrumentation*, Vol. 6, No. 1, pp. 61-73.

Kumar, S., Vanderheyden, W. B., Devanathan, N., Padial, N. T., Dudukovic, M. P., Kashiwa, B. A., 1995b, "Numerical Simulation and Experimental Verification of the Gas-Liquid Flow in Bubble Columns," *AIChE Symposium Series*, Vol. 91, N. 305, pp. 11-19.

Lamarsh, J. R., 1983, *Introduction to Nuclear Engineering*, Addison-Wesley, Reading, MA, pp. 78-88, 472-488, 648-649.

Lapp, R. E., and Andrews, H. L., 1972, *Nuclear Radiation Physics*, Prentice-Hall, Englewood Cliffs, NJ, pp. 247-250.

Lin, J.-T., Jones, O. C., Ovacik, L., and Shu, H.-J., 1993, "Advances in Impedance Imaging Relative to Two-Phase Flow," *ANS Proceedings*, Thermal Hydraulics Division, Vol. 7, American Nuclear Society, LaGrange, IL, pp. 68-75.

Loh, W. W., and Dickin, F. J., 1996, "Improved Modified Newton-Raphson Algorithm for Electrical Impedance Tomography," *Electronics Letters*, Vol. 32, No. 3, p. 206.

MacCuaig, N., Seville, J. P. K., Gilboy, W. B., and Clift, R., 1985, "Application of Gamma-Ray Tomography to Gas Fluidized Beds," *Applied Optics*, Vol. 24, No. 23, pp. 4083-4085.

Mann, R., Dickin, F. J., Dyakowski, T., Williams, R. A., Edwards, R. B., Forrest, A. E., and Holden, P. J., 1997, "Application of Electrical Resistance Tomography to Interrogate Mixing Processes at Plant Scale," *Chemical Engineering Science*, in press.

Meyerhof, W. E., 1967, *Elements of Nuclear Physics*, McGraw-Hill, New York, pp. 91-103.

Moslemian, D., Devanathan, N., and Dudukovic, M. P., 1992, "Radioactive Particle Tracking Technique for Investigation of Phase Recirculation and Turbulence in Multiphase Systems," *Review of Scientific Instruments*, Vol. 63, No. 10, pp. 4361-4372.

Munshi, P., 1990, "A Review of Computerized Tomography with Application to Two-Phase Flows," *Sadhana*, Vol. 15, Part 1, pp. 43-55.

O'Hern, T. J., Torczynski, J. R., Ceccio, S. L., Tassin, A. L., Chahine, G. L., Duraiswami, R., and Sarkar, K., 1995a, "Development of an Electrical Impedance Tomography System for an Air-Water Vertical Bubble Column," in *Forum on Measurement Techniques in Multiphase Flows*, FED-Vol. 233, edited by T. J. O'Hern, A. Naqwi, C. Presser, and R. D. Skocypec, American Society of Mechanical Engineers, New York, pp. 531-537.

O'Hern, T. J., Torczynski, J. R., Shollenberger, K. A., and Ceccio, S. L., 1995b, "Electrical Impedance Tomography for Spatial Measurements of Gas Distribution in Multiphase Flows," *Bulletin of the American Physical Society*, Vol. 40, No. 12, p. 2004.

Pan, L., and Hewitt, G. F., 1995, "Precise Measurement of Cross Sectional Phase Fractions in Three-Phase Flow Using a Dual-Energy Gamma Densitometer," *ANS Proceedings*, Thermal Hydraulics Division, Vol. 8, pp. 71-78.

Press, W. H., Flannery, B. P., Teukolsky, S. A., and Vetterling, W. T., 1986, *Numerical Recipes: The Art of Scientific Computing*, Cambridge University Press, New York, Section 3.3, pp. 86-89.

Reda, D. C., Hadley, G. R., and Turner, J. R., 1981, "Application of the Gamma-Beam Attenuation Technique to the Measurement of Liquid Saturation for Two-Phase Flows in Porous Media," in *Instrumentation in the Aerospace Industry*, Vol. 27, *Advances in Test Measurement*, Vol. 18, Part Two, *Proceedings of the 27th International Instrumentation Symposium*, edited by K. E. Kissell, Instrument Society of America, Research Triangle Park, NC, pp. 553-568.

Savolainen, T., Kaipio, J. P., Karjalainen, P. A., and Vauhkonen, M., 1996, "An Electrical Impedance Tomography Measurement System for Experimental Use," *Review of Scientific Instruments*, Vol. 67, No. 10, pp. 3605-3609.

Shah, Y. T., and Deckwer, W.-D., 1983, "Hydrodynamics of Bubble Columns," in *Handbook of Fluids in Motion*, edited by N. P. Cheremisinoff and R. Gupta, Ann Arbor Science Publishers, Ann Arbor, MI, Chapter 22.

Shollenberger, K. A., Torczynski, J. R., Adkins, D. R., and O'Hern, T. J., 1995a, "Bubble Column Measurements Using Gamma Tomography," in *Fluid Measurement and Instrumentation*, FED-Vol. 211, edited by G. L. Morrison, M. Nishi, T. B. Morrow, and R. A. Gore, American Society of Mechanical Engineers, New York, pp. 25-30.

Shollenberger, K. A., Torczynski, J. R., Adkins, D. R., and O'Hern, T. J., 1995b, "Gamma Densitometry Tomographic Measurements of Void-Fraction Spatial Distribution in Bubble Columns," in *Frontiers in Industrial Process Tomography*, edited by D. M. Scott and R. A. Williams, Engineering Foundation, New York, p. 329.

Shollenberger, K. A., Torczynski, J. R., Adkins, D. R., O'Hern, T. J., and Jackson, N. B., 1997a, "Gamma Densitometry Tomography of Gas Holdup Spatial Distribution in Industrial Scale Bubble Columns," *Chemical Engineering Science*, in press.

Shollenberger, K. A., Torczynski, J. R., O'Hern, T. J., Adkins, D. R., Ceccio, S. L., and George, D. L., 1997b, "Comparison of Gamma-Densitometry Tomography and Electrical-Impedance Tomography for Determining Material Distribution in Liquid-Solid Flows," in *Cavitation and Multiphase Flow Forum*, edited by J. Katz and K. J. Farrell, American Society of Mechanical Engineers, New York, in press.

Taylor, L. M., and Preece, D. S., 1989, *DMC -- A Rigid Body Motion Code for Determining the Interaction of Multiple Spherical Particles*, Sandia Report SAND88-3482, Sandia National Laboratories, Albuquerque, NM.

Thompson, Kyle R., and Stoker, G. C., 1997, Private Communication, Sandia National Laboratories, Albuquerque, NM.

Torczynski, J. R., O'Hern, T. J., Adkins, D. R., Shollenberger, K. A., Mondy, L. A., and Jackson, N. B., 1994, "Sandia Support for PETC Fischer-Tropsch Research. Part A: Experimental Flows in Slurry-Phase Bubble-Column Reactors," in *Proceedings of the 1994 Coal Liquefaction and Gas Conversion Contractors' Review Conference*, edited by S. Rogers, P.-Z. Zhou, and K. Lockhart, Pittsburgh Energy Technology Center, Pittsburgh, pp. 449-456.

Torczynski, J. R., Shollenberger, K. A., O'Hern, T. J., and Adkins, D. R., 1995, "Tomographic Measurements of Volume Fractions in Multiphase Flows," *Bulletin of the American Physical Society*, Vol. 40, No. 12, p. 2004.

Torczynski, J. R., Adkins, D. R., Shollenberger, K. A., and O'Hern, T. J., 1996a, "Application of Gamma-Densitometry Tomography to Determine Phase Spatial Variation in Two-Phase and Three-Phase Bubbly Flows," in *Cavitation and Multiphase Flow Forum*, FED-Vol. 236, edited by J. Katz and K. J. Farrell, American Society of Mechanical Engineers, New York, pp. 503-508.

Torczynski, J. R., O'Hern, T. J., Shollenberger, K. A., Ceccio, S. L., and Tassin, A. L., 1996b, "Finite Element Method Electrical Impedance Tomography for Phase Distribution Determination in Multiphase Flows: Validation Calculations and Experiments," in *Cavitation and Multiphase Flow Forum*, FED-Vol. 236, edited by J. Katz and K. J. Farrell, American Society of Mechanical Engineers, New York, pp. 497-501.

Torczynski, J. R., Shollenberger, K. A., O'Hern, T. J., and Adkins, D. R., 1996c, "Gamma Densitometry Tomographic Measurements of Gas Distribution in a Large-Diameter Bubble Column," *Bulletin of the American Physical Society*, Vol. 41, No. 9, p. 1824.

Torvik, R., and Svendsen, H. F., 1990, "Modelling of Slurry Reactors. A Fundamental Approach," *Chemical Engineering Science*, Vol. 45, No. 8, pp. 2325-2332.

Toye, D., Marchot, P., Crine, M., and L'Homme, G., 1996, "Modelling of Multiphase Flow in Packed Beds by Computer-Assisted X-Ray Tomography," *Measurement Science and Technology*, Vol. 7, pp. 436-443.

Vest, C. M., 1985, "Tomography for Properties of Materials that Bend Rays: A Tutorial," *Applied Optics*, Vol. 24, No. 23, pp. 4089-4094.

Weast, R. C., editor, 1973, *CRC Handbook of Chemistry and Physics*, 54th edition, CRC Press, Cleveland, OH, p. B-133.

Webster, J. G., editor, 1990, *Electrical Impedance Tomography*, Adam Hilger, Bristol, UK.

Wilkinson, P. M., Spek, A. P., and van Dierendonck, L. L., 1992, "Design Parameters Estimation for Scale-Up of High-Pressure Bubble Columns," *AIChE Journal*, Vol. 38, No. 4, pp. 544-554.

Wolfram, S., 1996, *The Mathematica Book*, Cambridge University Press, Cambridge, UK.

Yang, Y. B., Devanathan, N., and Dudukovic, M. P., 1994, "Liquid Backmixing in Bubble Columns via Computer Automated Radioactive Particle Tracking (CARPT)," *Experiments in Fluids*, Vol. 16, No. 1, pp. 1-9.

Yorkey, T. J., Webster, J. G., and Tompkins, W. J., 1987, "Comparing Reconstruction Algorithms for Electrical Impedance Tomography," *IEEE Transactions on Biomedical Engineering*, Vol. BME-34, No. 11, pp. 843-852.

Zuber, N., and Findlay, J. A., 1965, "Average Volumetric Concentration in Two-Phase Flow Systems," *Journal of Heat Transfer*, pp. 453-468.

Distribution